Making use of local remote sensing measurements for improving snow cover products over different scales

Dissertation zur Erlangung des Doktorgrades
an der Fakultät für Geowissenschaften
der Ludwig-Maximilians-Universität München

Vorgelegt von
Stefan Härer
aus München, Deutschland

München, 08.12.2017

Erstgutachter:	Prof. Dr. Karsten Schulz
Zweitgutachter:	Prof. Dr. Ralf Ludwig
Tag der mündlichen Prüfung:	15.06.2018

"Karriere ist etwas Herrliches,

aber man kann sich nicht in einer kalten Nacht an ihr wärmen." (Marilyn Monroe)

Zusammenfassung

Die vorgelegte Arbeit hat die Entwicklung von Methoden zur Minimierung der heutigen Probleme im Bereich des Monitorings der alpinen Schneedecke im Fokus. Im Besonderen geht es um die Bereitstellung neuer Datenprodukte zur Verbesserung der Genauigkeiten von satellitenbasierten Schneedeckenkarten und damit einhergehend der Verbesserung der Evaluationsmöglichkeiten von Landoberflächenmodellen.

Die alpine Schneedecke ist ein zeitlich wie räumlich höchst dynamischer Wasserspeicher. Sie ist von hoher Relevanz für die Wasserversorgung der Gebirgsregionen selbst, sowie ihrer Vorländer. Der Schneespeicher reagiert dabei direkt und ohne zeitliche Verzögerung auf Veränderungen des lokalen Klimas und somit auch auf Folgen des Klimawandels. Klimatische Veränderungen können z.B. Einfluss auf die mittlere Akkumulationshöhe, die Schneedeckendauer oder die Ablationsdynamik der Schneedecke haben. Verändert sich eine dieser Größen, verändert das direkt die bestehenden Abflussregime bzw. führt potentiell zu einer Verstärkung von Abflussextremen.

Ein Wandel des Abflussverhaltens bedeutet dabei, dass sich die Abflussvolumina im Gerinne zeitlich verschieben und bisher gängige Entnahmestrategien, z.B. im Bereich der Bewässerung, nicht mehr funktionieren würden bzw. nicht mehr nachhaltig wären. Eine Änderung der Abflussextreme bedeutet z.B. im wahrscheinlichen Falle eines tendenziell abnehmenden mittleren Volumens des Schneespeichers, dass sommerliche Niedrigwasser nicht mehr wie im bisherigen Umfang durch Schmelzwasser gestützt werden könnten, was wiederum direkt zu einer Häufung von Niedrigwasserperioden führen würde. Eine Zunahme von Zuständen mit isothermen und wassergesättigten Schneedecken hingegen, könnte tendenziell zu einer Häufung von Hochwasserereignissen führen, die durch sogenannte Regen-auf-Schnee Ereignisse erzeugt werden. Jede Änderung am Akkumulations- oder Ablationsverhalten der alpinen Schneedecke hat demzufolge das Potential die heute bestehenden Abflussregime in Zukunft deutlich zu modifizieren und die Unsicherheiten in der Prognose zukünftiger Abflüsse zu erhöhen.

Um diese Prognoseunsicherheiten zu minimieren sind adäquate, robuste und valide Modellansätze von Nöten. Die Modelle können allerdings nur mit geeigneten Datensätzen bestätigt bzw. überprüft werden. Die Verfügbarkeit von Evaluationsdatensätzen im Gebirge ist aber sehr begrenzt. Die Anzahl alpiner meteorologischer Stationen ist seit Jahren sehr gering und erlaubt kein auch nur ansatzweise flächendeckendes Monitoring. Satellitendaten auf der anderen Seite erfassen die großräumige Erstreckung der Schneedecke zumeist sehr gut, allerdings ist die zeitliche Auflösung und die Qualität der Produkte, zumindest im Bereich der räumlich hochauflösenden Satelliten, für ein genaues Monitoring häufig nicht hinreichend. Es fehlt also ein überzeugendes Instrument zur Erzeugung von qualitativ hochwertigen Daten auf regionaler/lokaler Skala mit einer hohen räumlichen und zeitlichen Auflösung, das zudem leicht einsetzbar und robust gegen die harschen Bedingungen im Hochgebirge ist.

Eine im Rahmen dieser Arbeit durchgeführte Analyse, der im Gebirge vorhandenen und potentiell zur Beobachtung der Schneedecke geeigneten Systeme, kam schnell zu dem Schluss, dass die Anzahl an Webcams im alpinen Raum in den letzten Jahren deutlich zugenommen hat. Die photographischen Datenreihen der Webcams haben eine hohe räumliche und zeitliche Auflösung und sind in der Regel leicht über das Internet abzurufen. Dennoch wurde diese zusätzliche Datenquelle bisher nicht entsprechend in Wert gesetzt. Basierend auf diesem Ergebnis wurde die Analysesoftware PRACTISE (Photo Rectification And ClassificaTIon SoftwarE) entwickelt, die im Zentrum dieser Dissertation steht. Die Arbeiten, die im Rahmen der Entwicklung von PRACTISE durchgeführt wurden, werden anhand von vier Publikationen erläutert. Die Publikation „PRACTISE - Photo Rectification And ClassificaTIon SoftwarE (v.1.0)“ beschreibt die generelle Idee hinter der Software, deren Konzeption und die verwendeten Methoden. So wird dargestellt wie sich die Transformation einer zweidimensionalen Information aus einer photographischen Aufnahme in eine orthorektifizierte Schneedeckenkarte vollzieht. Die zweite Publikation „Matlab toolbox PRACTISEgeo v.1.0“ ist eine Erweiterung auf andere Anwendungsgebiete der terrestrischen Fotografie und erhöht die Nutzerfreundlichkeit in Hinblick auf die Analyse langer Zeitreihen. Die dritte Publikation „PRACTISE - Photo Rectification And ClassificaTIon SoftwarE (v.2.1)” zeigt anschließend die Möglichkeiten von PRACTISE im Bereich der Kalibrierung von satellitenbasierten Schneekarten bzw. der Evaluierung von anderen Produkten auf. Die

vierte Publikation „On the need of a time- and location-dependent estimation of the NDSI threshold value for reducing existing uncertainties in snow cover maps at different scales“ beschreibt anhand einer mehrjährigen Analyse zweier Testgebiete in den europäischen Alpen detailliert, welche Unsicherheiten in normalized-difference snow index (NDSI) basierten Schneedeckenprodukten zu erwarten sind und wie man diese Unsicherheiten zu minimieren vermag.

Schlussendlich steht mit der Entwicklung von PRACTISE nun ein Werkzeug zur Verfügung das oben benannte Lücken in der Schneedeckenbeobachtung auf lokaler Skala schließen kann. PRACTISE wird inzwischen von vielen internationalen Arbeitsgruppen genutzt und wird als public domain software stetig weiterentwickelt.

Neben den genannten Veröffentlichungen die den Rahmen dieser Promotion darstellen sind weitere Publikationen entstanden, die aber nicht direkt in die Dissertation eingebaut wurden:

Bernhardt, M., Härer, S., Jacobeit, J., Wetzel, K. F., and Schulz, K.: The virtual alpine observatory - research focus Alpine hydrology, Hydrol. Wasserbewirts., 58, 241–243, 2014.

Weber, M., Bernhardt, M., Pomeroy, J. W., Fang, X., Härer, S., and Schulz, K.: Description of current and future snow processes in a small basin in the Bavarian Alps, Environ. Earth Sci., 75(17), 1223, doi: 10.1007/s12665-016-6027-1, 2016.

Summary

The presented work deals with the development of new monitoring methods for minimizing current uncertainties in snow cover mapping. In particular, it is about providing new data products to improve the accuracy of satellite-based snow cover maps and to improve the evaluation capabilities for land surface models.

The alpine snow cover is a water storage which is highly dynamic in space and time. It is of high relevance for the water supply of the mountain regions themselves, as well as of their forelands. The snow reservoir thereby reacts directly and without delay to changes in the local climate and thus also to the consequences of climate change. Climatic changes can alter the mean accumulation height of the snow cover, the snow cover duration or the ablation dynamics of the snowpack. A change in one of these parameters is directly coupled to changes in the current runoff regimes and potentially leads to more frequent or stronger runoff extremes.

A change in the regimes means that runoff volumes will be transferred from e.g. one month to another and current withdrawal strategies, e.g. in the field of irrigation, would cease to function or would no longer be sustainable. A change in the runoff extremes means e.g. in the probable case of a decreasing mean volume of the snow reservoir, that low waters in summer could not be supported by meltwater to the previous extent, which in turn would directly lead to an increasing number of low water periods. As a contrast, an increase in conditions with isothermal and water-saturated snowpacks could result in more flood events that are generated by rain-on-snow events. Each change in the accumulation or ablation characteristic of alpine snow cover thus has the potential to significantly modify the future runoff behaviour of rivers that are influenced by mountains and as a result can introduce large uncertainties in the forecast of future runoffs.

In order to minimize these forecast uncertainties, adequate, robust and valid model approaches are needed. The models, however, can only be confirmed or verified with suitable evaluation data sets. But the availability of evaluation datasets in the mountains is very limited. The number of alpine meteorological stations has been low for years and does not permit any kind of nationwide monitoring.

Satellite data, on the other hand, can cover the large-scale snow cover very well, but the temporal resolution as well as the quality of the snow products, at least in the area of high-resolution satellites, is often not sufficient for an accurate monitoring. So, there is no convincing instrument for the generation of high-quality data on a regional/local scale with a high spatial and temporal resolution available, which is also easy to use and robust against the harsh conditions in high mountain areas.

An analysis of available instruments in the mountains that are potentially suitable for the observation of snow cover has come to the conclusion that the number of webcams in the Alpine region has increased significantly in recent years. The photographic data series of the webcams have a high spatial and temporal resolution and are usually easy to retrieve via the Internet. Nonetheless, this additional data source is rarely used until now. Based on this result, the analysis software PRACTISE (Photo Rectification And ClassificaTion SoftwareE) was developed, which is the focus of this dissertation. The work carried out in course of the development of PRACTISE is presented in form of four publications. The publication "PRACTISE - Photo Rectification And ClassificaTion SoftwareE (v.1.0)" describes the general idea behind the software, its conception and the methods used. It shows how the transformation of two-dimensional information from a photographic image into an orthorectified snow cover map takes place. The second publication "Matlab toolbox PRACTISEgeo v.1.0" expands the first publication to other application areas of terrestrial photography and enhances user-friendliness in view of the analysis of long-term photograph series. The third publication "PRACTISE - Photo Rectification And ClassificaTion Software (v.2.1)" subsequently highlights the possibilities of PRACTISE in calibrating satellite-based snow cover maps or evaluating other products. The fourth publication "On the need of a time- and location-dependent estimation of the NDSI threshold value for reducing existing uncertainties in snow cover maps at different scales" shows on basis of a long-term analysis of two Alpine test sites which uncertainties in today’s NDSI based snow cover maps exist and how these uncertainties can be minimized. Finally, through the development of PRACTISE, a tool is now available to close the above-mentioned gaps in the observation on the local scale. PRACTISE is already used by many international working groups and is constantly evolving as a public domain software.

In addition to the publications mentioned in the framework of the thesis, further publications have been produced, but these were not directly included in the dissertation:

Bernhardt, M., Härer, S., Jacobeit, J., Wetzel, K. F., and Schulz, K.: The virtual alpine observatory - research focus Alpine hydrology, Hydrol. Wasserbewirts., 58, 241–243, 2014.

Weber, M., Bernhardt, M., Pomeroy, J. W., Fang, X., Härer, S., and Schulz, K.: Description of current and future snow processes in a small basin in the Bavarian Alps, Environ. Earth Sci., 75(17), 1223, doi: 10.1007/s12665-016-6027-1, 2016.

Acknowledgements

I want to thank so many people here that were in one way or another supportive to my thesis and my personal development in the last years but as I cannot mention all of them I have to restrict myself mainly to the supporting teams and institutions.

At first, I thank the German environment foundation (DBU) for my personal scholarship (AZ20011/138) and the team of the Environmental Research Station Schneefernerhaus (UFS) for the infrastructural resources as well as the support and nice atmosphere during my stays at the Zugspitze.

Moreover, I want to acknowledge the NASA and USGS services for the satellite data of the Landsat series, Dr. Daniel Morche for the DEM of the Zugspitze area, and Matthias Siebers for the camera data of the Vernagtferner area. I also want to use this opportunity to thank my co-authors as well as editors and reviewers of my publications again.

In addition, I want to thank the MICMoR graduate program with special thanks to the coordinating persons of the program, Dr. Elija Bleher and Petra Guppenberger as well as my mentors in the program Prof. Dr. Karl-Friedrich Wetzel and Dr. Nick Rutter.

And now - very important - thank you to all my great colleagues in Munich and in Vienna. You always had an open ear and were supportive in case of problems and besides, made university fun. Moreover, I am happy to call some of you my friends today. In particular, I have to mention Prof. Dr. Karsten Schulz and Assoc. Prof. Dr. Matthias Bernhardt here. Both accompany my work for years now with a mixture of leadership and collegiality. Thank you for your trust and confidence! And thank you for the great TV evenings watching our favourite football teams or the expert talk in the coffee breaks the next day!

A big thank you also goes to all the people I enjoy spending time with outside the university. This especially includes my friends from school, football or studies. You do not know how much it means to me that I have such great friends in life and that you made each of our too rare meetings fun and special.

At last, I want to thank my parents and all other family members: for their love, endless support, encouragement and sacrifices. A special ‘thank you’ is dedicated to my wife Michaela and our baby for not only supporting and being with me but for enriching my life in all its facets.

Table of contents

List of figures

List of tables

Aim and content of the thesis

The presented thesis is targeted on the development of a new monitoring scheme for the spatial distribution of snow cover in mountain regions. Adequate monitoring systems are needed as the snowpack and its spatial distribution is a key to properly understand the alpine water cycle. Today's monitoring strategies still lack a tool that is able to link plot and regional scale measurements (fig. 0.1). This leads to an information gap between point measurements which allow for a detailed investigation of the state of the snow cover at the plot scale, but which do only have a very limited spatial representativeness, and large-scale products, like remotely sensed data, able to deliver an overview over the general snowpack distribution, but which are in turn connected to significant uncertainties when used at the plot scale.

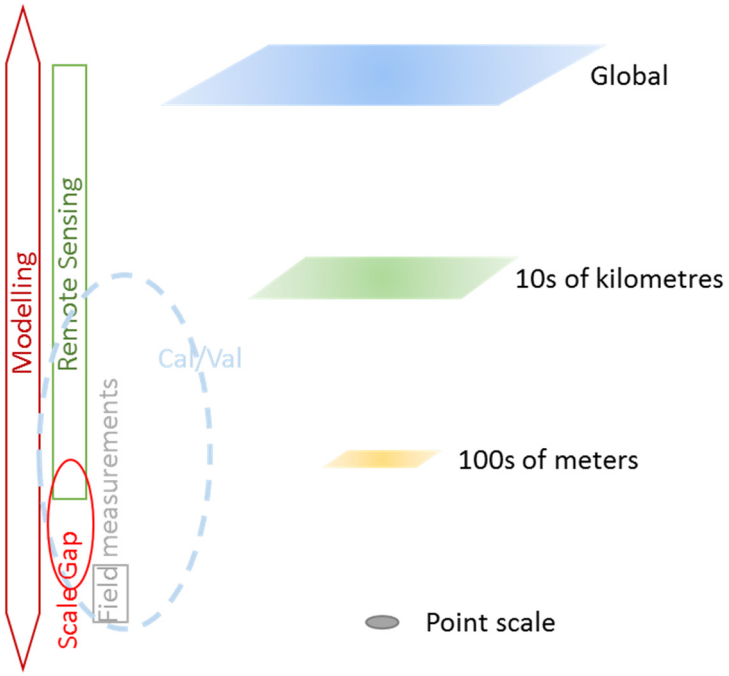

Figure 0-1: Schematic overview over important scales in alpine studies with a focus on hydrology.

The widely available networks of webcams in mountain regions, until now an unused source of information, were identified as able to close this scale gap. For doing so, a new software package PRACTISE was developed in course of the presented thesis (Härer et al., 2013; Härer et al., 2016). The software is suited to orthorectify and classify webcam images. The resulting products deliver

information on the snow cover distribution with a high spatial and temporal resolution at the sub-catchment scale. An included optimization routine for NDSI based satellite products additionally allows connecting this local scale information with the regional satellite data.

The thesis is structured as follows:

- First, an *Introduction* chapter will give an overview over the importance of the alpine snow cover in view of the general water supply and the existing challenges connected to a continuous monitoring of the Alpine snow cover distribution. The section *Ground-based station network* will describe the development as well as the advantages and limitations of the existing station network on the example of the European Alps. After that, the section *Description of the snow cover distribution* will give an insight into the modeller perspective who use the available ground-based data. And then, current satellite products are introduced and discussed in the section *Satellite-based snow cover products*.
- The chapter *Bridging the gap* is then introducing the background of the software developed in here and presenting its application. The chapter mainly consists of four papers. The paper *PRACTISE - Photo Rectification And ClassificaTIon SoftwarE (v.1.0)* is focusing on the georectification and snow classification of photographs. The second paper *Matlab© toolbox PRACTISEgeo v.1.0: Extending the focus of PRACTISE (Photo Rectification And ClassificaTIon Software) from the cryosphere to other geoscientific photo mapping applications* displays improvements with respect to user friendliness and versatility of the software, paper three *PRACTISE – Photo Rectification And ClassificaTIon SoftwarE (v.2.1)* introduces the link between local photographs and satellite products while the last paper *On the need of a time- and location-dependent estimation of the NDSI threshold value for reducing existing uncertainties in snow cover maps at different scales* is discussing the advantages of PRACTISE 2.1 improved Landsat snow cover maps on the example of a multi-year analysis of two Alpine catchments.
- Finally, a *Discussion and Outlook* chapter sums up the results of this thesis and will give an overview of potential future developments.

I Introduction

Fresh water has become a vulnerable and intensively used natural resource (Gosling and Arnell, 2016). The higher demand of process water, for example used for energy production as well as irrigation, is thereby opposing regulations which are asking for certain rest water quantities and limit the uncontrolled withdrawal of fresh water in many parts of the world. Consequences are several water use conflicts and that any changes in the general water availability can aggravate the tensions between different stakeholders. Climate change can lead to such changes and an increasing global population additionally enlarges the pressure on water supply systems (Staben et al., 2015; Tolle et al., 2013; Whateley et al., 2014).

As a result of the ongoing climate change process, significant drought events/periods (Adamson et al., 2009; AghaKouchak et al., 2014; Zheng et al., 2012), a potential increase in the insensitivity and/or number of flood events (Alexander, 1995; Blöschl et al., 2006), and changes of the annual distribution of runoff and therewith of the availability of water (Afzal et al., 2015; Ahmad et al., 2012; Bao et al., 2012; Bookhagen and Burbank, 2010) can be already observed or anticipated. When expecting a higher vulnerability of the water supply system, it is important to analyse where the available water originates. Moreover, it is essential to understand if the fresh water is mainly generated and used on a regional scale, or if it belongs to an area which is far away and which does potentially have a different vulnerability or reactivity to climate change than the area in which the water is used.

By doing this, it becomes obvious that mountain areas do play a key role in this context. Nearly half of humanity are directly or indirectly dependent on water from mountain regions (Viviroli et al., 2007). Figure 1-1 underlines that mountain water is an important fresh water source in nearly any area of the world. Water from the mountains does thereby not only increase the water availability in the forelands but does also modify the runoff regime (Viviroli et al., 2011). This usually results in a significant support of summer runoff in the forelands, which can be related to the melt out of mountain snow and ice covers. Without this support, water shortages would have to be expected in many regions of the world (Viviroli et al., 2011). But, there are also risks connected to the water stored in form of mountain snow and ice.

So-called rain-on-snow events, where rain is falling on an isothermal and water-saturated snowpack, can result in major and destructive flood events as well (Pomeroy et al., 2016).

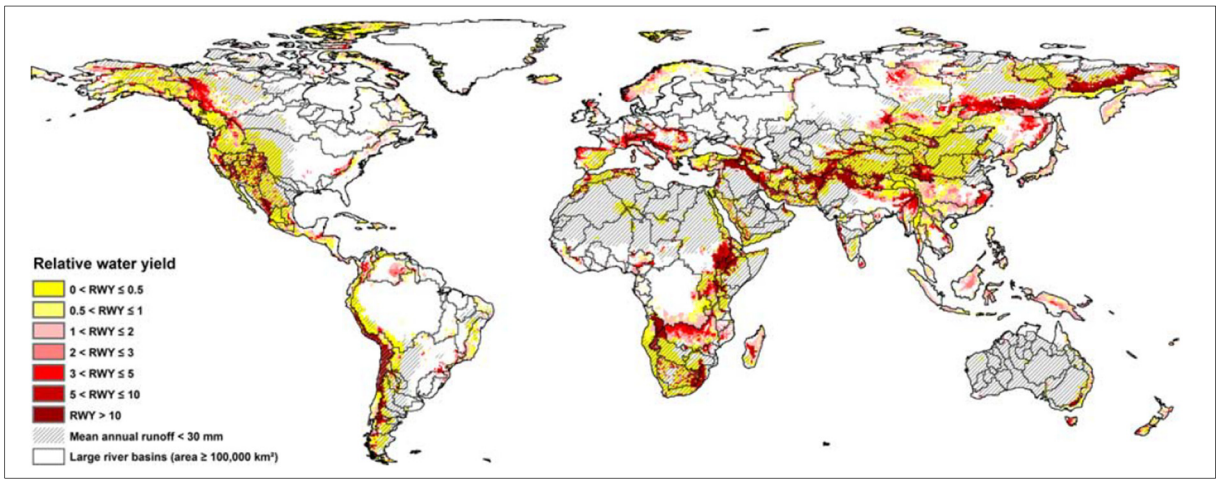

Figure 1-1: Disproportionality of mountain runoff formation relative to average lowland runoff (RWY), mapped cell by cell for mountainous areas. Disproportionality in favor of runoff is given when RWY is greater than 1, its importance being marked for RWY > 2 and essential for RWY > 5 (cited from Viviroli et al., 2007).

The timing and the amount of water released by mountain regions in general is more related to processes in the cryosphere than to the annual precipitation distribution (Viviroli et al., 2007). As the impact and dependence on mountain water is high (Mankin et al., 2015; Viviroli et al., 2011; Viviroli et al., 2007), knowledge about the actual size and the temporal development of the snow cover, which is the largest and most variable water storage in high elevations, is of major importance. It is the key to properly understand the current runoff behaviour and is also needed for a short-term or seasonal runoff forecast of rivers with an influencing mountainous share.

The observation and prediction of snow cover at the point as well as at the global scale are thereby fairly straightforward. It is known that the mean maximum areal extent of the annual snow-covered area is about 47 million square kilometers, which again highlights the importance of this storage term (Wang et al., 2014). 98 % percent of the snow cover is thereby located in the northern hemisphere and large parts can be classified as seasonal snow cover which underlines the high spatial and temporal variability of the global snow cover (Armstrong and Brun, 2008). While the large-scale information is important in view of e.g. global climate models and correct ground albedo values, information at the plot scale

helps to understand e.g. the physical processes within the snowpack. But, for model evaluation and runoff forecast data on the catchment or sub-catchment scale is needed. Gathering data at these resolutions is however a difficult task and hence not available to a comparable extent.

Klemes [1990] stated that "a team of Olympic ski heroes" would be needed for any field campaign in case meaningful data should be achieved from rough mountainous regions. He furthermore stated that remote sensing data can be only used partwise as the delivered data is prone to high uncertainties because of the steep topography (Klemes, 1990). He moreover defined mountain hydrology as the blackest of all black boxes in hydrology (Klemes, 1988). The arguments of Klemes do still have some foundation independent of the fact that the monitoring networks and the available data has been heavily extended since then. However, the characteristic spatial scales of the meteorological forcing, which are determining the snow cover distribution, are still poorly captured even with relatively dense networks of high altitude meteorological stations like those in Switzerland (Tobin et al., 2011; Frei and Schär, 1998). The existing uncertain data in complex terrain is leading to biases as large as 25 % in view of the question where snow accumulates (Groisman and Legates, 1994). Another problem in this context is that the limited number of available stations is leading to large uncertainties in the determination of the phase of precipitation. This again introduces uncertainties in the prediction of the accumulation or ablation height (Tobin et al., 2011; Benestad and Haugen, 2007). So, if the available point data is used for driving hydrological models many error sources are existent which can then lead to questionable model representations of the spatial snow cover distribution. This again leads to the need for monitoring schemes which allow for the identification of potential errors in the spatial distribution of the modelled snowpack. Satellite data is an often used solution in this context.

Originally, snow cover was mapped by visually inspecting the satellite data (Singer and Pohham, 1963). In a next step and with the introduction of new multichannel satellite systems, a trend to automatic classification approaches could be observed (Ma, 1998; Wang, 1999). In course of this development, the normalized-difference Snow Index (NDSI), already presented in 1989 (Dozier, 1989), became one of the major satellite snow cover mapping methods because of a relatively high quality and a high degree of automatization in the classification (Winther and Hall, 1999; Hall et al., 2002). NDSI based

approaches however also have a major weakness as the correct setting of the needed threshold value to distinguish between snow-covered and snow-free areas is a prerequisite for high qualitative snow cover maps (Härer et al., 2016). Another problem of satellite-based measurements in general is that they are not temporally continuous on a day-by-day basis. The main reason is bad weather which makes many of the available satellite scenes unusable. Furthermore, the channel setup of different satellite sensors and the spatial resolution of the available satellites are varying. This leads to different accuracies and information contents if it comes to snow cover mapping and often makes an intersection of the products difficult.

Hence, the available sources of information are either valid at the plot scale or at the regional scale but there is nearly no high qualitative and high resolution (temporal as well as spatial) data available at the sub-catchment scale. This data, on the other hand, is essential for gaining a better understanding on the spatial development of the snowpack in mountains and for the evaluation of hydrological models used in these mountain environments where snow cover represents a key component of the hydrological cycle.

1.1 Ground-based station network

The installation of ground-based meteorological stations in high mountains was very often connected to the introduction of astronomical observatories. In Europe, the first observatories were initialized after the second international Meteorological Congress in Rome (1879). Those are for example Puy de Dome (1876, France), Sonnblick (1886, Austria), Zugspitze (1900, Germany), Jungfraujoch (1931, Switzerland) and Davos Weissfluhjoch (1936, Switzerland). Most of the observatories which were introduced during this time are still operating and are important sources of information about long-term changes in the European Alps. Nevertheless, the named stations are only covering a few mountain sites in Europe and the general coverage of high altitudes is very low when compared to the lower elevations. Figure 1.1-1a gives an overview of the elevation distribution of the existing meteorological stations.

The meteorological stations in mountains usually gather information on the water input, the available melt energy, the air and snow temperature, the snowpack depth and other parameters at a certain location. The problem with the available point measurements in mountains in general is that they have

a limited spatial representativeness. This is mainly due to two factors. Firstly, the meteorological stations are located in areas which are following certain predefined standards. The most important one defines that the area around a meteorological station has to be more or less flat. This does not combine well with the main topographical features in mountain environments. Secondly, changing climate conditions over short distances which can be related to the undulated and steep topography do limit the general meaning of the measurements for larger areas. Besides these two aspects, high elevation stations do always have problems in view of the continuity of the measurements as they have a higher failure probability than flatland stations because of e.g. freezing events (fig. 1.1-1b).

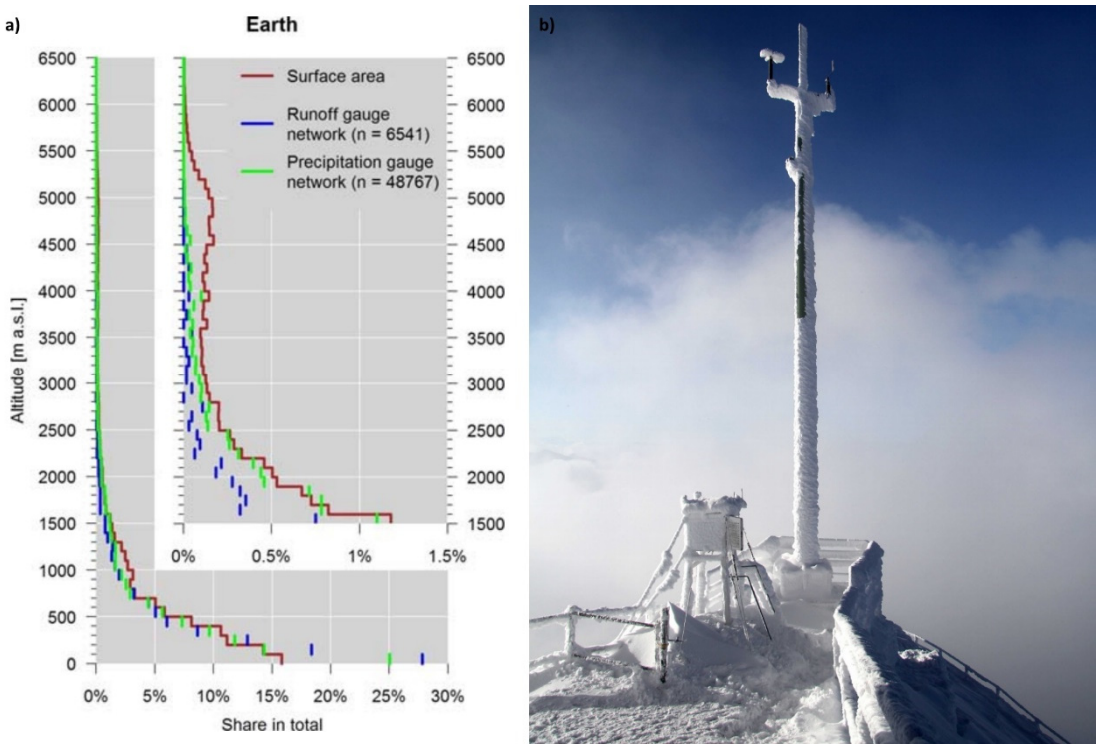

Figure 1.1-1: (a) Altitudinal distribution of global runoff stations represented in the GRDC archive and global precipitation station network represented in the GPCC archive compared to global hypsography of the land surface area (without Greenland and Antarctica). The inset shows a magnification for altitudes above 1500 m. a.s.l. (from Viviroli et al., 2011). (b) Snow and ice-covered weather station of the DWD at the Wendelstein. The station was shut down on 21st September 2012 due to costs ending a continuous measurement time series of 130 years (Elsert et al., 2012).

The higher failure probability and spatially as well as temporally highly variable meteorological fields would in principle require for a higher density of meteorological stations in mountain areas if the existing uncertainties in the measurements should be reduced. This would be moreover reasonable in view of the

importance of mountain areas in context of the global water supply (Viviroli et al., 2007) and of the climate change process which does have highly pronounced effects in high elevation areas (Scherrer et al., 2004; Marty, 2008; Bavay et al., 2009). Despite this knowledge, the existing density of meteorological stations above 1500 m a.s.l. is extremely low because of the high installation and maintenance charges.

Hence, one can conclude that meteorological stations are an important source of information in view of numerous parameters related to the alpine snow cover but they do have a low spatial coverage and a low spatial representativeness. The resulting data is therefore hard to regionalize and therefore of limited value for the evaluation of spatially distributed snow cover products.

1.2 Description of the snow cover distribution

If the size of the snow storage in mountains needs to be quantified for e.g. hydrological predictions or for flood forecasting issues, data about the spatial extent of the snow cover is needed as well as the snow depth distribution. This means that the point measurements of the available meteorological stations have to be translated into an information on the temporal and spatial development of the snowpack. The translation of meteorological variables into a snowpack evolution is thereby straightforward at the point scale as the available measurements are usually able to support even complex snow evolution models and because of the fact that the measurements are meaningful at this specific location. However, the description of the snow cover distribution in alpine terrain is a more difficult task as numerous influencing parameters like wind speed and direction, which can be hardly distributed in space on basis of point measurements, do play a key role in view of the observed snow distribution.

Besides these challenges, numerous snow cover model approaches were developed for calculating a spatially distributed representation of the real snowpack. The range of available models is thereby immense and reaches from simple statistical approaches (Abermann et al., 2011; Braithwaite, 1995; Bormann et al., 2014), over semi-empirical approaches (Bernhardt et al., 2010; Liston and Elder, 2006), up to process-based approaches (Pomeroy et al., 2007; Lehning et al., 2006). In addition, different statistical approaches are available which try to distribute the snow cover on basis of different terrain characteristics (Lehning et al., 2011; Bernhardt and Schulz, 2010).

All of the named approaches thereby rely on input data. The more complex the approaches are, the more input data they need. This is problematic because of the above-mentioned problems of a low availability and quality of the data. The uncertainty which stems from this data can then lead to problems in the model representation of the snow cover distribution. As the input information might be weak, the model results have to be very well evaluated. This is especially the case if information about the spatial snow cover distribution is needed for e.g. flood forecasts where error-prone or misleading information could lead to an incorrect risk assessment with possibly fatal consequences to the concerned communities.

Model evaluation is often done over snow depth or snow water equivalent (SWE) measurements which are achieved at the same location the driver data was acquired, namely at the available meteorological stations. Data at steep slopes or other remote areas are usually not available for the evaluation of the model results as permanent measuring devices are usually not installed at these locations. For guaranteeing at least some spatial evaluation, field campaigns are conducted. Data of those campaigns is extremely valuable but has the drawback that it covers only one or a few moments in time.

As a result, it can be stated that either the available data sources for in situ evaluation are point sources with a good temporal but with a very limited spatial representativeness or field campaign data, which may cover the spatial distribution of the snow cover at a limited area very well but not its temporal development. This results in the need for a product, which allows for a derivation of the snow cover distribution in a high spatial and temporal resolution.

1.3 Satellite-based snow cover products

Data which does contain information on the dynamics of the mountain snow and ice cover at a larger scale and which is available for total catchment areas stems from satellite remote sensing systems. A wide range of satellite systems suited for environmental analysis has become available over the last decades (fig. 1.3-1). Optical satellite sensors are the most commonly used systems for snow cover mapping in hydrology today. Established ones are Landsat with a spatial resolution of 30 meters and MODIS with a spatial resolution of 500 meters. Snow maps are usually generated by utilizing algorithms of different complexity. These are used for translating the numeric information of a satellite scene into semantic information about the fact if there is snow on the ground or not. Most of these algorithms do

still rely on the simple normalized-difference snow index (NDSI) ratio approach. The NDSI uses the fact that snow does show unique reflection properties in the visible (VIS) and the mid-infrared (MIR) range of the electromagnetic spectrum. The reflection in the VIS, and especially in the green wavelength around 550 nm (GREEN), is thereby high when compared to other land cover types while the reflection in the MIR wavelength range around 1600 nm is relatively low.

The NDSI is hence formulated as:

$$NDSI = \frac{GREEN - MIR}{GREEN + MIR} \quad (1.3\text{-}1)$$

The resulting values are ranging between -1 and 1 and snow normally has a high NDSI value. However, a certain threshold value is needed for defining if a certain NDSI value means that a pixel is classified as snow-covered or not. This threshold is usually set to a value of 0.4 (Dozier, 1989; Hall et al., 1995). However, it is sometimes modified especially in course of studies which are focusing on the local scale, as it turned out that the standard value does lead to a bad performance of the resulting snow cover maps here. Nevertheless, these adaptations were mainly made on the basis of visual inspections and do therefore allow for the introduction of high uncertainties in the final snow maps as the judgement about the fact if a pixel is assumed to be snow-covered or not might differ between end-users which are working on satellite images in view of snow cover mapping. So, a user-independent objective approach for defining a locally valid NDSI threshold value is lacking. The publications, presented in the sections 2.3 and 2.4 of this thesis, address this issue as it does strongly affect the results of the established systems and therewith their heavily needed evaluation capabilities for hydrological model approaches. This is a major problem as high-quality snow cover maps are extremely helpful in view of the calibration or evaluation of models.

Besides the described uncertainties, optical satellite-based information does in general have the problem of a low temporal coverage. This is due to the fact that cloudy conditions can reduce the availability of satellite scenes to a significant extent. This is also reflected by the comparatively low amount of satellite scenes I have found for the analysis presented in section 2.4. But, model evaluation tasks do need high-quality data with a reliable repetition rate. This is not guaranteed by the available optical systems.

We can thus conclude that while remotely sensed data can provide information about the spatial snow cover extent at the catchment scale, it currently suffers from two problems. Firstly, the analysis scheme is either a fixed or subjective threshold which introduces unknown uncertainties in view of the snow cover extent and secondly, the repetition rate of the most commonly used satellite systems for snow cover mapping is still low, mainly because of the prevailing weather conditions in mountain regions.

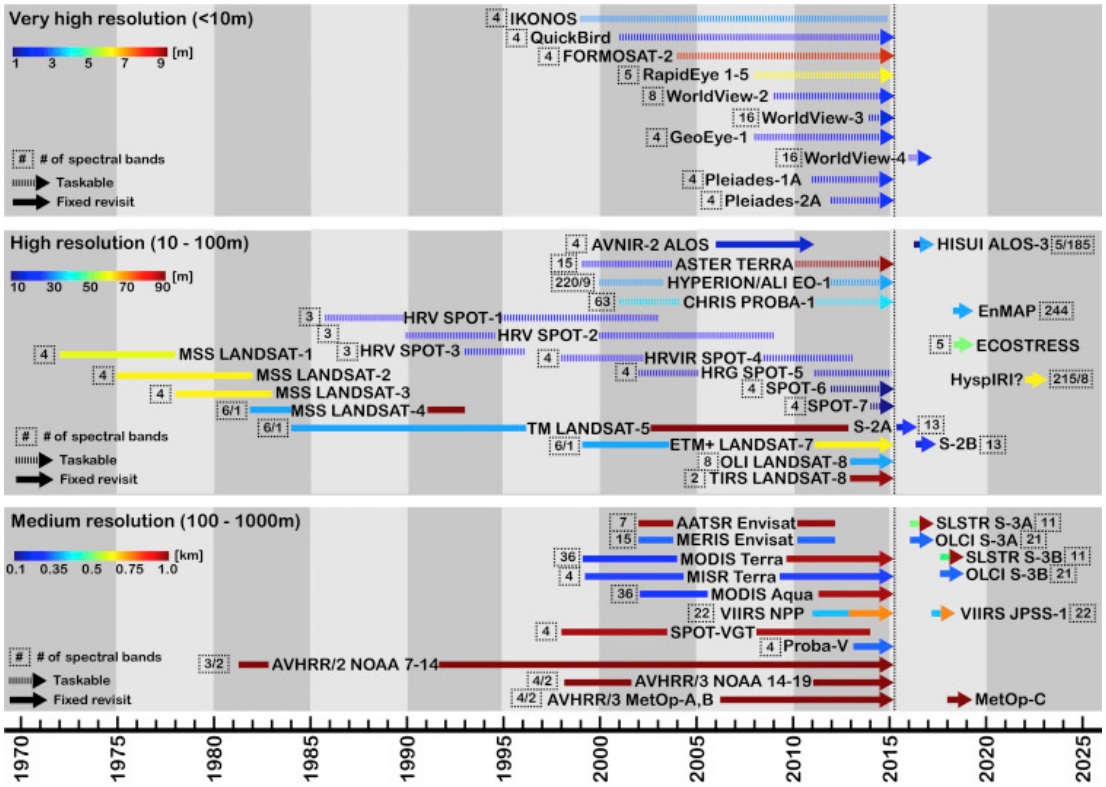

Figure 1.3-1: Timelines of historical and planned multi- and hyperspectral optical and thermal satellite sensors relevant for remote sensing of vegetation and snow at medium to very high spatial resolution (from Houborg et al., 2015).

References

Abermann, J., M. Kuhn, and A. Fischer: A reconstruction of annual mass balances of Austria's glaciers from 1969 to 1998, Ann. Glaciol., 52(59), 127–134, 2011.

Adamson, D., Mallawaarachchi, T., and Quiggin, J.: Declining inflows and more frequent droughts in the Murray-Darling Basin: climate change, impacts and adaptation, Aust. J. Agr. Resour. Ec., 53(3), 345–366, doi: 10.1111/j.1467-8489.2009.00451.x, 2009.

Afzal, M., Gagnon, A. S., and Mansell, M. G.: The impact of projected changes in climate variability on the reliability of surface water supply in Scotland, Water Sci. Tech-W. Sup., 15(4), 736–745, 10.2166/ws.2015.027, 2015.

AghaKouchak, A., Cheng, L. Y., Mazdiyasni, O., and Farahmand, A.: Global warming and changes in risk of concurrent climate extremes: Insights from the 2014 California drought, Geophys. Res. Lett., 41(24), 8847–8852, 10.1002/2014gl062308, 2014.

Ahmad, Z., Hafeez, M., and Ahmad, I.: Hydrology of mountainous areas in the upper Indus Basin, Northern Pakistan with the perspective of climate change, Environ. Monit. Assess., 184(9), 5255–5274, doi: 10.1007/s10661-011-2337-7, 2012.

Alexander, W. J. R.: Floods, Droughts and Climate-Change, S. Afr. J. Sci., 91(8), 403–408, 1995.

Armstrong, R. L., and Brun, E.: Snow and Climate: Physical Processes, Surface Energy Exchange and Modeling, Cambridge University Press, 2008.

Bao, Z. X., Fu, G. B., Wang, G. Q., Jin, J. L., He, R. M., Yan, X. L., and Liu, C. S.: Hydrological projection for the Miyun Reservoir basin with the impact of climate change and human activity, Quatern. Int., 282, 96–103, doi: 10.1016/j.quaint.2012.07.012, 2012.

Bavay, M., Lehning, M., Jonas, T., and Löwe, H.: Simulations of future snow cover and discharge in Alpine headwater catchments. Hydrol. Process., 23(1), 95–108. doi: 10.1002/hyp.7195, 2009.

Benestad, R. E., and Haugen, J. E.: On complex extremes: flood hazards and combined high spring-time precipitation and temperature in Norway, Climatic Change, 85(3-4), 381–406, doi: 10.1007/s10584-007-9263-2, 2007.

Bernhardt, M., and Schulz, K.: SnowSlide: A simple routine for calculating gravitational snow transport, Geophys. Res. Lett., 37, L11502, doi: 10.1029/2010gl043086, 2010.

Bernhardt, M., Liston, G. E., Strasser, U., Zängl, G., and Schulz, K.: High resolution modelling of snow transport in complex terrain using downscaled MM5 wind fields, The Cryosphere, 4(1), 99–113, doi: 10.5194/tc-4-99-2010, 2010.

Blöschl, G., Ardoin-Bardin, S., Bonell, M., Dorninger, M., Goodrich, D., Gutknecht, D., Matamoros, D., Merz, B., Shand, P., and Szolgay, J.: UNESCO Working Group on the impacts of climate variability and land-cover change on flooding and low flows as a function of scale, IAHS Publ., 308, 667–671, 2006.

Bookhagen, B., and Burbank, D. W.: Toward a complete Himalayan hydrological budget: Spatiotemporal distribution of snowmelt and rainfall and their impact on river discharge, J. Geophys. Res-Earth, 115, F03019, doi 10.1029/2009jf001426, 2010.

Bormann, K. J., Evans, J. P., and McCabe, M. F.: Constraining snowmelt in a temperature-index model using simulated snow densities, J. Hydrol., 517, 652–667, doi: 10.1016/j.jhydrol.2014.05.073, 2014.

Braithwaite, R. J.: Positive Degree-Day Factors for Ablation on the Greenland Ice-Sheet Studied by Energy-Balance Modeling, J. Glaciol., 41(137), 153–160, 1995.

Dozier, J.: Spectral signature of alpine snow cover from the Landsat Thematic Mapper, Remote Sens. Environ., 28, 9 Int. J. Remote Sens 22, doi:10.1016/0034-4257(89)90101-6, 1989.

Elsert, B., Heinrich, R., and Reich, G.: Wetterjahr 2013 - Wetter, Klima, Natur, Windturm Verlag, 2012.

Frei, C., and Schar, C.: A precipitation climatology of the Alps from high-resolution rain-gauge observations, Int. J. Climatol., 18(8), 873–900, doi: 10.1002/(SICI)1097-0088(19980630)18:8<873::AID-JOC255>3.0.CO;2-9, 1998.

Gosling, S. N., and Arnell, N. W.: A global assessment of the impact of climate change on water scarcity, Climatic Change, 134(3), 371–385, 10.1007/s10584-013-0853-x, 2016.

Groisman, P. Y., and Legates, D. R.: The Accuracy of United-States Precipitation Data, B. Am. Meteorol. Soc., 75, 215–227, doi: 10.1175/1520-0477(1994)075<0215:Taousp>2.0.Co;2, 1994.

Hall, D. K., Riggs, G. A., and Salomonson, V. V.: Development of methods for mapping global snow cover using moderate resolution imaging spectroradiometer data, Remote Sens. Environ., 54, 127–140, doi:10.1016/0034-4257(95)00137-P, 1995.

Hall, D. K., Riggs, G. A., Salomonson, V. V., DiGirolamo, N. E., and Bayr, K. J.: MODIS snow-cover products, Remote Sens. Environ., 83(1-2), 181–194, doi: 10.1016/S0034-4257(02)00095-0, 2002.

Härer, S., Bernhardt, M., Corripio, J. G., and Schulz, K.: PRACTISE - Photo Rectification And ClassificaTIon SoftwarE (V.1.0), Geosci. Model Dev., 6(3), 837–848, doi: 10.5194/gmd-6-837-2013, 2013.

Härer, S., Bernhardt, M., and Schulz, K.: PRACTISE – Photo Rectification And ClassificaTIon SoftwarE (V.2.1), Geosci. Model Dev., 9(1), 307–321, 10.5194/gmd-9-307-2016, 2016.

Houborg, R., Fisher, J. B., and Skidmore, A. K.: Advances in remote sensing of vegetation function and traits, Int. J. Appl. Earth Obs., 43, 1–6, doi: 10.1016/j.jag.2015.06.001, 2015.

Klemes, V.: Hydrology of mountainous areas, International IAHS workshop, 7-10 June 1988, Bratislava, Slovakia, 1988.

Klemes, V.: The modelling of mountain hydrology: the ultimate challenge, IAHS Publ., 190, 29–43, 1990.

Lehning, M., Grünewald, T., and Schirmer, M.: Mountain snow distribution governed by an altitudinal gradient and terrain roughness, Geophys. Res. Lett., 38, L19504, doi: 10.1029/2011gl048927, 2011.

Lehning, M., Volksch, I., Gustafsson, D., Nguyen, T. A., Stähli, M., and Zappa, M.: ALPINE3D: a detailed model of mountain surface processes and its application to snow hydrology, Hydrol. Process., 20(10), 2111–2128, doi: 10.1002/Hyp.6204, 2006.

Liston, G. E., and Elder, K.: A distributed snow-evolution modeling system (SnowModel), J. Hydrometeorol., 7(6), 1259–1276, doi: 10.1175/Jhm548.1, 2006.

Ma, H.: Snow cover monitoring and mapping using NOAA-AVHRR data, Arid Land Geogr., 21(3), 73–80. 1998.

Mankin, J. S., Viviroli, D., Singh, D., Hoekstra, A. Y., and Diffenbaugh, N. S.: The potential for snow to supply human water demand in the present and future, Environ Res. Lett., 10(11), 114016, doi: 10.1088/1748-9326/10/11/114016, 2015.

Marty, C.: Regime shift of snow days in Switzerland, Geophys. Res. Lett., 35, L12501, doi:10.1029/2008GL033998, 2008.

Pomeroy, J. W., Gray, D. M., Brown, T., Hedstrom, N. R., Quinton, W. L., Granger, R. J., and Carey, S. K.: The cold regions hydrological process representation and model: a platform for basing model structure on physical evidence, Hydrol. Process., 21(19), 2650–2667, doi: 10.1002/hyp.6787, 2007.

Pomeroy, J. W., Stewart, R. E., and Whitfield, P. H.: The 2013 flood event in the South Saskatchewan and Elk River basins: Causes, assessment and damages, Can. Water Resour. J., 41(1-2), 105–117, doi: 10.1080/07011784.2015.1089190, 2016.

Scherrer, S. C., Appenzeller, C., and Laternser, M.: Trends in Swiss Alpine snow days: the role of local- and large-scale climate variability, Geophys. Res. Lett., 31, L13215, doi:10.1029/2004GL020255, 2004.

Singer, F. S., and Pohham, R. W.: Non-meteorological observations from weather satellites, Astronaut. Aerosp. Eng., 1(3), 1963.

Staben, N., Nahrstedt, A., and Merkel, W.: Securing safe drinking water supply under climate change conditions, Water Sci. Tech-W. Sup., 15(6), 1334–1342, doi: 10.2166/ws.2015.099, 2015.

Tobin, C., Nicotina, L., Parlange, M. B., Berne, A., and Rinaldo, A.: Improved interpolation of meteorological forcings for hydrologic applications in a Swiss Alpine region, J. Hydrol., 401(1-2), 77–89, doi: 10.1016/j.jhydrol.2011.02.010, 2011.

Tolle, M. H., Moseley, C., Panferov, O., Busch, G., and Knohl, A.: Water supply patterns over Germany under climate change conditions, Biogeosciences, 10(5), 2959–2972, doi: 10.5194/bg-10-2959-2013, 2013.

Viviroli, D., Archer, D. R., Buytaert, W., Fowler, H. J., Greenwood, G. B., Hamlet, A. F., Huang, Y., Koboltschnig, G., Litaor, M. I., Lopez-Moreno, J. I., Lorentz, S., Schadler, B., Schreier, H., Schwaiger, K., Vuille, M., and Woods, R.: Climate change and mountain water resources: overview and recommendations for research, management and policy, Hydrol. Earth Syst. Sc., 15(2), 471–504, doi: 10.5194/hess-15-471-2011, 2011.

Viviroli, D., Dürr, H. H., Messerli, B., Meybeck, M., and Weingartner, R.: Mountains of the world, water towers for humanity: Typology, mapping, and global significance, Water Resour. Res., 43(7), W07447, doi: 10.1029/2006wr005653, 2007.

Wang, J.: Comparison and analysis on methods of snow cover mapping by using satellite remote sensing data, Remote Sens. Technol. Appl., 14(4), 29–30, 1999.

Wang, J., Li, H. X., Hao, X. H., Huang, X. D., Hou, J. L., Che, T., Dai, L. Y., Liang, T. G., Huang, C. L., Li, H. Y., Tang, Z. G., and Wang, Z. Y.: Remote sensing for snow hydrology in China: challenges and perspectives, J Appl. Remote Sens., 8, 084687, doi: 10.1117/1.Jrs.8.084687, 2014.

Whateley, S., Steinschneider, S., and Brown, C.: A climate change range-based method for estimating robustness for water resources supply, Water Resour. Res., 50(11), 8944–8961, doi: 10.1002/2014wr015956, 2014.

Winther, J. G., and Hall, D. K.: Satellite-derived snow coverage related to hydropower production in Norway: present and future, Int. J. Remote Sens., 20(15-16), 2991–3008, doi: 10.1080/014311699211570, 1999.

Zheng, P. N., Li, Z. Q., Bai, Z. P., Wan, L., and Li, X. T.: Influence of Climate Change to Drought and Flood, Disaster Adv, 5(4), 1331–1334, 2012.

II. Bridging the gap

Chapter I has clearly shown that data for predicting the spatiotemporal development of the snow storage in the Alpine is sparse and error-prone, especially where at the catchment scale. It cannot be expected that the available station network will be heavily extended during the next years, which requires alternative steps to broaden the available database. The main question which has arrived out of the circumstances described in chapter I was:

How can high-quality information about the snow cover dynamics be generated from already available data sources?

The information I was looking for should be suited for model evaluation at the sub-catchment scale at a high temporal resolution and it should be able to improve the quality of local satellite-derived snow maps as well.

An analysis of still available but potentially unused monitoring capabilities has directly lead to webcams. Products of those webcams have become freely available in an increasing number and quality over the last years. Hence, the challenge was to produce scientific data out of the available photographs. This was done by developing the software package PRACTISE (Photo Rectification And ClassificaTIon SoftwarE) which is able to create orthorectified high-resolution snow maps from the webcam images. It was then extended in a way that allows for the calibration of satellite snow maps and in course of this leads to the derivation of an objective NDSI threshold value from in situ data. The development and evaluation of the software package were done at the Environmental Research Station Schneefernerhaus (UFS) at Zugspitze. A final inter-comparison study has underlined the importance of local catchment specifics in view of a proper usage of satellite data. For doing so images of the Zugspitze and the Vernagtferner catchment were analysed and satellite scenes were optimized for these two catchments. The results have again shown that a location-specific evaluation method is vital for achieving valid information about the snow cover at the sub-catchment scale.

2.1 Publication I

The following text is an edited version of the 2013 Geoscientific Model Development (GMD) article:

PRACTISE – Photo Rectification And ClassificaTIon SoftwarE (v.1.0)

S. Härer[1], M. Bernhardt[1], J. G. Corripio[2] and K. Schulz[1]

[1] Department of Geography, LMU Munich, Germany

[2] meteoexploration.com, Innsbruck, Austria

Correspondence to: S. Härer (s.haerer@iggf.geo.uni-muenchen.de)

Abstract

Terrestrial photography is a cost-effective and easy-to-use method for measuring and monitoring spatially distributed land surface variables. It can be used to continuously investigate remote and often inaccessible terrain. We focus on the observation of snow cover patterns in high mountainous areas. The high temporal and spatial resolution of the photographs have various applications, for example validating spatially distributed snow-hydrological models. However, the analysis of a photograph requires a preceding georectification of the digital camera image. To accelerate and simplify the analysis, we have developed the "Photo Rectification And ClassificaTIon SoftwarE" (PRACTISE) that is available as a Matlab code. The routine requires a digital camera image, the camera location and its orientation, as well as a digital elevation model (DEM) as input. If the viewing orientation and position of the camera are not precisely known, an optional optimization routine using ground control points (GCPs) helps to identify the missing parameters. PRACTISE also calculates a viewshed using the DEM and the camera position. The visible DEM pixels are utilized to georeference the photograph which is subsequently classified. The resulting georeferenced and classified image can be directly compared to other georeferenced data and can be used within any geoinformation system. The Matlab routine was tested using observations of the north-eastern slope of the Schneefernerkopf, Zugspitze, Germany. The results obtained show that PRACTISE is a fast and user-friendly tool, able to derive the microscale variability of snow cover extent in high alpine terrain, but can also easily be adapted to other land surface applications.

1 Introduction

Oblique terrestrial photography has become a more and more frequently used observation method in various research disciplines, such as vegetation phenology (Richardson et al., 2007; Ahrends et al., 2008; Crimmins and Crimmins, 2008; Migliavacca et al., 2011), land cover studies (Clark and Hardegree, 2005; Zier and Baker, 2006; Roush et al., 2007; Michel et al., 2010) and volcanology (Major et al., 2009). Here, we focus on glaciology and snow hydrology where, for example, investigations of the snow albedo on glaciers were realized by Corripio (2004), Rivera et al. (2008) and Dumont et al. (2009). For a comprehensive overview of snowfall interception of vegetation, glacier velocity and snow cover mapping, we refer to Parajka et al. (2012). Terrestrial photography is used for these monitoring applications with an increasing frequency. This has to be attributed to the advancements in digital photography and in off-grid power supply. In addition, it is related to the fact that field campaigns and satellite-based remote sensing have limitations due to the prevailing weather conditions and the complexity of mountainous terrain (Klemes, 1990). Terrestrial photography offers an easy-to-use and inexpensive opportunity to monitor spatially distributed land surface characteristics, even in remote areas.

With the increasing availability of cost-effective high-resolution digital cameras and high-resolution digital elevation models, new tools can be developed to observe and map the patterns of land surface variables such as the spatial distribution of the snow cover in mountainous terrain. The main challenge for spatially distributed monitoring, however, is the georeferencing of a 2-D photograph to the 3-D reality. Tools, developed by Aschenwald et al. (2001) and Corripio (2004), addressed this problem by projecting the DEM to the camera image plane to establish a link between the photograph and the real world. Aschenwald et al. (2001) used a photogrammetric approach that needs various ground control points (GCPs) for the georectification process. This is, however, unfavourable in remote, mountainous terrain where the derivation of GCPs can be time-consuming and costly. Additionally, the integrated optimization procedure in their approach only optimizes the camera target position $\boldsymbol{T}$, i.e. the center position of the photograph, whereas all other parameters remain fixed. It should be noted here that $\boldsymbol{T}$ is known as the principal point in photogrammetry. The georectification method applied in Corripio (2004) is based on an animation and rendering technique by Watt and Watt (1992). This method only needs one

GCP (***T***), but 13 camera parameters have to be set. If these parameters are not accurately measured, they have to be manually corrected by changing them in an iterative way, which is unfavourable if extensive time series have to be processed.

The Photo Rectification And ClassificaTIon SoftwarE (PRACTISE) introduced here is based on the approach of Corripio (2004) but has been improved and extended by additional model features. We use slightly different formulations for the calculation of the 3-D rotation and projection. Even more importantly, several new optional routines are implemented in PRACTISE. This includes the dynamically dimensioned search (DDS) algorithm (Tolson and Shoemaker, 2007) to automatically identify the camera location and orientation using GCPs if the exterior and interior orientation parameters are not precisely known. Additionally, a viewshed algorithm (Wang et al., 2000) was integrated that simplifies and hastens the necessary visibility analysis by computing the viewshed directly without the additional step of using a geoinformation system, as is needed when using other georectification tools. PRACTISE also differs from existing software packages because it contains an automatic and a manual snow classification algorithm, and because a batch mode is implemented, i.e. several images can be classified in one program evaluation. As stated above, the routines described here are optional and the user selects the routines depending on the task and the available data. If, for example, the exact camera location and orientation of a photograph are known, the DDS optimization with the need for additional GCPs can be omitted. By contrary, the DDS routine is absolutely necessary for the georectification procedure if the parameters are not precisely known. The strength of PRACTISE is that the new features form a flexible, fast and user-friendly processing tool for analyzing spatially and temporally distributed land surface variables. A further strength is that the Matlab source code is freely available, and even though it is designed to classify the snow variability in mountainous terrain, it can be easily adapted to other fields of research, such as greenness indexes in phenology (Richardson et al., 2007; Ahrends et al., 2008; Crimmins and Crimmins, 2008; Migliavacca et al., 2011).

2 Data

The test area for PRACTISE is located near the Zugspitze mountain in the Alps (located in Bavaria, Germany, fig. 2.1-1a). A common single-lens reflex camera (SLR, Canon EOS 550D, Canon EF

17-40 mm f/4I USM objective lens) was installed at 2665 m a.s.l. at the Environmental Research Station Schneefernerhaus (UFS, fifth floor) which is located on the south slope of the Zugspitze. The camera was oriented towards the test area, on the northeast facing slope of the Schneefernerkopf summit (211000 m², fig. 2.1-1b). The skiing area on the glacier was excluded. During daylight, hourly images were taken from 10 May 2011 to 2 March 2012 (307 days). Some technical problems with the automatic timer reduced the number of days with available photographs to 245 (2061 photographs). The hourly frequency, however, increased the probability that at least one suitable image would be obtained per day, which resulted in about 180 days with potentially suitable photographs unaffected by weather and lighting conditions.

PRACTISE requires as inputs a DEM raster and the exterior orientation parameters of the camera: the camera position $\boldsymbol{C}$, the camera target position $\boldsymbol{T}$ and the roll φ of the camera. The latitude and longitude positions of $\boldsymbol{C}$ and $\boldsymbol{T}$ are sufficient as the altitude is taken from the corresponding DEM pixel during the computing process. If necessary, a camera offset o (installation height above the surface) is added to the altitude of $\boldsymbol{C}$, the combined altitude being referred to as $\boldsymbol{C}_\mathbf{o}$. Additionally, interior orientation parameters of the camera are necessary, such as the focal length f, as well as the sensor (CCD or CMOS) dimensions: height h and width w. We note here that lens distortions which can be significant are not taken into account in PRACTISE. Therefore, a high-quality objective lens was chosen that is known to have almost no distortion.

We selected three photographs to show the functionality of PRACTISE for different weather conditions and snow cover extents. The camera image taken on 11 May 2011 at 08:15 CEST (fig. 2.1-1b) represented the start of the ablation period in spring under clear sky conditions. The photograph from 16 August 2011, 11:05 CEST, was recorded under clear sky conditions in summer with almost no snow in the investigation area, whereas the photograph from 17 February 2012 at 15:07 CET described cloudy conditions directly after a snowfall event in winter.

The input given for the georectification and the classification of the photographs is presented in table 2.1-1. All camera-dependent parameters were taken from the user manual of the Canon camera system. Using the best resolution (17.9 Mpx), the pixel dimensions of the photographs are vertically

3456 px (N_v) and horizontally 5184 px (N_h). The latitude and longitude positions of ***C*** and ***T*** were visually derived from an official orthophoto from September 2009 with a spatial resolution of 0.2 m provided by the Bavarian State Office for Survey and Geoinformation. The UFS building where the camera is located is clearly identifiable in the orthophoto, while the coordinates of ***T*** are estimated by comparing the orthophoto with a photograph from September 2011.

Table 2.1-1: Initial input data of PRACTISE for the test site Schneefernerkopf. The coordinates are referenced to the European Terrestrial Reference System 1989 (ETRS89) and UTM Zone 32T. The values are in m except noted otherwise.

Parameter name	Original input
C_x	649 299.97
C_y	5 253 358.26
T_x	648 740.85
T_y	5 252 771.33
o	1.5
φ [°]	0
f	0.031
h	0.0149
w	0.0223
N_v [px]	3456
N_h [px]	5184

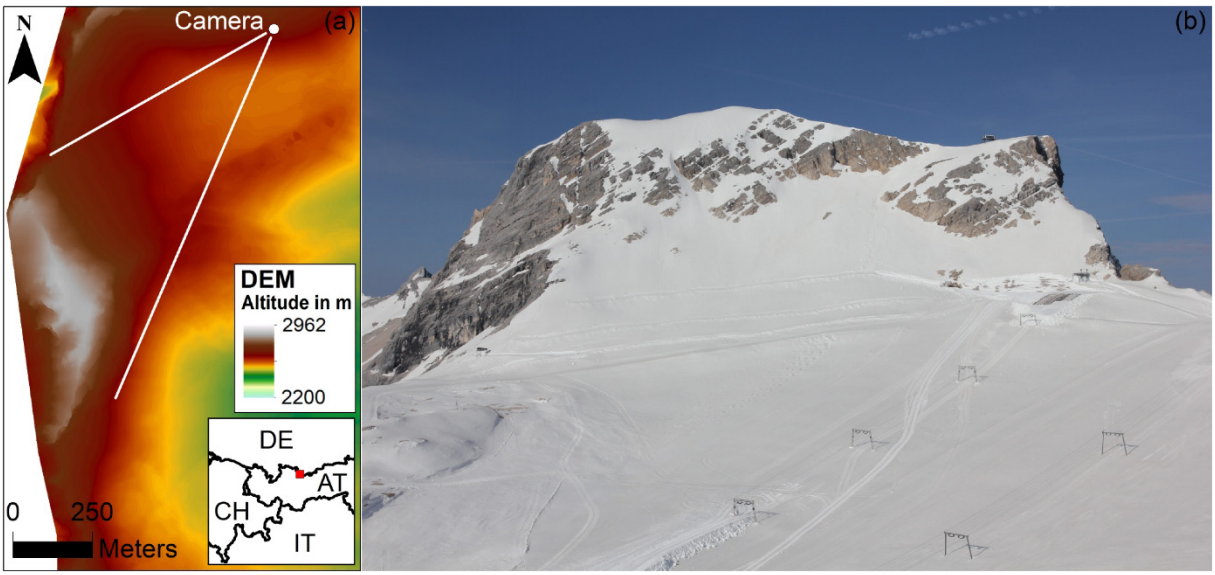

Figure 2.1-1: (a) The test site of PRACTISE is located at the Schneefernerkopf which is situated in southern Germany, at the border to Austria (right frame). The DEM depicts the camera location and the field of view of the camera. (b) The installed digital camera system records hourly photographs of the investigation area, the north-eastern slope of the Schneefernerkopf summit (upper central area).

Other techniques to obtain the coordinates of $\boldsymbol{C}$ and $\boldsymbol{T}$ might also be possible, for example with a standard GPS device. The parameters o, φ and f were estimated after the installation of the camera system. The DEM used had a spatial resolution of 1 m in the horizontal plane and originated from an airborne laser scanning campaign in 2006 by the Martin Luther University Halle–Wittenberg. Both the orthophoto and the DEM are referenced to the European Terrestrial Reference System 1989 (ETRS89) and UTM (Universal Transverse Mercator) Zone 32T.

The available input data for the camera location and orientation is subject to considerable uncertainty as it was not accurately measured using for example a differential GPS system. Furthermore, the camera was moved between the images. The DDS optimization utilizing GCPs was applied to improve the exterior and interior orientation parameters of each photograph. The GCPs of each photograph were determined by using the orthophoto in combination with the DEM for the longitude, latitude and altitude as well as the photograph with the row and column information.

3 Model routines

PRACTISE is programmed in Matlab and divided into four modules that are presented in the following subsections. The partitioning of the software in different routines provides a maximum of flexibility as the user can decide depending on the task and available data which features are necessary and have to be activated or if a new routine has to be implemented. In the default case, the camera location and orientation are precisely known. PRACTISE starts with the viewshed generation (subsect. 3.1). Subsequently, the georectification procedure is applied (subsect. 3.2) and finally the snow classification is executed (subsect. 3.4). In our study, however, the exterior and interior orientation parameters of the camera are estimated. Hence, all routines are activated. In this case, PRACTISE begins by assessing the accuracy of the GCPs (subsect. 3.3) where it utilizes the georectification routine (subsect. 3.2) to compute the deviations between the georeferenced and real positions of the GCPs. Next, the DDS algorithm reduces the positional inaccuracy by optimizing the camera parameters (subsect. 3.3). From this point, the default procedure is followed, as described above. In each subsection, we will show the processing steps based on the photograph of 11 May 2011 at 08:15 CEST (fig. 2.1-1b).

3.1 Viewshed

In a first step, PRACTISE identifies the pixels of the DEM which are visible from the camera location. This is necessary because pixels of the digital image can only be attributed to those DEM pixels. Note that the spatial resolution of the DEM determines the detail of the results. The implemented viewshed calculation is an optional feature that can be bypassed if a viewshed is externally provided, for example from geoinformation software.

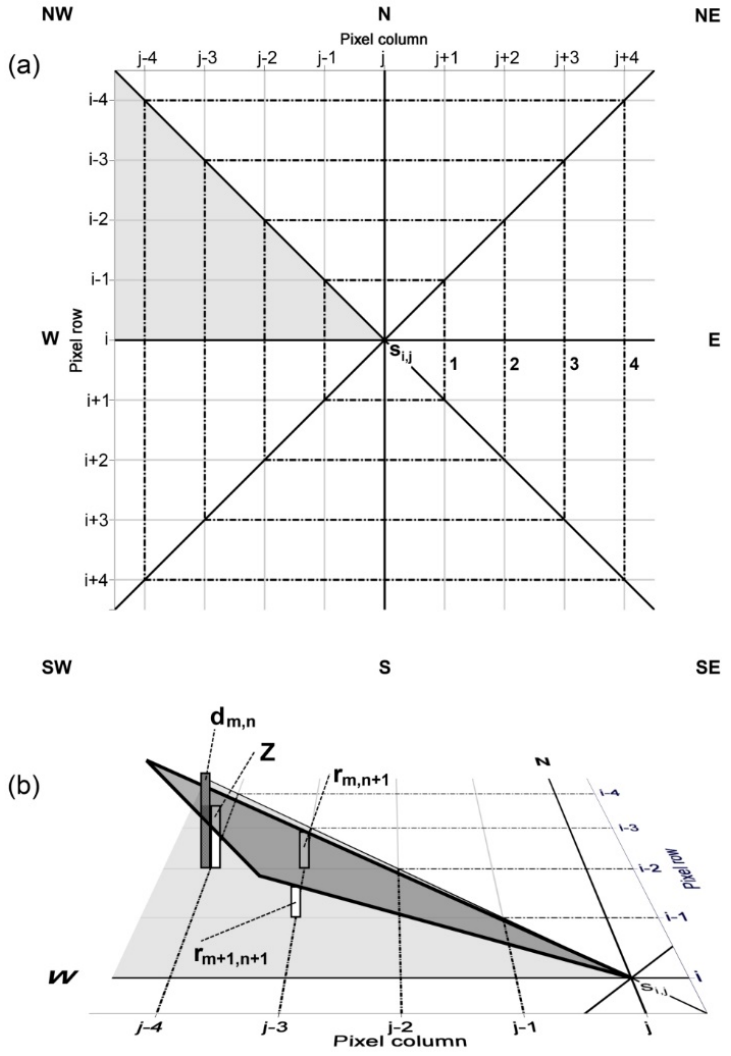

Figure 2.1-2: (a) The viewshed calculation is divided into eight sectors based on the compass directions N, NE, E, SE, S, SW, W and NW (black lines) from the point $s_{i,j}$. The DEM pixels are attributed to a certain ring (1, 2, 3, 4, ..., black dotted lines) depending on the pixel distance to $s_{i,j}$. (b) The "reference planes" concept of Wang et al. (2000) is evaluated subsequently from the inner to the outer rings and is shown for an example in the fourth ring of the grey-shaded W-NW sector. The normalized camera position $s_{i,j}$, as well as the neighbouring pixels $r_{m,n+1}$ and $r_{m+1,n+1}$ (third ring) create a plane that checks if the pixel with the normalized elevation value $d_{m,n}$ is visible. In this case, $d_{m,n}$ is visible as the plane height Z at row m and column n is lower (adapted from Wang et al., 2000).

The viewshed generation is based on the "reference planes" concept (Wang et al., 2000) and requires a DEM raster and the camera position $\boldsymbol{C_o}$. By definition, only the horizontal centers of DEM pixels are utilized in the visibility analysis and the origin of the raster grid is in the northwestern (NW) corner. Indices *i* and *m* refer to the row positions of DEM pixels, and indices *j* and *n* indicate the column positions.

The viewshed calculation is divided into eight sectors based on the compass directions N, NE, E, SE, S, SW, W and NW. At first, the elevation of the DEM coordinate system is modified by setting the elevation of $\boldsymbol{C_o}$ to zero. The normalized camera position simplifies the plane generation and is referred to as $s_{i,j}$ (fig. 2.1-2a). The algorithm starts the visibility analysis at the DEM pixels in the second ring and proceeds stepwise to the cells of the outer rings. All pixels in the first ring are assumed to be visible, since no obstacles to $s_{i,j}$ are evident. The general functionality of the method is shown by using the example of the west-northwest (W-NW) sector (shaded area in figs. 2.1-2a and 2.1-2b).

Three pixel values define the plane which builds the criteria for visibility (Z) for the destination point $d_{m,n}$. These pixels are the normalized camera position $s_{i,j}$ as well as the neighbouring pixels $r_{m,n+1}$ and $r_{m+1,n+1}$. Both, $r_{m,n+1}$ and $r_{m+1,n+1}$, lie on the adjacent inner ring of $d_{m,n}$, i.e. the third ring in fig. 2.1-2b. Additionally, these two points have the shortest distance to $s_{i,j}$ and to $d_{m,n}$ on that ring. The values of $r_{m,n+1}$ and $r_{m+1,n+1}$ represent the maximum height of either the normalized elevation at this raster position or, in relative terms, higher obstacles in the already calculated inner rings in between to $s_{i,j}$.

Z is then derived as follows:

$$Z = -(m-i)\left(r_{m,n+1} - r_{m+1,n+1}\right) + \frac{(n-j)\left((m-i)(r_{m,n+1}-r_{m+1,n+1})+r_{m,n+1}\right)}{n+1-j}. \quad (2.1\text{-}1)$$

The calculation of the main directions is simplified since the reference plane (eq. 2.1-1) can be reduced to a "reference line" (eq. 2.1-2). This is shown for the NW diagonal:

$$Z = r_{m+1,n+1}\frac{i-m}{i-m-1}. \quad (2.1\text{-}2)$$

A pixel is considered as visible if

$$d_{m,n} > Z.$$

In this case the value of $d_{m,n}$ is assigned to $r_{m,n}$ for further calculations in the adjacent outer ring, otherwise the pixel is invisible and $r_{m,n}$ is set to the value of Z. The next visibility check will be executed at $d_{m-1,n}$ (fig. 2.1-2b). Other directions and sectors are calculated in a similar way.

The algorithm of Wang et al. (2000) was developed to generate a 360-degree viewshed. Assuming a central projection of the camera lens, we use the viewing direction as well as the horizontal and vertical field of view and thus only compute the areas depicted in the photographs. Here, we additionally need the camera target position $\boldsymbol{T}$ and the interior orientation parameters of the camera f, h and w. The viewing direction is set by connecting $\boldsymbol{C_o}$ and $\boldsymbol{T}$. The interior orientation parameters are necessary to calculate the corresponding horizontal and vertical field of view. A maximum vertical viewing angle α_v to the viewing direction can be calculated as follows:

$$\alpha_v = \pm \arctan\left(\frac{\frac{1}{2}h}{f}\right). \tag{2.1-3}$$

The maximum horizontal viewing angle α_h of the photograph is calculated by replacing the height h by the width w in eq. (2.1-3). The vertical or horizontal orientation of a camera image might be different to the real-world vertical or horizontal orientation due to φ.

Figure 2.1-3 shows the viewshed in this case study.

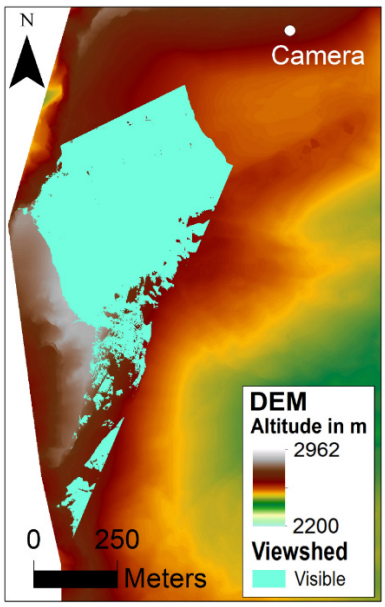

Figure 2.1-3: The optional viewshed feature of PRACTISE computes the visible pixels (cyan) using the corresponding camera location and orientation.

3.2 Georectification

PRACTISE uses an animation and rendering technique to georectify the visible DEM pixels (Watt and Watt, 1992). The principle behind the georectification process is illustrated in fig. 2.1-4. The camera produces a 2-D representation of the 3-D landscape. The oblique and two-dimensional image lacks depth information: therefore, a direct back-calculation of the 2-D information into a 3-D landscape is impossible. A method for calculating it is to generate a 2-D virtual camera image of the DEM while conserving the real-world position of any pixel. The RGB (red, green, blue) values of the camera can then be assigned to the virtual 2-D image. Afterwards, any pixel with the attached RGB information is retransformed to its real-world position.

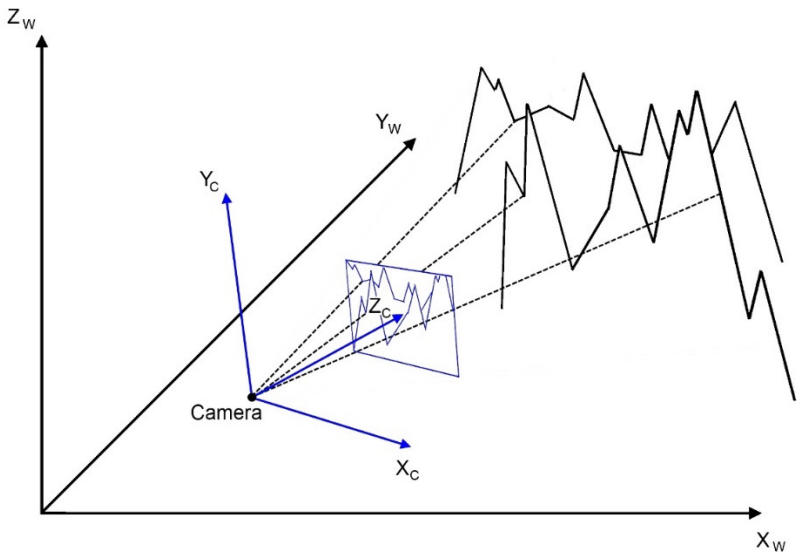

Figure 2.1-4: The principle of the georectification procedure is as follows: at first, the mountain massif in the real world coordinate system (XYZ_W, black) is translated and rotated to the camera coordinate system (XYZ_C, blue). Then, the 3-D mountain landscape is projected to a 2-D virtual camera image utilizing the central projection of the camera lens (adapted from Corripio et al., 2004).

The georectification is shown for a single DEM pixel, whereas all visible pixels are successively processed in the same way. Given the fact that the pixel is visible from $\boldsymbol{C_o}$, its center point coordinates $\boldsymbol{P_w}$ is derived and saved in a vector:

$$\boldsymbol{P_w} = \begin{bmatrix} P_{wx} \\ P_{wy} \\ P_{wz} \end{bmatrix}. \qquad (2.1\text{-}4)$$

The transformation of the real-world coordinates of the DEM into the camera coordinate system is achieved by a translation of the origin of the coordinate system to the camera position $\boldsymbol{C_o}$ and a subsequent multiplication of the translated pixel coordinates with a rotation matrix:

$$\boldsymbol{P_t} = \begin{bmatrix} P_{tx} \\ P_{ty} \\ P_{tz} \end{bmatrix} = \begin{bmatrix} P_{wx} \\ P_{wy} \\ P_{wz} \end{bmatrix} - \begin{bmatrix} C_{ox} \\ C_{oy} \\ C_{oz} \end{bmatrix}, \tag{2.1-5}$$

$$\boldsymbol{P_c} = \begin{bmatrix} P_{cx} \\ P_{cy} \\ P_{cz} \end{bmatrix} = \begin{bmatrix} U_x & U_y & U_z \\ V_x & V_y & V_z \\ N_x & N_y & N_z \end{bmatrix} \begin{bmatrix} P_{tx} \\ P_{ty} \\ P_{tz} \end{bmatrix}. \tag{2.1-6}$$

The unit vectors $\boldsymbol{U}$, $\boldsymbol{V}$ and $\boldsymbol{N}$ describe the axis of the new camera coordinate system (fig. 2.1-5), where $\underline{\boldsymbol{N}}$ points in the viewing direction. Vectors $\boldsymbol{U}$ and $\boldsymbol{V}$ are the horizontal and vertical axis of the camera system and create a plane that is parallel to the image plane (figs. 2.1-4 and 2.1-5).

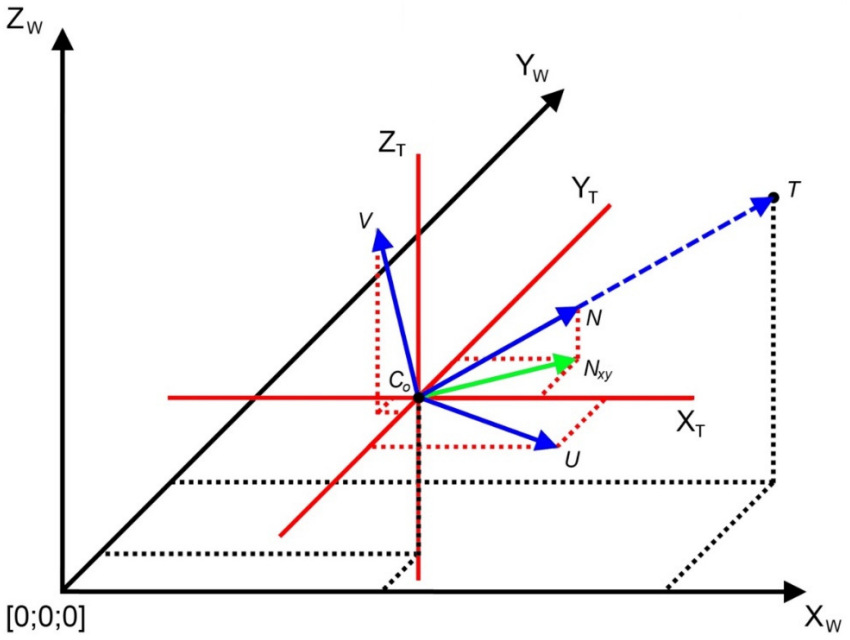

Figure 2.1-5: The mathematical components of the translation and rotation of the real world coordinate system (XYZ_W, black) can be derived using vector calculus. The translated real world coordinate system (XYZ_T, red) is determined by setting $\boldsymbol{C_o}$ as coordinate system origin. The connection line from $\boldsymbol{C_o}$ to $\boldsymbol{T}$ forms the vector of the viewing direction which is subsequently normalized ($\boldsymbol{N}$). The unit vector $\boldsymbol{U}$ is derived by the cross product of $\boldsymbol{N}$ and the unit vector of $\boldsymbol{N_{xy}}$ (green) where N_{xy} is the projection of $\boldsymbol{N}$ to the XY_T plane. The directions of the camera coordinate system (blue) are spanned by $\boldsymbol{N}$, $\boldsymbol{U}$ and $\boldsymbol{V}$ where $\boldsymbol{V}$ is the cross product of $\boldsymbol{U}$ and $\boldsymbol{N}$ (adapted from Corripio, 2004).

The calculation of $\boldsymbol{N}$ is performed on the basis of the real-world coordinates of $\boldsymbol{C_o}$ and $\boldsymbol{T}$:

$$\boldsymbol{N} = \frac{\boldsymbol{T}-\boldsymbol{C_o}}{|\boldsymbol{T}-\boldsymbol{C_o}|}. \tag{2.1-7}$$

Following Corripio (2004), we use cross products to calculate $\boldsymbol{U}$ and $\boldsymbol{V}$ (fig. 2.1-5), if $\boldsymbol{N_z} \neq 0$:

$$\boldsymbol{U} = \begin{cases} \boldsymbol{N} \times \frac{\boldsymbol{N_{xy}}}{|\boldsymbol{N_{xy}}|} \text{ for } \boldsymbol{N_z} > 0 \\ \frac{\boldsymbol{N_{xy}}}{|\boldsymbol{N_{xy}}|} \times \boldsymbol{N} \text{ for } \boldsymbol{N_z} < 0 \end{cases}, \tag{2.1-8}$$

$$\boldsymbol{V} = \boldsymbol{U} \times \boldsymbol{N}, \tag{2.1-9}$$

where $\boldsymbol{N_{xy}} = [N_x, N_y, 0]$. We extend the calculation to the situation where $\boldsymbol{N} = \boldsymbol{N_{xy}}$, i.e. $N_z = 0$. In this particular case, we set $\boldsymbol{V} = [0,0,1]$, and calculate $\boldsymbol{U}$ by computing the cross product of $\boldsymbol{V}$ and $\boldsymbol{N}$.

In the case of the camera not being completely levelled, an additional rotation of the coordinates around $\boldsymbol{N}$ is required:

$$\boldsymbol{P_{cr}} = \begin{bmatrix} P_{crx} \\ P_{cry} \\ P_{crz} \end{bmatrix} = \begin{bmatrix} \cos(\varphi) & \sin(\varphi) & 0 \\ -\sin(\varphi) & \cos(\varphi) & 0 \\ 0 & 0 & 1 \end{bmatrix} \begin{bmatrix} P_{cx} \\ P_{cy} \\ P_{cz} \end{bmatrix}, \tag{2.1-10}$$

where the roll φ is defined from 0° to ±90°, where the positive values turn the $\boldsymbol{U}$-$\boldsymbol{V}$ plane in the viewing direction clockwise, and the negative values turn it anticlockwise.

The last step of the georectification is the projection of the rotated coordinates $\boldsymbol{P_{cr}}$ to the image plane p. The three coordinate values of the DEM pixel determine the position in the camera space, where P_{crx} as well as P_{cry} hold the horizontal and vertical information and P_{crz} the depth information. In contrast to Corripio (2004), we reduce the 3-D problem ($\boldsymbol{P_{cr}}$ to $\boldsymbol{P_p}$) to two 2-D problems: a horizontal (P_{crx} to P_{px}) and a vertical (P_{cry} to P_{py}) one. We solve each of them in two steps. At first, we directly apply the intercept theorem to calculate the horizontal (and vertical) component of the photograph at the CCD sensor plane s:

$$P_{sx} = \frac{P_{crx}}{P_{crz}} \cdot f, \tag{2.1-11}$$

where f is the focal length. P_{sy} is calculated by replacing P_{crx} with P_{cry}. It should be noted that the intercept theorem is applicable here, as $\boldsymbol{T}$ is located at $[0,0,P_{crz}]$ in the camera coordinate system and thus lies in the center of the photograph.

As a second step, P_{sx} and P_{sy} are scaled to the image plane p using the number of pixels N_h and N_v of the photograph in the horizontal and vertical directions:

$$P_{px} = \frac{N_h}{\frac{1}{2}w} \cdot P_{sx} \,, \tag{2.1-12}$$

where w is the camera sensor width. P_{py} is computed in the same way but under usage of N_v and the CCD height h. Both, the photograph and the projected DEM are now in-plane. The last step is to shift the origin of the virtual camera image from $[N_h/2,N_v/2]$ to the origin of the photograph $[0,0]$. This is necessary as the photograph origin lies at the upper left corner while the projected DEM coordinate system is centered in the photograph. The overlay of the images facilitates the direct extraction of the RGB values for the classification which can be directly retransformed to the raster format of the DEM.

Figure 2.1-6 shows the overlay of the georectified DEM pixels and the photograph.

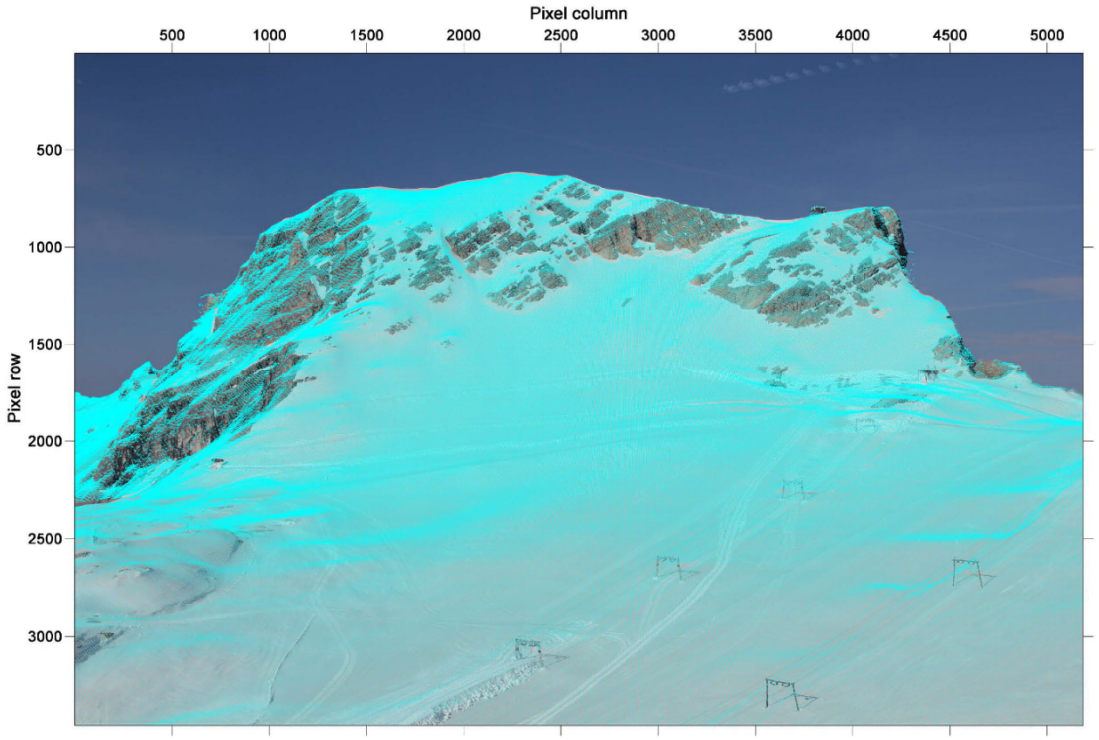

Figure 2.1-6: The georectification of the visible DEM pixels (fig. 2.1-3) is superimposed with cyan dots on the corresponding photograph.

3.3 GCP accuracy assessment and DDS optimization

PRACTISE offers an optional feature to enhance the exterior and interior orientation parameters of the camera used in the georectification procedure if the camera parameters are not precisely known. In that case, GCPs are required to determine and to reduce the positional inaccuracy of the virtual camera image to the photograph. The root mean square error (RMSE) is used as an error metric.

We implemented a global optimization approach, the dynamically dimensioned search (DDS) algorithm (Tolson and Shoemaker, 2007), to minimize the displacement between the georeferenced and real locations of the GCPs. We selected this technique because Tolson and Shoemaker (2007) state that, for calibration problems between 6 and 30 dimensions and with a limited number of function evaluations (1000 to 10000), it produces equally good or even better results than the frequently used shuffled complex evolution (SCE) optimization. The general procedure of the implemented DDS algorithm is shown in table 2.1-2.

Within the optimization procedure, seven decision variables are optimized: the latitude and longitude of $\boldsymbol{C}$ and $\boldsymbol{T}$, the camera offset o, the roll φ, and the focal length f. The inclusion of f in the optimization is necessary as the actual and nominal focal length of a camera lens will probably differ slightly. The initial estimates of the decision variables x^0 are taken from the original input (table 2.1-1). Additionally, the user has to define the upper and lower boundaries (x^{max} and x^{min}) that span the range of reasonable values (table 2.1-3). Finally, the maximum number of function evaluations M is specified. Six GCPs are used in the DDS optimization example.

The algorithm starts with the georectification of the GCPs using x^0 and creates an initial $x^{best} = x^0$. Then, x^{new} is randomly generated (table 2.1-2) and if the recalculation of the RMSE(x^{new}) results in a lower RMSE than RMSE(x^{best}), x^{best} is updated with x^{new}. The optimization procedure stops when the number of iterations is equal to M and subsequently the georectification of the DEM with the best camera orientation (table 2.1-3) starts. In this example, $M = 3000$ as no large improvements have been observed with more iterations. At least one recalculation is recommended to verify that the global optimum was found.

Table 2.1-2: Working steps of the implemented DDS algorithm in PRACTISE (adapted from Tolson and Shoemaker, 2007).

Step 1	Define DDS inputs:
	Vector of initial solution $\boldsymbol{x}^0 = [x_1, \ldots, x_7]$
	Vectors of upper, $\boldsymbol{x}^{max}$, and lower, $\boldsymbol{x}^{min}$, boundaries for the 7 decision variables
	Maximum number of function evaluations m
	Neighbourhood perturbation size parameter r (0.2 is default)
Step 2	Set counter to 1, i =1, and evaluate RMSE at initial solution RMSE$(\boldsymbol{x}^0)$:
	$RMSE_{best}$ =RMSE$(\boldsymbol{x}^0)$, and $\boldsymbol{x}^{best} = \boldsymbol{x}^0$
Step 3	Randomly select J of the D decision variables for inclusion in neighbourhood $\{N\}$:
	Calculate probability each decision variable is included in $\{N\}$ as a function of the current iteration count: $P(i) = 1 - \ln(i)/\ln(m)$
	FOR d =1, …, D decision variables, add d to $\{N\}$ with probability P
	IF $\{N\}$ empty, select one random d for $\{N\}$
Step 4	FOR j=1, …, J decision variables in {N}, perturb $\boldsymbol{x}_j^{best}$ using a standard normal random variable $N(0,1)$, reflecting at decision variable bounds if necessary:
	$x_j^{new} = x_j^{best} + \sigma_j N(0,1)$, where $\sigma_j = r(x_j^{max} - x_j^{min})$
	IF $x_j^{new} < x_j^{min}$, reflect perturbation: $x_j^{new} = x_j^{min} + (x_j^{min} - x_j^{new})$ IF $x_j^{new} > x_j^{max}$, set $x_j^{new} = x_j^{min}$
	IF $x_j^{new} > x_j^{max}$, reflect perturbation: $x_j^{new} = x_j^{max} - (x_j^{new} - x_j^{max})$ IF $x_j^{new} < x_j^{min}$, set $x_j^{new} = x_j^{max}$
Step 5	Evaluate RMSE$(\boldsymbol{x}^{new})$ and update current best solution if necessary:
	IF RMSE$(\boldsymbol{x}^{new}) \leq RMSE_{best}$, update new best solution: $RMSE_{best}$=RMSE$(\boldsymbol{x}^{new})$ and $\boldsymbol{x}^{best} = \boldsymbol{x}^{new}$
Step 6	Update iteration count, $i = i + 1$, and check stopping criterion:
	IF $i = m$, STOP, print output ($RMSE_{best}$ and $\boldsymbol{x}^{best}$)
	ELSE go to Step 3

Table 2.1-3: Vectors of the DDS optimization example with 3000 iterations: x^0, x^{max}, x^{min} and x^{best}. The values are in m except noted otherwise. x^{max} of $\boldsymbol{C}$ is set to the values of x^0 as the UFS building is represented in the DEM by a plateau. Hence, we confine the optimization directions to stay at the edge or in front of the building. The latter needs a large camera offset to obtain the height of the fifth floor of the UFS.

	$\boldsymbol{x}^0$	$\boldsymbol{x}^{max}$	$\boldsymbol{x}^{min}$	$\boldsymbol{x}^{best}$
C_x	649 299.97	649 299.97	649 294.97	649 299.83
C_y	5 253 358.26	5 253 358.26	5 253 353.26	5 253 356.6
T_x	648 740.85	648 765.85	648 715.85	648 741.86
T_y	5 252 771.33	5 252 796.33	5 252 746.33	5 252 768.71
o	1.5	26.5	1	6.35
φ [°]	0	2	-2	1.37
f	0.031	0.036	0.026	0.0302

Figure 2.1-7 depicts the correct position of the six GCPs (green crosses) in comparison to the georectification of the GCPs before and after the DDS optimization (red circles and dots).

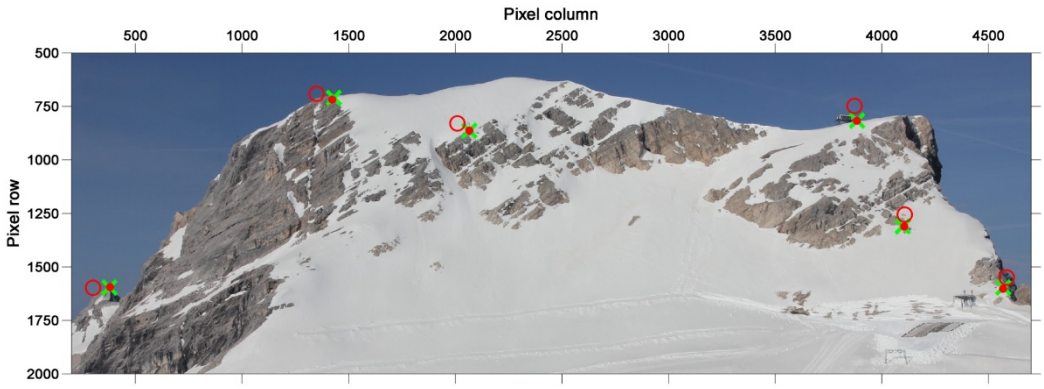

Figure 2.1-7: The correct GCP positions are depicted as green crosses in the enlarged view of the photograph. The georectification using x^0 is shown by the red circles while the red dots illustrate the georectification after the DDS optimization ($M = 3000$) using x^{best}.

3.4 Classification

Here, we focus on the classification of snow cover even though the investigation of other land surface variables is possible and only needs slight adaptions of the respective routine. Two classification routines of different complexity can be used. The first is based on threshold values, which have to be manually derived by analyzing the RGB values of the snow cover and of the surrounding environment in the photograph. The second is an automatic snow cover classification routine (Salvatori et al., 2011), that has not been used in quantitative snow cover mapping before but is able to hasten the classification, in particular of long time series.

The manual classification assigns snow to pixels with RGB values above certain thresholds. The threshold values can be in between 0 and 255 if 8-bit data is used and are often around 150 for all bands. The predefined thresholds vary from image to image as the lighting conditions change and as we want to classify fresh snow (pure white), as well as old snow which turns grey with time. In general, snow has a similar reflectance within the RGB bands, while the reflectance values of, for example, light-coloured bare rocks are significantly lower in the blue band. Hence, we introduced a test that verifies if the spread between the RGB values of one pixel does not exceed a specified threshold (for example 10).

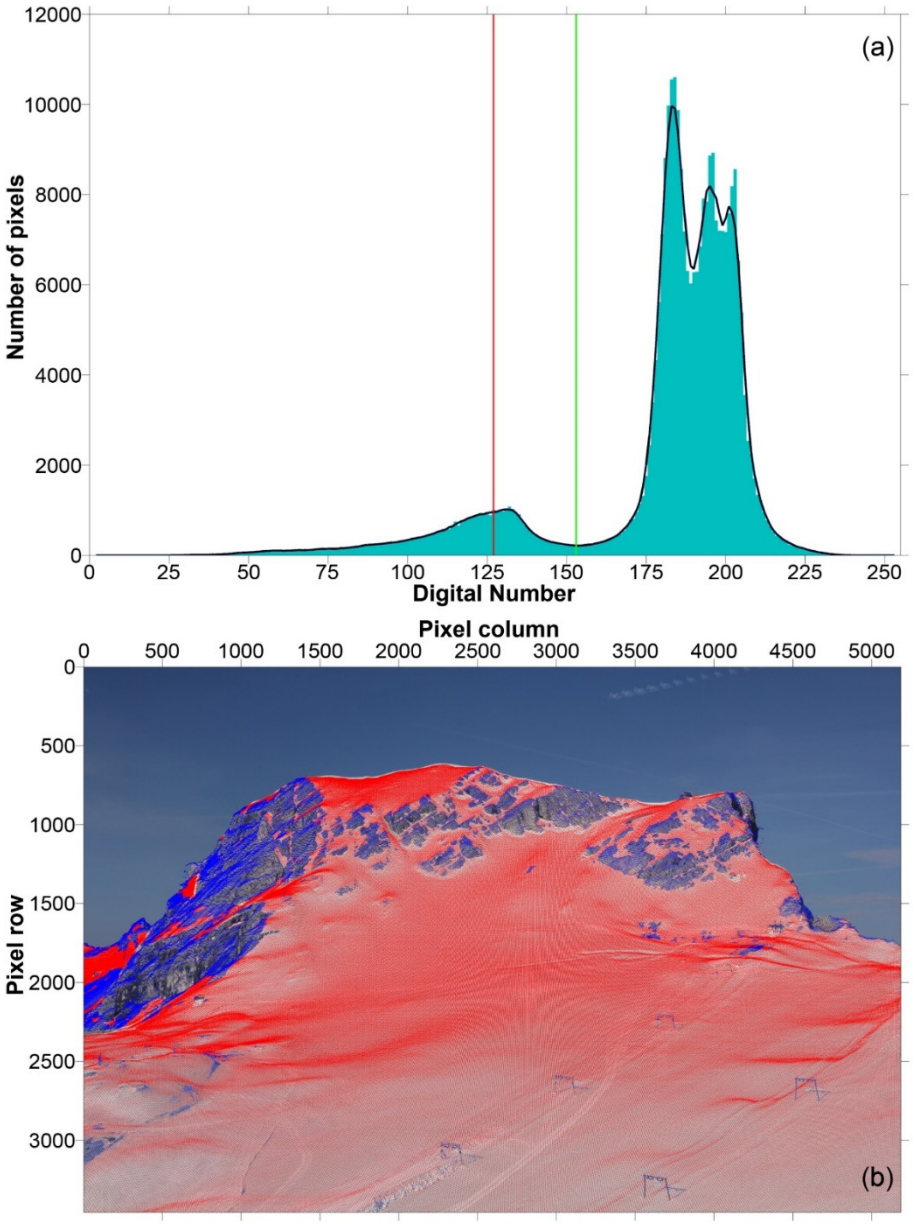

Figure 2.1-8: (a) The automatic snow classification in PRACTISE creates a DN frequency histogram of the blue band values (blue-green bars) of the superimposed DEM pixel positions (Fig. 2.1-6). The distribution is smoothed with a moving average window size of 5 (black line) and the snow threshold (green line) is selected for the first local minimum beyond a DN ≥ 127 (red line). (b) In the overlay, all DEM pixels with a DN in the blue band in the range from the snow threshold to 255 are classified as snow (red dots), while all other pixels are assigned as no snow (blue dots).

The automatic classification of Salvatori et al. (2011) incorporates a statistical analysis of the image by using a DN (digital number) frequency histogram (fig. 2.1-8a). The algorithm uses the blue band exclusively because of the assumption that it is representative of the other bands with respect to snow. In the presence of snow, the histogram usually shows a bimodal distribution. The first local minimum

over or equal to 127 is selected as the snow threshold (fig. 2.1-8a). The DN frequency histogram has to be smoothed for this analysis by using a moving average window of 5. This is done for removing single outliers, which might be mistakenly interpreted as local minima. Salvatori et al. (2011) defined the size of the moving window as well as of the minimum histogram threshold of the blue band, on the basis of about 300 images. The resulting classification is shown in fig. 2.1-8b.

The structure of PRACTISE also allows for an inclusion of already classified images and of other routines. For example, Hinkler et al. (2002) present a calibrated index similar to the normalized-difference snow index in satellite remote sensing (Dozier, 1989) to identify snow cover and areas free of snow, while Schmidt (2007) uses manually determined thresholds and additional masks of shadows, vegetation and topographic features. In the studies of Corripio (2004) and Corripio et al. (2004), the albedo of glacier and snow surfaces is calculated using an atmospheric transmittance model. Algorithms for the investigation of other land surface variables are likewise possible. The implementation of any existing or self-programmed routines in PRACTISE can also be accomplished with limited programming skills.

4 Results and discussion

The functionality of PRACTISE will be demonstrated using the test area of Schneefernerkopf, Zugspitze on the basis of three photographs which are hereinafter referred to as the May (11 May 2011 at 08:15 CEST), the August (16 August 2011, 11:05 CEST) and the February (17 February 2012 at 15:07 CET) images. All routines described above are used to compute the snow cover extent. The DDS optimization is necessary as the exact camera location and orientation was not measured but estimated from an orthophoto. Further, the camera was slightly moved between each photograph. The runtime per photograph is about 40 s using computing power similar to an Intel Pentium 4 with 3 GHz.

In the DDS optimization, we found an initial RMSE of 67.82 px between the GCPs and the control points within the May photograph (table 2.1-3, x^0). The error could be reduced to 4.42 px by using the optimized input (table 2.1-3, x^{best}). The RMSE after the optimization procedure for the August and February images are 6 and 5.49 px, whereas the initial error values are 43.45 and 92.91 px, respectively.

The comparison of the RMSE values illustrates that the positional accuracy of the optimized input is at least seven times higher than the initial input. The mean RMSE of these three photographs (5.30 px) corresponds to 0.79 m for the mean distance of 1044.46 m between the camera position and the GCPs and is thus smaller than the spatial resolution of the DEM (1 m).

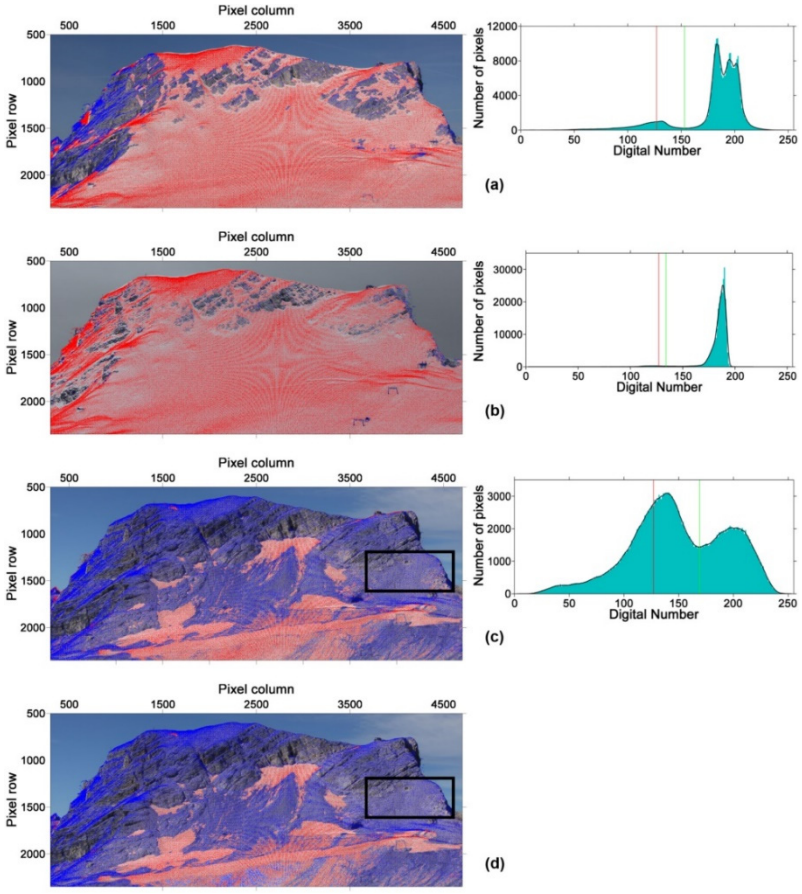

Figure 2.1-9: The superimposition of the DEM pixels (red dots=snow, blue dots=no snow) over the corresponding and enlarged photograph are shown on the left for the automatically classified images under clear sky conditions in spring on 11 May 2011 at 08:15CEST (a), under cloudy conditions in winter on 17 February 2012 at 15:07CET (b), and under clear sky conditions in summer on 16 August 2011, 11:05CEST (c), as well as for the manually reprocessed classification of the August image (d). On the right, the corresponding snow thresholds (green lines) are illustrated: 153 (a), 134 (b) and 169 (c). The manual snow classification threshold is 169 for all three RGB bands and 10 for the maximum-minimum test (d). The black box in (c) and (d) depicts a small test area in the investigation area at the Schneefernerkopf where visually no snow could be detected although several pixels are classified as snow.

The visual investigation of the automatically classified photographs showed qualitatively a good agreement between automatically classified and visually observed snow-covered areas (fig. 2.1-9a to c,

enlarged views of the investigation area). The high quality of the classification applies to both clear sky conditions in the May image (fig. 2.1-9a) and cloudy conditions in the February image (fig. 2.1-9b). In the August photograph (fig. 2.1-9c), limitations in the classification with respect to light-coloured bare rock could be observed. A small test area (11701 m^2, black box in fig. 2.1-9c) was selected within the investigation area where visually no snow could be detected. However, the automatic classification routine mistakenly classifies 477 m^2 of limestone as snow, which corresponded to a relative error of 4.1 %.

The August photograph was also processed using the manual classification routine (fig. 2.1-9d). The thresholds of the RGB bands were identical to the automatically derived classification threshold (169) in fig. 2.1-9c. The maximum allowed spread between the three RGB values of one pixel was 10. Qualitatively, the visual investigation of the overlay of the photograph and the classification shows a good match for the investigation area. We investigated again the same small test area (black box in fig. 2.1-9d). The misclassification is reduced to 100 m^2 (0.9 %) in comparison to the automatic classification as the light-coloured bare rock reflects the blue band significantly weaker than the red and green bands.

The resulting snow cover maps of the three photographs are depicted in the figs. 2.1-10a to c using the classification of figs. 2.1-9a, b and d, respectively. We compared the derived snow cover extent in fig. 2.1-10a, to the DEM, respective to the slope in more detail. More than 90 % of the areas free of snow on this date are located in steep terrain with slope angles above 35° (without figure). With the last snowfall being on 3 May 2011, this is reasonable due to gravitational snow redistribution (Bernhardt and Schulz, 2010). The snow cover extents in the investigation area (black dotted line) are in accordance with the time of the year, and amount to 94000 m^2 on 11 May 2011 (fig. 2.1-10a), 122000 m^2 on 17 February 2012 (fig. 2.1-10b) and 13000 m^2 on 16 August 2011 (fig. 2.1-10c).

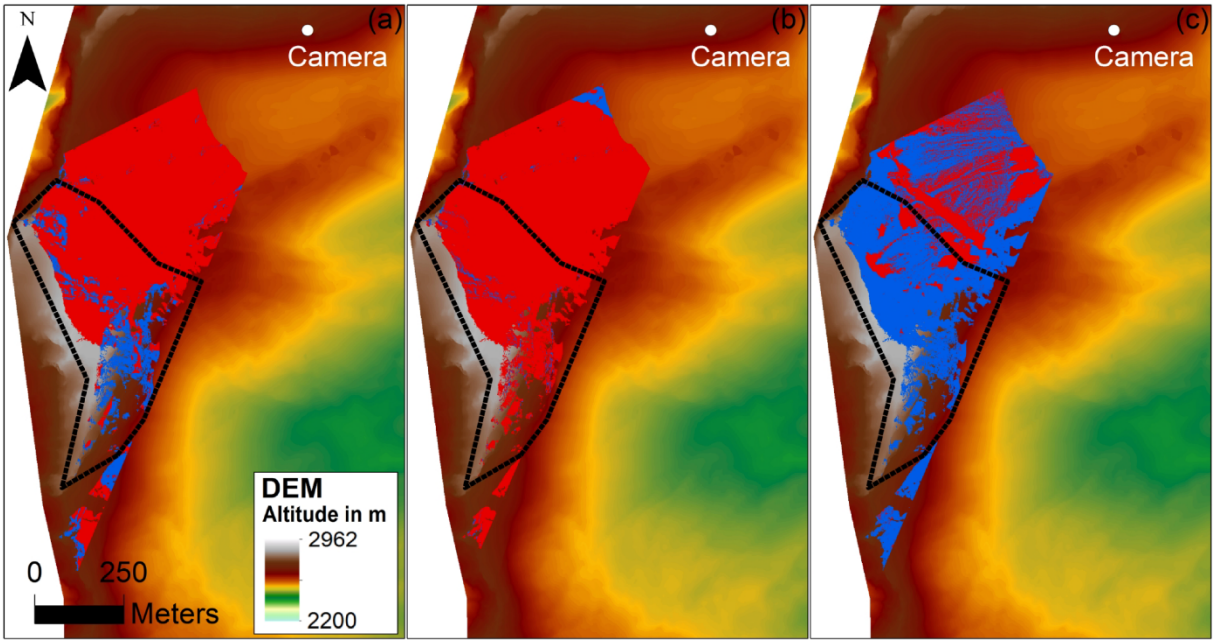

Figure 2.1-10: The maps depict the resulting snow cover extent of the figs. 2.1-9a (a), b (b), and d (c). The black dashed line outlines the investigation area at the Schneefernerkopf. We want to note here that the small test area (black box in fig. 2.1-9d) is not shown in (c).

The present results reveal that PRACTISE, with its different features and its flexibility, is an efficient software tool to produce temporal and spatial high-resolution snow cover maps. All methods used are well-established and the optional routines can be selected by the user depending on the available data and the task. We have shown here that the DDS optimization as well as the classification routines produce high-quality results for the three investigated photographs. The accuracy assessments of all three images are better than the spatial resolution of the DEM. Thus, the DDS optimization of the interior and exterior orientation parameters makes the software very valuable for the analysis of photographs where the camera parameters are only imprecisely known, for example for extensive time series where camera movements are a problem. The combined use of DDS optimization and viewshed routine additionally hastens the georectification procedure in our study as with each new camera location, a new viewshed is needed. The automatic snow classification of Salvatori et al. (2011) works well in most cases without the need for calibration or the manual determination of thresholds for different weather situations and snow cover patterns. The manual classification routine provided in PRACTISE can be used as an alternative under unfavourable conditions. Although the automatic classification represents a promising approach, the presented classification results also confirm the well-known limitations in the

snow classification using the visible spectrum (0.4–0.7μm). Shadows are another possible source of uncertainty; however, they do not have a great effect on the snow cover mapping in our study as the recording time was able to be controlled and was adjusted to a minimum of shading (Dozier, 1989; Winther and Hall, 1999; Schmidt, 2007; Salvatori et al., 2011).

The fast and easy processing capabilities of PRACTISE might help to increase the efficiency of terrestrial photography either in validating spatially distributed snow-hydrological models (Lehning et al., 2006) or in statistically analyzing snow patterns influenced by the topography (Lehning et al., 2011). Future studies using PRACTISE will test the comparability of SLR images to other methods of snow cover detection and include long-term studies. A further topic of research will be the development of an automatic classification algorithm that is less prone to misclassifications of snow in digital camera images caused by clouds, shadows or light-coloured bare rock. The versatility and the opportunity to comfortably georeference especially large time series of photographs in PRACTISE makes the software also attractive for other research disciplines. In particular, the aforementioned example of phenological greenness indexes, as well as the observation of land surface temperatures using thermal infrared cameras might be interesting fields of application.

Supplement

Supplementary material related to this article is available online at: http://www.geosci-model-dev.net/6/837/2013/gmd-6-837-2013-supplement.zip.

Acknowledgement. The authors want to especially thank Thomas Werz who installed and maintained the digital camera at the Environmental Research Station Schneefernerhaus (UFS) during his master thesis and David Morche for providing the DEM. We appreciate the computational support of Benjamin Müller, as well as the helpful comments and suggestions of the referees S. Pohl, M. Spencer and an anonymous referee. The work was supported by the UFS, the doctoral scholarship program “Deutsche Bundesstiftung Umwelt” (DBU) and the Helmholtz Research School “Mechanisms and Interactions of Climate Change in Mountain Regions” (MICMoR).

Edited by: I. Rutt

References

Ahrends, H. E., Brügger, R., Stöckli, R., Schenk, J., Michna, P., Jeanneret, F., Wanner, H., and Eugster, W.: Quantitative phenological observations of a mixed beech forest in northern Switzerland with digital photography, J. Geophys. Res., 113, G04004, doi:10.1029/2007jg000650, 2008.

Aschenwald, J., Leichter, K., Tasser, E., and Tappeiner, U.: Spatio-temporal landscape analysis in mountainous terrain by means of small format photography: a methodological approach, IEEE T. Geosci. Remote, 39, 885–893, doi:10.1109/36.917917, 2001.

Bernhardt, M. and Schulz, K.: SnowSlide: a simple routine for calculating gravitational snow transport, Geophys. Res. Lett., 37, L11502, doi:10.1029/2010gl043086, 2010.

Clark, P. E. and Hardegree, S. P.: Quantifying vegetation change by point sampling landscape photography time series, Rangeland Ecol. Manage., 58, 588–597, doi:10.2111/04-111R2.1, 2005.

Corripio, J. G.: Snow surface albedo estimation using terrestrial photography, Int. J. Remote Sens., 25, 5705–5729, doi:10.1080/01431160410001709002, 2004.

Corripio, J. G., Durand, Y., Guyomarc'h, G., Mérindol, L., Lecorps, D., and Pugliése, P.: Land-based remote sensing of snow for the validation of a snow transport model, Cold Reg. Sci. Technol., 39, 93–104, doi:10.1016/j.coldregions.2004.03.007, 2004.

Crimmins, M. and Crimmins, T.: Monitoring plant phenology using digital repeat photography, Environ. Manage., 41, 949–958, doi:10.1007/s00267-008-9086-6, 2008.

Dozier, J.: Spectral signature of alpine snow cover from the Landsat Thematic Mapper, Remote Sens. Environ., 28, 9–22, doi:10.1016/0034-4257(89)90101-6, 1989.

Dumont, M., Arnaud, Y., Six, D., and Corripio, J. G.: Retrieval of glacier surface albedo using terrestrial photography, Houille Blanche, 2, 102–108, doi:10.1051/Lhb/2009021, 2009.

Hinkler, J., Pedersen, S. B., Rasch, M., and Hansen, B. U.: Automatic snow cover monitoring at high temporal and spatial resolution, using images taken by a standard digital camera, Int. J. Remote Sens., 23, 4669–4682, doi:10.1080/01431160110113881, 2002.

Klemes, V.: The modelling of mountain hydrology: the ultimate challenge, IAHS Publ., 190, 29–43, 1990.

Lehning, M., Völksch, I., Gustafsson, D., Nguyen, T. A., Stähli, M., and Zappa, M.: ALPINE3D: a detailed model of mountain surface processes and its application to snow hydrology, Hydrol. Process., 20, 2111–2128, doi:10.1002/Hyp.6204, 2006.

Lehning, M., Grünewald, T., and Schirmer, M.: Mountain snow distribution governed by an altitudinal gradient and terrain roughness, Geophys. Res. Lett., 38, L19504, doi:10.1029/2011gl048927, 2011.

Major, J. J., Dzurisin, D., Schilling, S. P., and Poland, M. P.: Monitoring lava-dome growth during the 2004–2008 Mount St. Helens, Washington, eruption using oblique terrestrial photography, Earth Planet. Sci. Lett., 286, 243–254, doi:10.1016/j.epsl.2009.06.034, 2009.

Michel, P., Mathieu, R., and Mark, A. F.: Spatial analysis of oblique photo-point images for quantifying spatio-temporal changes in plant communities, Appl. Veget. Sci., 13, 173–182, doi:10.1111/j.1654-109X.2009.01059.x, 2010.

Migliavacca, M., Galvagno, M., Cremonese, E., Rossini, M., Meroni, M., Sonnentag, O., Cogliati, S., Manca, G., Diotri, F., Busetto, L., Cescatti, A., Colombo, R., Fava, F., di Celia, U. M., Pari, E., Siniscalco, C., and Richardson, A. D.: Using digital repeat photography and eddy covariance data to model grassland phenology and photosynthetic CO_2 uptake, Agr. Forest Meteorol., 151, 1325–1337, doi:10.1016/j.agrformet.2011.05.012, 2011.

Parajka, J., Haas, P., Kirnbauer, R., Jansa, J., and Blöschl, G.: Potential of time-lapse photography of snow for hydrological purposes at the small catchment scale, Hydrol. Process., 26, 3327–3337, doi:10.1002/Hyp.8389, 2012.

Richardson, A. D., Jenkins, J. P., Braswell, B. H., Hollinger, D. Y., Ollinger, S. V., and Smith, M. L.: Use of digital webcam images to track spring green-up in a deciduous broadleaf forest, Oecologia, 152, 323–334, doi:10.1007/s00442-006-0657-z, 2007.

Rivera, A., Corripio, J. G., Brock, B., Clavero, J., and Wendt, J.: Monitoring ice-capped active Volcan Villarrica, southern Chile, using terrestrial photography combined with automatic weather stations and global positioning systems, J. Glaciol., 54, 920–930, doi:10.3189/002214308787780076, 2008.

Roush, W., Munroe, J. S., and Fagre, D. B.: Development of a spatial analysis method using ground-based repeat photography to detect changes in the alpine treeline ecotone, Glacier National Park, Montana, USA, Arctic Antarctic Alpine Res., 39, 297–308, doi:10.1657/1523-0430(2007)39[297:doasam]2.0.co;2, 2007.

Salvatori, R., Plini, P., Giusto, M., Valt, M., Salzano, R., Montagnoli, M., Cagnati, A., Crepaz, G., and Sigismondi, D.: Snow cover monitoring with images from digital camera systems, Ital. J. Remote Sens., 43, 137–145, doi:10.5721/ItJRS201143211, 2011.

Schmidt, S.: Die reliefabhängige Schneedeckenverteilung im Hochgebirge. Ein multiskaliger Methodenverbund am Beispiel des Lötschentals (Schweiz), Ph.D. thesis, Faculty of math and natural sciences, University of Bonn, Bonn, Germany, 2007.

Tolson, B. A. and Shoemaker, C. A.: Dynamically dimensioned search algorithm for computationally efficient watershed model calibration, Water Resour. Res., 43, W01413, doi:10.1029/2005wr004723, 2007.

Wang, J., Robinson, G. J., and White, K.: Generating viewsheds without using sightlines, Photogramm. Eng. Remote S., 66, 87– 90, 2000.

Watt, A. and Watt, M.: Advanced Animation and Rendering Techniques: Theory and Practice, ACM Press, New York, 1992.

Winther, J. G. and Hall, D. K.: Satellite-derived snow coverage related to hydropower production in Norway: present and future, Int. J. Remote Sens., 20, 2991–3008, doi:10.1080/014311699211570, 1999.

Zier, J. L. and Baker, W. L.: A century of vegetation change in the San Juan Mountains, Colorado: an analysis using repeat photography, Forest Ecol. Manage., 228, 251–262, doi:10.1016/j.foreco.2006.02.049, 2006.

2.2 Publication II

The following text is an edited version of a submitted Computer & Geosciences article:

Matlab© toolbox PRACTISEgeo v.1.0: Extending the focus of PRACTISE (Photo Rectification And ClassificaTIon Software) from the cryosphere to other geoscientific photo mapping applications

S. Härer[1], M. Bernhardt[1], and K. Schulz[1]

[1] Institute of Water Management, Hydrology and Hydraulic Engineering (IWHW), University of Natural Resources and Life Sciences (BOKU), Vienna, Austria

Correspondence to: S. Härer (stefan.haerer@boku.ac.at)

Abstract

PRACTISEgeo is a Matlab toolbox for the software PRACTISE (Photo Rectification And ClassificaTIon SoftwarE) which has been initially developed for the generation of alpine snow cover maps by using ground-based photography. PRACTISEgeo makes PRACTISE functionalities available for other geoscientific research topics with a need for open-source photo rectification software. The toolbox includes pre- and post-processing functions for PRACTISE. PRACTISEgeo delivers a graphical user interface for the photo rectification process to make a simple and accurate ground control point (GCP) delineation possible. Moreover, it allows for the generation of single-band (e.g. thermal) as well as three-band (e.g. RGB) orthophotos by using the existent PRACTISE infrastructure. Hence, with these two major features the presented toolbox significantly increases the capabilities of PRACTISE and in particular, the detection of GCPs is suited to reduce the user workload. Another advantage is that PRACTISEgeo makes PRACTISE accessible to end users inexperienced in photo rectification.

1 Introduction

Automatic ground-based camera networks were heavily extended during the last years. They exist in many environments and the reasons for installation are usually non-scientific and range from e.g. traffic and security purposes in urban areas to touristic advertisements in natural environments. Nevertheless, these cameras can be seen as an important source of information in research often recording some content of scientific relevance (Härer et al., 2016; Morris et al., 2013; Timothy and Groves, 2001). To make use of this content, a localization of the photographs is often needed. In some cases, a simple

localization might be not sufficient and an orthorectification of the 2-D photography is needed. Snow cover mapping can serve as an example here: the 2-D photographs have to be converted into a spatial information readable by geoinformation software (GIS) or other interpretation tools (Härer et al., 2013).

PRACTISE (Photo Rectification And ClassificaTIon SoftwarE) was developed for exactly this purpose, namely the conversion from 2-D RGB photographs into orthorectified snow cover maps with a standard format of geoprocessing software. PRACTISE is executable in Matlab and GNU Octave environments and has proven its applicability at various sites in the European Alps (Härer et al., 2013; Härer et al., 2016). However, as a free and open-source georectification software is also needed in other geoscientific research areas, a long-term objective was to open PRACTISE to any geoscientific mapping application that needs to rectify photographs. A second objective thereby was to make the handling of PRACTISE easier.

The development of PRACTISEgeo v.1.0 can be seen in the light of these requirements. It is a Matlab toolbox for PRACTISE and provides two central functionalities. First, it serves as an interface to generate single-band (1B, e.g. thermal or grayscale) or three-band (3B, e.g. RGB or 3B false-color composite) orthophotos. And secondly, it has an innovative user-interactive approach to facilitate and significantly fasten the accurate rectification of the photograph in the 3-D world. Some secondary features of PRACTISEgeo are related to the user-friendliness. They include routines which deliver detailed information on the photo rectification accuracy or allow a fast automatic update of the input file of PRACTISE. All features are written as Matlab functions and either need to be applied before or after the execution of PRACTISE. The functions are described in subsect. 2, while the source code with a manual is available in a GitHub repository (see subsect. 3).

2 The Matlab toolbox PRACTISEgeo v.1.0

The functionality and compatibility of PRACTISEgeo v.1.0 was developed and tested with PRACTISE v.2.1 (Härer et al., 2016) at the alpine headwater catchment Zugspitzplatt, Germany (Wetzel, 2004; Weber et al., 2016) and the photographs are taken from the environmental research station Schneefernhaus (UFS, Bernhardt et al., 2014). More information on the camera setup, the test site and the internal program structure of PRACTISE is given in Härer et al. (2013) and Härer et al. (2016).

Figure 2.2-1 depicts the general workflow before and after the Matlab toolbox PRACTISEgeo v.1.0 was introduced. It thereby gives an overview on inputs and outputs, scripts and functions, and interfaces of PRACTISE and PRACTISEgeo.

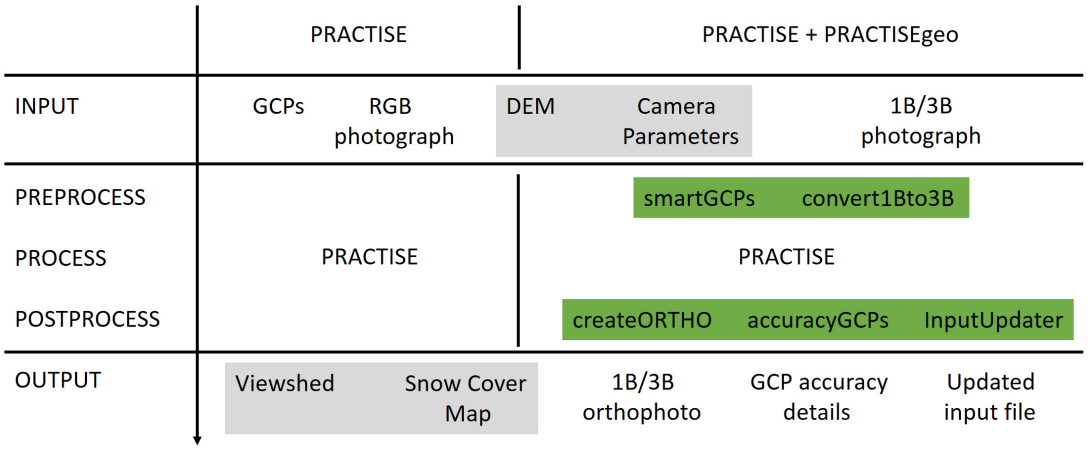

Figure 2.2-1. The old workflow from input data over processing steps to the output using solely PRACTISE is depicted on the left and for the new workflow combining PRACTISE and PRACTISEgeo on the right. With respect to the input and output, the grey boxes represent data needed for or generated with both workflows and additionally separate the old (left) from the new (right) workflow. The new optional processing functions introduced with PRACTISEgeo are highlighted in green.

The orthorectification of 1B and 3B images is performed using the functions *convert1Bto3B* and *createORTHO* in PRACTISEgeo. The function *convert1Bto3B* first converts single-band products (1B) e.g. thermal or greyscale photographs to a 3B synthetic false-color composite as PRACTISE needs a 3B photography as input. In a next step and in succession of the PRACTISE run, the function *createORTHO* generates a 1B or 3B orthophoto with a color code identical to the original image in a format readable in standard geoprocessing software. PRACTISE provides a batch mode which allows for the sequential automatic processing of several photographs within a single program evaluation. This is especially useful in course of time series analysis and is also available in the functions *convert1Bto3B* and *createORTHO*. As a processing example for a single photograph, fig. 2.2-2a to c show a 1B greyscale photograph of the Schneefernerkopf at the Zugspitzplatt, Germany, the converted 3B false-color composite and the resulting 1B orthophoto.

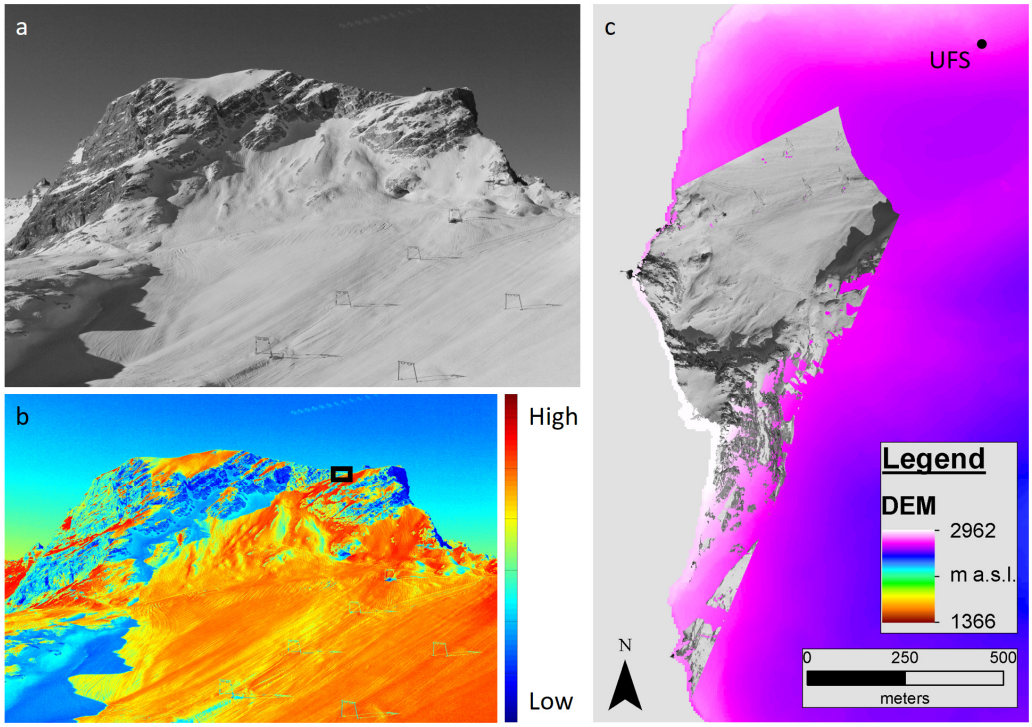

Figure 2.2-2: Orthophoto generation example from a greyscale photograph of Schneefernerkopf at the Zugspitzplatt, Germany (a) using PRACTISEgeo: The function *convert1Bto3B* converts the single-band (1B) photograph to a three-band (3B) false-color composite (b) as PRACTISE needs a 3B photograph as input. After the PRACTISE execution, the function *createORTHO* then generates the 1B orthophoto (c) which is superimposed here on the DEM and also shows the camera position located at the UFS. The black box in (b) depicts the extent shown enlarged in fig. 2.2-3.

In general, it is beneficial for orthophoto generation to use a high-resolution digital elevation model (DEM) as this determines the horizontal spatial resolution of the resulting orthophoto. This is decisive for the orthophoto quality as most of the today's camera systems have a very high resolution and do therefore not act as the limiting factor. Figure 2.2-3, showing an enlarged view of the photograph from fig. 2.2-2b, clarifies the effect of the horizontal DEM resolution for the used example by superimposing the projected DEM pixels. The digital number of the photograph at the projected DEM pixels are thereby directly used for the orthophoto generation.

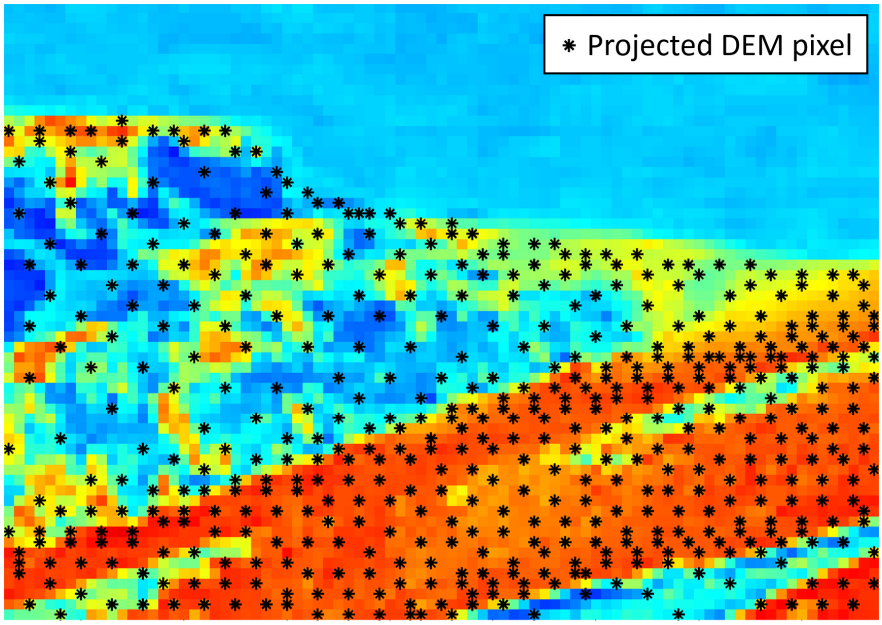

Figure 2.2-3: DEM pixels with a horizontal spatial resolution of 1m (black stars) projected to the 2-D photo plane are superimposed on the enlarged view of fig. 2.2-2b (black box). If the DEM resolution is 5 m, only about 20 projected DEM pixels would be present in this photo extent. A lower resolution DEM thus results in a lower quality orthophoto, especially in the steep (blue and green) areas.

The function *SmartGCPs* in PRACTISEgeo delivers a graphical user interface and applies an innovative approach utilizing the terrain silhouette in the photograph for an accurate photo rectification. This method significantly reduces the time exposure as the formerly used GCP delineation was performed manually and was based on numerous additional information like DEM, orthophotos, topographic maps or in situ GPS measurements. The new strategy incorporated in *SmartGCPs* allows for a usage of the software package to users unexperienced in photo rectification or users which do not have access to the needed information for the manual delineation of GCPs. The key skill of *SmartGCPs* is that it uses the terrain silhouette, specified by the projected DEM applying a user-defined first guess for camera location and orientation. This silhouette is superimposed on the photograph and thus the difference between photograph and real world (DEM) terrain silhouette directly displays the current rectification accuracy (fig. 2.2-4). The user can then interactively select or, if necessary, delete GCPs via mouse clicks on the photograph and hence iteratively optimize camera location and orientation. Finally, the input file for the PRACTISE run is automatically updated with the new camera parameters using the function *InputUpdater*.

InputUpdater is hence called by the *SmartGCPs* function but moreover, this function is also directly usable if parameters in the input file of PRACTISE need to be updated in an efficient way from parameters saved in an earlier PRACTISE run, or given as an input argument of the function.

Another function enhancing the general applicability of PRACTISE is *GCPaccuracy* that provides detailed information on the photo rectification accuracy. Resulting outputs are the rectification accuracy of each GCP in units of the camera (in pixels) and the real world coordinate system (meters).

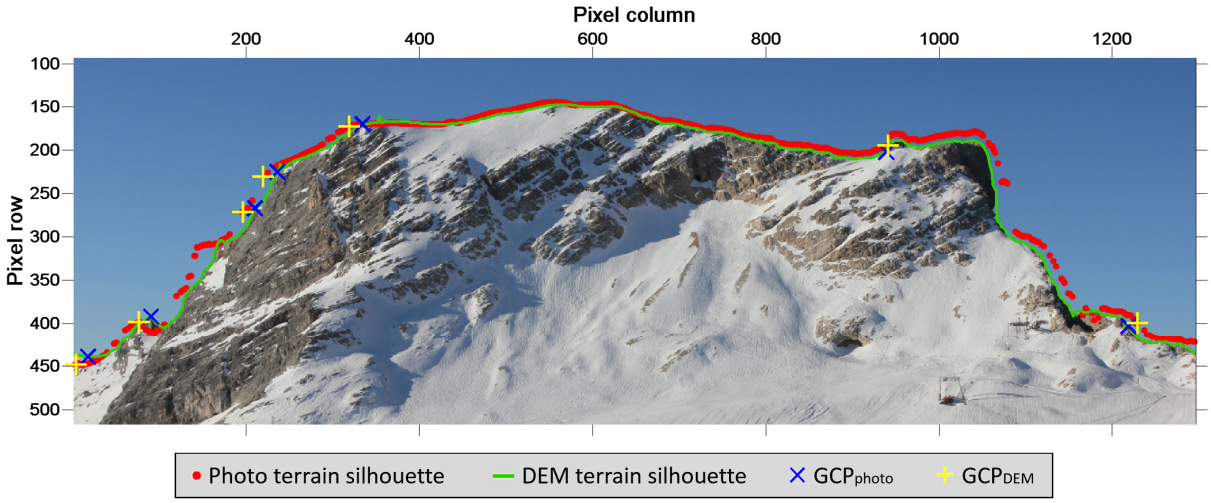

Figure 2.2-4: The optional terrain silhouette of the photograph (enlarged RGB version of fig. 2.2-2a) is depicted in green while the terrain silhouette of the DEM projected to the photo plane is shown in red in the graphical user interface (GUI) of the *SmartGCPs* function. The user can then interactively select and delete GCPs by mouse, these are displayed as blue 'X' for the photograph silhouette (GCP_{photo}) and as yellow crosses for the DEM silhouette (GCP_{DEM}). The camera location and orientation are then iteratively optimized using these GCPs.

3 Code availability

The software PRACTISE v.2.1 and the extension toolbox PRACTISEgeo v.1.0 are both distributed under the Creative Commons license (CC-BY-NC-SA 4.0) and freely available with source code, example data and manual in GitHub Repositories. The scripts and functions are executable using Matlab (version 2005 and later) as well as the open-source Matlab alternative, GNU Octave 4.0 (64-bit-enabled) and higher.

PRACTISE v.2.1: https://github.com/shaerer/PRACTISE/releases/tag/v2.1

PRACTISEgeo v.1.0: The link to the public GitHub repository will be added here after acceptance.

Acknowledgments. The authors want to thank the Austrian Science Fund (I 2142-N29), the doctoral scholarship program of the German Federal Environmental Foundation (DBU), the Helmholtz Research School Mechanisms and Interactions of Climate Change in Mountain Regions (MICMoR) and the Environmental Research Station Schneefernerhaus (UFS) in course of the Virtual Alpine Observatory (VAO). All of which supported the development of the software packages PRACTISE and PRACTISEgeo. Namely, we want to thank Markus Neumann, Dr. Till Rehm and Hannes Hiergeist (at the UFS), as well as Michael Weber (LMU Munich), Thomas Werz (formerly LMU Munich) and David Morche (Martin Luther University Halle–Wittenberg) for their help and support.

References

Bernhardt, M., Härer, S., Jacobeit, J., Wetzel, K. F., and Schulz, K.: The virtual alpine observatory – research focus Alpine hydrology, Hydrol. Wasserbewirts., 58, 241–243, 2014.

Härer, S., Bernhardt, M., Corripio, J. G., and Schulz, K.: PRACTISE – Photo Rectification And ClassificaTIon SoftwarE (v.1.0), Geosci. Model Dev., 6, 837–848, doi:10.5194/gmd-6-837-2013, 2013.

Härer, S., Bernhardt, M., and Schulz, K.: PRACTISE – Photo Rectification And ClassificaTIon SoftwarE (v.2.1), Geosci. Model Dev., 9, 307–321, doi:10.5194/gmd-9-307-2016, 2016.

Morris, D. E., Boyd, D. S., Crowe, J. A., Johnson, C. S., and Smith, K. L.: Exploring the Potential for Automatic Extraction of Vegetation Phenological Metrics from Traffic Webcams, Remote Sens., 5, 2200–2218, doi:10.3390/rs5052200, 2013.

Timothy, D. J., and Groves, D. L.: Research note: Webcam images as potential data sources for tourism research, Tour. Geogr., 3, 394–404, doi:10.1080/146166800110070487, 2001.

Weber, M., Bernhardt, M., Pomeroy, J. W., Fang, X., Härer, S., and Schulz, K.: Description of current and future snow processes in a small basin in the Bavarian Alps, Environ. Earth Sci., 75(17), 1223, doi:10.1007/s12665-016-6027-1, 2016.

Wetzel, K. F.: On the hydrology of the Partnach area in the Wetterstein mountains (Bavarian Alps), Erdkunde, 58(2), 172–186, doi:10.3112/erdkunde.2004.02.05, 2004.

2.3 Publication III

The following text is an edited version of the 2016 Geoscientific Model Development (GMD) article:

PRACTISE – Photo Rectification And ClassificaTIon SoftwarE (v.2.1)

S. Härer[1], M. Bernhardt[1] and K. Schulz[1]

[1] Institute of Water Management, Hydrology and Hydraulic Engineering (IWHW),
University of Natural Resources and Life Sciences (BOKU), Vienna, Austria

Correspondence to: S. Härer (stefan.haerer@boku.ac.at)

Abstract.

Terrestrial photography combined with the recently presented Photo Rectification And ClassificaTIon SoftwarE (PRACTISE v.1.0) has proven to be a valuable source to derive snow cover maps in a high temporal and spatial resolution. The areal coverage of the used digital photographs is however strongly limited. Satellite images, on the other hand, can cover larger areas but do show uncertainties with respect to the accurate detection of the snow-covered area. This is especially the fact if user-defined thresholds are needed, e.g. in case of the frequently used normalized-difference snow index (NDSI). The definition of this value is often not adequately defined by either a general value from literature or the impression of the user, but not by reproducible independent information. PRACTISE v.2.1 addresses this important aspect and shows additional improvements. The Matlab-based software is now able to automatically process and detect snow cover in satellite images. A simultaneously captured camera-derived snow cover map is in this case utilized as in situ information for calibrating the NDSI threshold value. Moreover, an additional automatic snow cover classification, specifically developed to classify shadow-affected photographs, was included. The improved software was tested for photographs and Landsat 7 Enhanced Thematic Mapper (ETM+) as well as Landsat 8 Operational Land Imager (OLI) scenes in the Zugspitze massif (Germany). The results show that using terrestrial photography in combination with satellite imagery can lead to an objective, reproducible, and user-independent derivation of the NDSI threshold and the resulting snow cover map. The presented method is not limited to the sensor system or the threshold used in here but offers manifold application options for other scientific branches.

1 Introduction

Snow cover plays an important role in the Earth's climate system as direct feedback mechanisms between surface temperature, surface albedo, and snow cover exist (IPCC, 2013). These reinforcing feedback processes have significantly contributed to the observed decrease in spring snow cover in the Northern Hemisphere in the last decades (Groisman et al., 1994; IPCC, 2013). Despite this general trend in the Northern Hemisphere, the observed seasonal and altitudinal variations in snow cover changes are large for different regions (Brown and Mote, 2009). Regional studies are thus crucial to provide a more complete picture. This is of special importance for high elevation areas where large amounts of water are temporally stored as snow and which therefore supply the lowlands with fresh water during the snowmelt in spring and summer (Viviroli et al., 2007, 2011).

However, station data of snow cover in alpine regions are rare except for a few well-equipped sites (Scherrer et al., 2004; Marty, 2008; Viviroli et al., 2011; Pomeroy et al., 2015). Manual in situ measurements are often prevented for reasons of remoteness and safety by the harsh environmental conditions (Klemes, 1990). Satellite remote sensing techniques are a big step forward in these data-scarce areas but it is still a challenge to achieve snow cover products with high spatial and temporal resolutions as well as a high accuracy (Klemes, 1990; Viviroli et al., 2011). The complementary use of ground and spaceborne measurements for observing mountainous snow cover as highlighted by Vivirioli et al. (2011) is a promising approach and the main motivation behind this paper.

Terrestrial photography is thereby utilized as *ground truth* data. This technique has been successfully applied in many applications in the context of glaciology and snow hydrology (Corripio, 2004; Rivera et al., 2008; Dumont et al., 2009; Garvelmann et al., 2013; Messerli and Grinsted, 2015; cf. Parajka et al., 2012 for an overview). The advantages of terrestrial photography are that this technique has a high accuracy, is non-invasive, and provides spatially distributed snow cover data in a high temporal and spatial resolution (Aschenwald et al., 2001; Hinkler et al., 2002; Corripio et al., 2004; Schmidt et al., 2009; Parajka et al., 2012; Härer et al., 2013). The decreasing costs of digital cameras and camera lenses with no or minimal distortion, as well as the potential use of terrestrial photography in remote and hostile

environments due to technical advancements in off-grid power supply and data transfer also need to be mentioned here.

The alpine snow cover patterns derived from terrestrial photography can then be used to evaluate spatially distributed (snow-)hydrological models like Alpine3D, SnowModel, and others (Lehning et al., 2006; Liston and Elder, 2006; Bernhardt et al., 2012). The high spatial resolution of the photograph snow cover maps is very valuable, as snow cover strongly varies over time and space and an accurate description in models is difficult (Blöschl et al., 1991; Winstral and Marks, 2002; Bernhardt and Schulz, 2010). The high temporal resolution of the terrestrial camera systems, for example on an hourly basis, further enhances the probability of at least one suitable photograph per day, despite the frequently occurring cloud and precipitation events at high altitudes (Härer et al., 2013).

To map the spatial snow cover distributions, the recorded 2-D photographs have to be classified and georectified. Corripio (2004) and Corripio et al. (2004) presented a software tool that eased the georectification process, utilizing the animation and rendering technique by Watt and Watt (1992). This also formed the basis for the Photo Rectification And ClassificaTIon SoftwarE (PRACTISE v.1.0; Härer et al., 2013). Though, the formulations for the calculation of the 3-D rotation and projection are slightly different to Corripio (2004) and Corripio et al. (2004). PRACTISE v.1.0 further simplifies and fastens the spatially distributed monitoring of snow cover patterns in mountainous terrain as it includes in addition to the georectification module routines for the identification of camera location and orientation, the viewshed computation and the snow classification of photographs. A batch mode also allows the processing of several photographs and thus the generation of multiple snow cover maps in a single program evaluation.

The trade-off for the high spatial resolution snow cover maps from terrestrial photography is that these maps are restricted to a comparatively small region. To monitor a complete catchment with an extent of several square kilometers and more, satellite imagery is more suitable. These data have a lower spatial and temporal resolution but it offers the advantage of long consistent time series and the coverage of large areas. The normalized-difference snow index (NDSI) formulated by Dozier in 1989 for Landsat data is thereby still a standard method to derive snow cover maps (cf. SNOMAP algorithm of the

MODIS snow cover product; Hall et al., 2001; Hall and Riggs, 2007). Other promising methods like traditional supervised multispectral classifications, artificial neural networks or spectral-mixture analyses are computationally highly intensive, need lots of additional input data or are dependent on the interpreter's knowledge (Hall et al., 2001). These techniques are thus difficult to automate.

The NDSI represents the spaceborne component in the synthesis of ground and satellite measurements in this study. The index relies on a band rationing technique with a simple but effective principle that snow is highly reflective in the visible bands (GREEN, ~0.55 µm) while having a very low reflectance in the mid-infrared bands (MIR; ~1.6 µm; Dozier, 1989). In this approach, it is assumed that snow is present within a satellite pixel if the NDSI is greater than 0.4,

$$NDSI = \frac{GREEN - MIR}{GREEN + MIR} > 0.4, \quad (2.3\text{-}1)$$

and the near-infrared (NIR; ~0.85 µm) reflectance value is above 0.11,

$NIR > 0.11$ (Dozier, 1989; Hall et al., 1995). (2.3-2)

The NIR condition ensures that water surfaces, which can also have high NDSI values, are not misclassified as snow.

The NDSI threshold value of 0.4 is the standard literature value (Nolin, 2010; Dietz et al., 2012) even though Hall et al. (1995) already mention that acceptable snow cover maps were found for NDSI thresholds between 0.25 and 0.45 in a study investigating six scenes in the United States and Iceland. This threshold range corresponded to changes in snow cover extent of more than 10 % in the studied scenes. In particular for local and regional applications it is thus crucial to set the NDSI threshold accurately but in a user-friendly and standardized manner. The manual adjustment of the threshold is no option in most cases as it is not reproducible and offers the danger of adapting the resulting snow cover distribution to support a given hypothesis.

This paper presents a new method to monitor alpine snow cover patterns with satellite data by making use of terrestrial camera infrastructure, including webcams. The NDSI threshold value for snow is thereby calibrated to achieve an optimal agreement in the overlapping area of the photograph and

satellite snow cover maps. Hence, an optimal NDSI based satellite snow cover map for the specific region and time is produced, for example for an alpine catchment with an extent of several square kilometers. The cameras needed for this method are often already available or can be easily installed at many sites. We focus on Landsat data in here, as the pixel dimensions of 30 m are in comparison to MODIS pixel sizes of 500 m preferable for local and regional applications, particularly as the instantaneous field of view further increases for mountainous terrain with steep slopes.

The new approach to complimentary use ground and spaceborne measurements to derive snow cover maps is fully implemented in PRACTISE v.2.1. The fast and easy-to-use processing includes the NDSI calculation from Landsat raw data as well as the use of NDSI maps produced externally in geoinformation systems. Optionally, it also allows for including an existing cloud mask using for example the freely available Fmask software (Zhu et al., 2015). In addition, a newly developed snow classification algorithm for shadow-affected photographs is presented in PRACTISE v.2.1. Further improvements are bug fixes and revised code of already published modules as well as increased user-friendliness.

This paper is supplemented with an example data set, a manual and the associated Matlab code. The structure of the paper itself is as follows: at first, the test site and data are described. The newly developed modules and improvements in existing modules of the software are subsequently explained. Then, the resulting snow cover maps of exemplary photographs and Landsat satellite images are presented and discussed for the test area. Finally, a conclusion and an outlook are given.

2 Test site and data

PRACTISE (v.2.1) was developed and tested in the Zugspitze massif, Germany. The investigated Zugspitzplatt covers a surface area of 13.1 km^2. A common single-lens reflex camera (SLR; Canon EOS 550D, Canon EF 17-40 mm f/4I USM objective lens, 17.9 Mpx) directed towards the north-east facing slope of the Schneefernerkopf and a webcam (Mobotix M10 L43, 1.2 Mpx) observing the southeastern area of the Zugspitzplatt are used (Fig. 1). Both cameras take hourly photographs during daylight and are installed at the Environmental Research Station Schneefernerhaus (UFS; 2650 m a.s.l.). We refer the reader to Bernhardt et al. (2014) for more information on the research station.

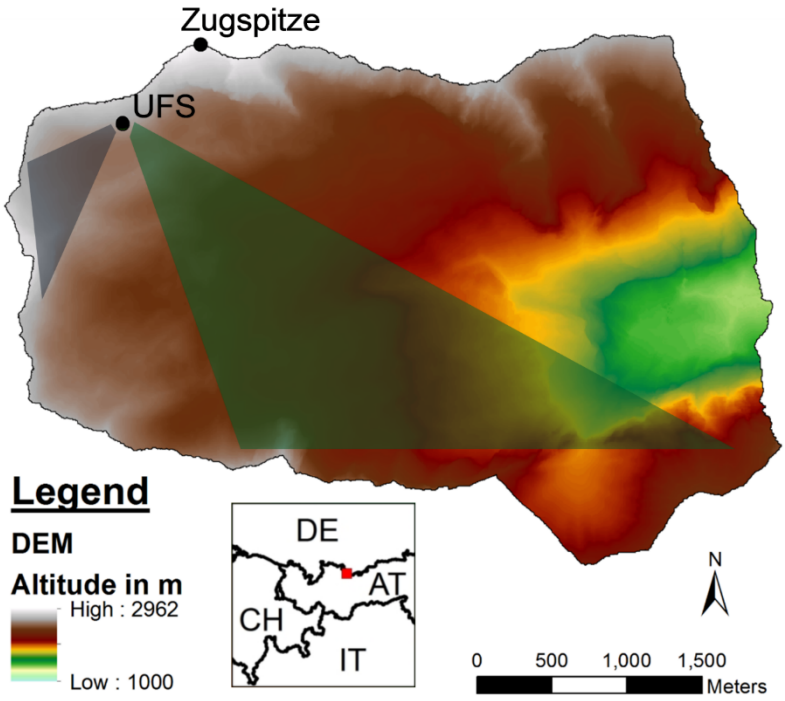

Figure 2.3-1: DEM of the Zugspitzplatt catchment at the border of Germany and Austria and the sketched fields of view of the cameras installed at the Environmental Research Station Schneefernerhaus (UFS; 2650 m): the single lens reflex camera (SLR) monitors Schneefernerkopf summit in the south-west of the UFS (blue) and the webcam is directed towards the southeastern Zugspitzplatt area (green).

2.1 General input data of PRACTISE v.2.1

PRACTISE v.2.1 requires a digital elevation model (DEM) and the exterior orientation parameters of the camera, i.e. the camera position $\boldsymbol{C}$, the camera target position $\boldsymbol{T}$ and the roll φ of the camera, as input. By definition, the camera target position is the location shown in the center of the photograph. The latitude and longitude positions of $\boldsymbol{C}$ and $\boldsymbol{T}$ are sufficient as input, as the altitude is taken from the corresponding DEM pixel during the computing process. If necessary, a camera offset o (installation height above the surface) is added to the altitude of $\boldsymbol{C}$, the combined altitude being referred to as $\boldsymbol{C}_o$. Similarly, a camera target offset t can be added to the elevation of $\boldsymbol{T}$ if $\boldsymbol{T}$ is not located inside the area covered by the DEM. The combined value is referred to as $\boldsymbol{T}_t$. In addition, interior orientation parameters of the camera are necessary, such as the focal length f, as well as the sensor dimensions: height h and width w (Härer et al., 2013). The vertical and horizontal dimensions of the photograph (N_v and N_h) are also needed for the georectification. These values are automatically derived by the software. We want to note here that lens distortions are not taken into account in PRACTISE as there are commercial and

open-source software packages (e.g. PTLens, http://epaperpress.com/ptlens/ and LensFun, http://lensfun.sourceforge.net/) for the pre-processing of distorted photographs available.

The above-mentioned inputs are obligatory in PRACTISE independent of the used modules. However, the camera parameters can also be estimated and automatically optimized if ground control points (GCPs) are available. The use of an externally calculated viewshed is optional if all exterior and interior camera parameters are known. Snow classification parameters are another required input in PRACTISE but only for the selected classification routine (cf. subsect. 3.1 and Härer et al., 2013). If the satellite image module is in use, radiometrically and geometrically corrected data of Landsat 5 Thematic Mapper (TM), Landsat 7 Enhanced Thematic Mapper Plus (ETM+), or Landsat 8 Operational Land Imager (OLI) can be processed. Instead of Landsat Level 1 data, the use of externally generated satellite NDSI maps is also possible. The spatial processing extent is user-dependent as well as if an externally produced mask for clouds, (cloud) shadows, and water is used or not. Another optional input is a Landsat Look image for visualization.

2.2 Study-specific input data of PRACTISE v.2.1

The functionality of the new modules of PRACTISE v.2.1 will be demonstrated on the basis of photographs and Landsat satellite images of 17 November 2011, 1 July 2013 and 7 April 2014. The dates were chosen because they represent different snow and illumination conditions at Zugspitzplatt as well as different snow cover extents and cloud coverages (figs. 2.3-2a to f). The scenes are therefore suited to test the capabilities of PRACTISE with respect to changing surrounding conditions.

SLR photographs are available for all dates while webcam images are available for 2013 and 2014. Landsat 7 overflights have captured the test site in 2011 and 2013 (figs. 2.3-2a and c), Landsat 8 in 2014 (fig. 2.3-2e). Masks for clouds, shadows, and cloud shadows as well as water bodies were externally generated with the Fmask algorithm of Zhu et al. (2015). The masks are applied for the scenes on 17 November 2011 and on 1 July 2013 whereas the cloud cover is not visible in the Landsat Look image on 17 November 2011. We also want to note here that Landsat 7 imagery is affected by a failure of the Scan Line Corrector (SLC) from 31 May 2003 onwards. The SLC normally compensates for the forward

motion of the Landsat satellite. But, Zugspitzplatt area is located in the center of the scene and is therefore not affected by this error.

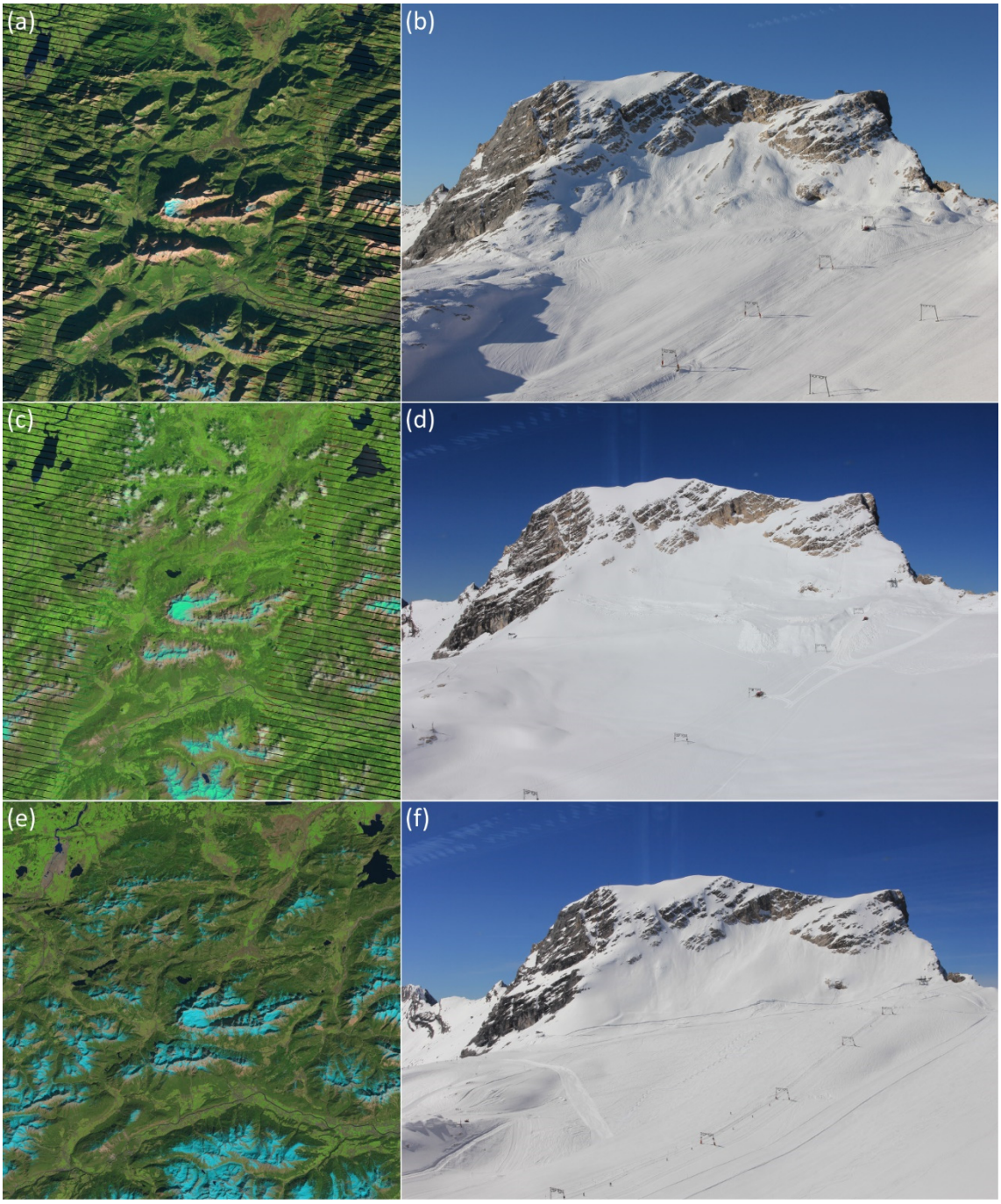

Figure 2.3-2: Enlarged view of the Landsat Look images of Zugspitzplatt (in the center) and SLR photographs of Schneefernerkopf for 17 November 2011 (a, b), 1 July 2013 (c, d), and 7 April 2014 (e, f): snow cover extents are generally depicted in cyan colours in the Landsat scenes. (a, b) show about one-month-old snow with strong shadowing effects and some partial cloud coverage (not visible in the Landsat Look image). (c) and (d) display fresh snow and have a significant but partial cloud coverage. (e) and (f) also show fresh snow but under clear conditions and with some weak shadowing effects.

The inputs given for the georectification of the SLR and webcam photographs are presented in table 2.3-1. Camera-dependent parameters were taken from the user manual of the camera systems. The focal lengths have been adjusted according to the used image. The location and target position of the camera as well as the GCP locations have been identified combining photographs, DEM data, topographical maps and official orthophotos with a sub-meter spatial resolution. Nevertheless, the camera location and target position could only be estimated. The camera parameters in table 2.3-1 except the camera sensor and photograph dimensions thus need to be optimized using GCPs. A separate estimation for each photograph in this study is further necessary as the locations and orientations of the cameras are changing in between the photographs due to either weather effects like wind, for maintenance reasons, or a new camera location at the UFS.

Table 2.3-1: Estimated parameters of the exterior and interior camera orientation of the SLR and webcam before the optimization: The parameter ranges in the optimization for the cameras and dates are given as differences to the estimated values. For the webcam photograph on 7 April 2014, the camera is directed towards an area outside of the DEM. Hence, the optimization of the camera target point offset *t* and an enlarged parameter range for the camera target point ($\boldsymbol{T}_t$) are necessary.

Parameter name	Input					Upper and lower boundaries		
	SLR camera			Webcam		SLR camera	Webcam	
	17/11/11	01/07/13	07/04/14	01/07/13	07/04/14	all dates	01/07/13	07/04/14
C_x	649 299.97			649 319.35		± 50	± 100	
C_y	5 253 358.26			5 253 356.25		± 50	± 100	
o	1.5			1.5		± 50	± 50	
T_x	648 740.85			650 801.1		± 250	± 250	± 500
T_y	5 252 771.33			5 251 927.6		± 250	± 250	± 500
t	0			0	500	0	0	± 500
φ [°]	0			0		± 3	± 3	
f	0.031	0.028		0.008		± 0.0025	± 0.0025	
h	0.0149			0.0048				
w	0.0223			0.0064				
N_v [px]	3456			960				
N_h [px]	5184			1280				

The DEM used for the SLR photographs has a spatial resolution of 1 m in the horizontal plane and originated from an airborne laser scanning (ALS) campaign in 2006 by the Martin Luther University, Halle-Wittenberg, Germany. The DEM was resampled to a 5 m resolution for processing the webcam photographs. The resampling can be seen as an adjustment to the lower webcam resolution. Both DEM

are referenced to the coordinate system of the Landsat images, which is the Universal Transverse Mercator (UTM) system based on the World Geodetic System 1984 (WGS84).

3 Model routines

PRACTISE v.2.1 introduces two major enhancements compared to version 1.0; the snow classification in partially shadow-affected photographs (subsect. 3.1) and the threshold calibration for optimal NDSI based snow cover maps (subsect. 3.2). In addition, all existing routines have been refined with respect to performance and user-friendliness (subsect. 3.3). The new routines (subsect. 3.1 and 3.2) and the flow chart (subsect. 3.3) of PRACTISE v.2.1 will be exemplarily presented for a SLR photograph and a Landsat 7 ETM+ image of Zugspitzplatt on 17 November 2011.

3.1 Snow classification in partially shadow-affected photographs

PRACTISE v.1.0 provides two snow classification routines for terrestrial RGB photographs. The user can select between a manual routine, which basically detects snow for digital numbers (DN) above user-specific snow thresholds in the red, green, and blue (RGB) bands of the digital photograph and an algorithm developed by Salvatori et al. (2011). This algorithm is a threshold based procedure, which automatically analyses the blue band DN frequency histogram and sets the snow threshold. Both classification types of PRACTISE v.1.0 are described in detail in Härer et al. (2013).

Both algorithms are working well if the photography is evenly illuminated and in the absence of shadows (Härer et al., 2013). However, shadow-free situations are rare in structured terrain and clouds can reason further shadowing. In the case of shaded areas, the two included classification routines tend to only identify snow surfaces that are sunlit while the classification in shaded areas has high uncertainties. This results from similarly high blue band DN in RGB images for shaded snow cover, and illuminated rock, soil, or sparsely vegetated surfaces (figs. 2.3-3a and b).

PRACTISE v.2.1 therefore includes a new classification routine, which automatically detects snow in shadow-affected photographs. The algorithm includes the automatic blue band classification from PRACTISE v.1.0 to identify the sunlit snow cover in the RGB images and additionally uses a principal component analysis (PCA) for separating shaded snow cover from sunlit rock surfaces. The method was

developed analyzing photographs in the Zugspitzplatt catchment and in the Vernagtferner area, Austria. The routine will be presented for the SLR photograph on 17 November 2011.

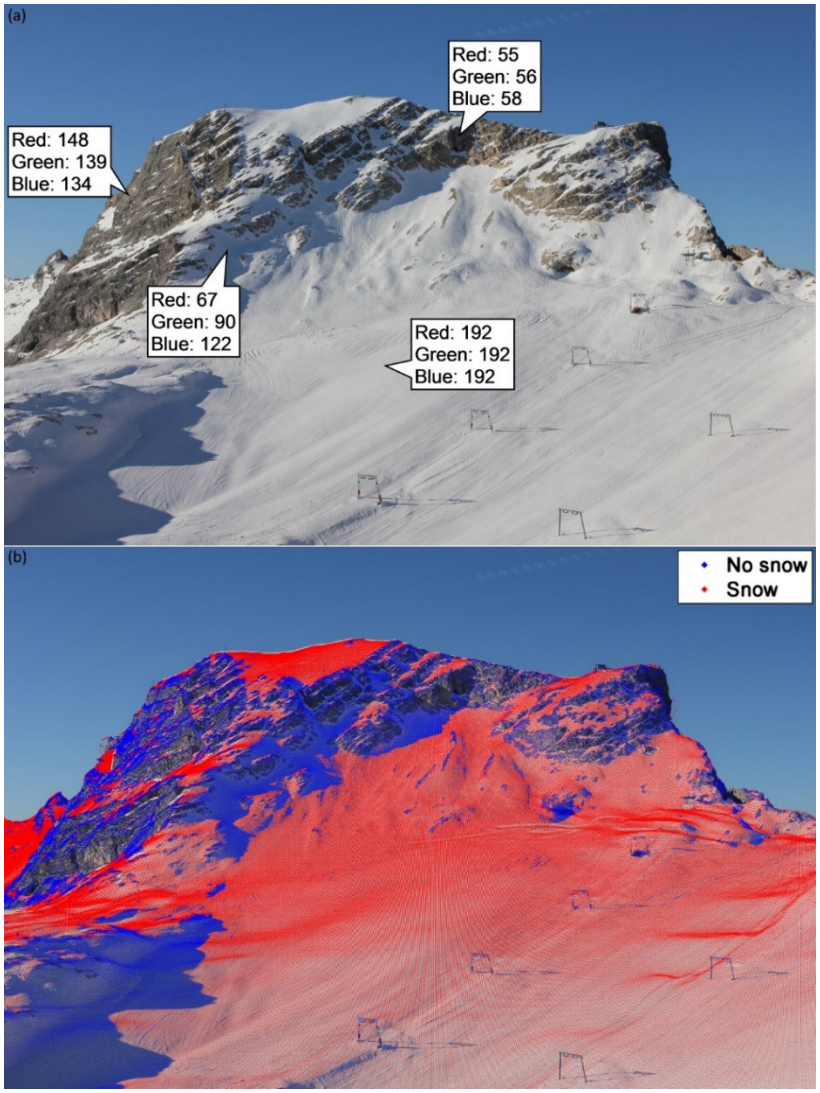

Figure 2.3-3: SLR photograph of Schneefernerkopf with large shadows on 17 November 2011: (a) the outlined RGB values (8-bit data, from 0 to 255) for the different surfaces show similarly high blue band values for shaded snow cover and illuminated rock areas. (b) Hence, shaded snow cover is erroneously classified as *free of snow* in the algorithm of Salvatori et al. (2011).

In a first step, the algorithm of Salvatori et al. (2011), described in Härer et al. (2013), is used for classifying snow at sunny locations. Snow cover detected in this step is illustrated in red in fig. 2.3-4.

The second step in the classification routine is the utilization of a PCA to detect snow cover in shaded areas. The PCA is a statistical method to analyse multivariate data sets. In our case, we use the PCA to orthogonally transform the axes of the RGB space to a new principal component (PC) space where the

center of the coordinate system is shifted to the mean value of the three-dimensional data set while the axis direction of the first PC (PC_1) explains the largest variance in the dataset. The axis of the second PC (PC_2) is orthogonal to PC_1 and explains the second largest variance. The axis of PC_3 is again orthogonal to PC_1 and PC_2. Due to the decreasing explained variance in the higher components, most information of the RGB data is stored in PC_1 and PC_2 while PC_3 mainly represents remaining noise.

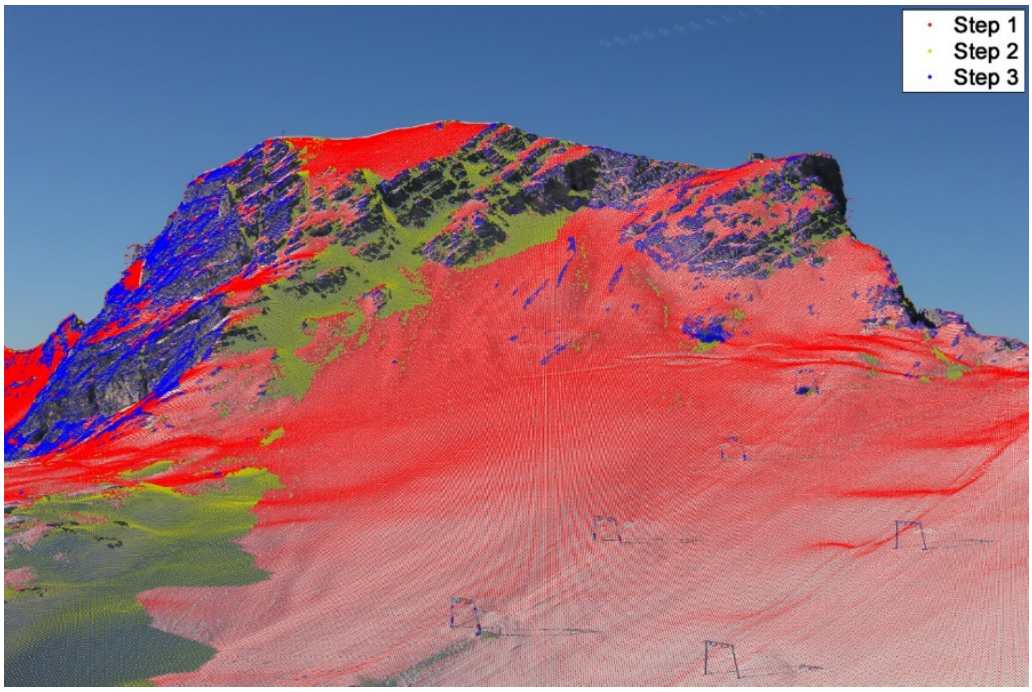

Figure 2.3-4: Stepwise classification of the SLR photograph on 17 November 2011 with the new PCA-based classification: in a first step, the algorithm of Salvatori et al. (2011) is used to classify sunlit snow (red). Then, shaded snow (yellow-green) is detected with the PCA classification, and in the third step, sunny rock (blue) is classified comparing blue and red band DN. All unclassified pixels after these steps, mainly shaded rock, are subsequently classified using the blue band DN (not shown here, see fig. 2.3-6).

For the PCA, the RGB values of all visible DEM pixels (N_{DEMv}) are standardized so that each colour column has a mean of 0 and a standard deviation of 1 ($\mathbf{RGB_s}$). The PC coefficients are calculated using a singular value decomposition. The $N_{DEMv} \times 3$ $\mathbf{RGB_s}$ matrix is then multiplied with the 3×3 PC coefficient matrix and results in the $N_{DEMv} \times 3$ PC score matrix ($\mathbf{PC_{sc}}$), which represents the standardized RGB values in the PCA space. The $\mathbf{PC_{sc}}$ has a decreasing explained variance from column 1 to 3 ($\mathbf{PC_{sc,1}}$ to $\mathbf{PC_{sc,3}}$) and is normalized by scaling between 0 and 1 in the last step.

Frequency histograms of the normalized PC score matrix ($\mathbf{PC_{sc,n,1}}$) for the columns 1 to 3 are illustrated in figs. 2.3-5a to c. The shape of the frequency histogram of $\mathbf{PC_{sc,n,1}}$ in the PCA space (fig. 2.3-5a) is essentially identical to the blue band DN frequency histogram in the RGB space. Hence, $\mathbf{PC_{sc,n,1}}$ is not analysed further as the first classification step already utilizes this information. But the frequency histograms of $\mathbf{PC_{sc,n,2}}$ and $\mathbf{PC_{sc,n,3}}$ are used and play a major role in the separation of shaded snow from other surfaces. Empirical analyses of numerous photographs have shown that shaded snow pixels have higher $\mathbf{PC_{sc,n,2}}$ than $\mathbf{PC_{sc,n,3}}$ values (figs. 2.3-5b and c).

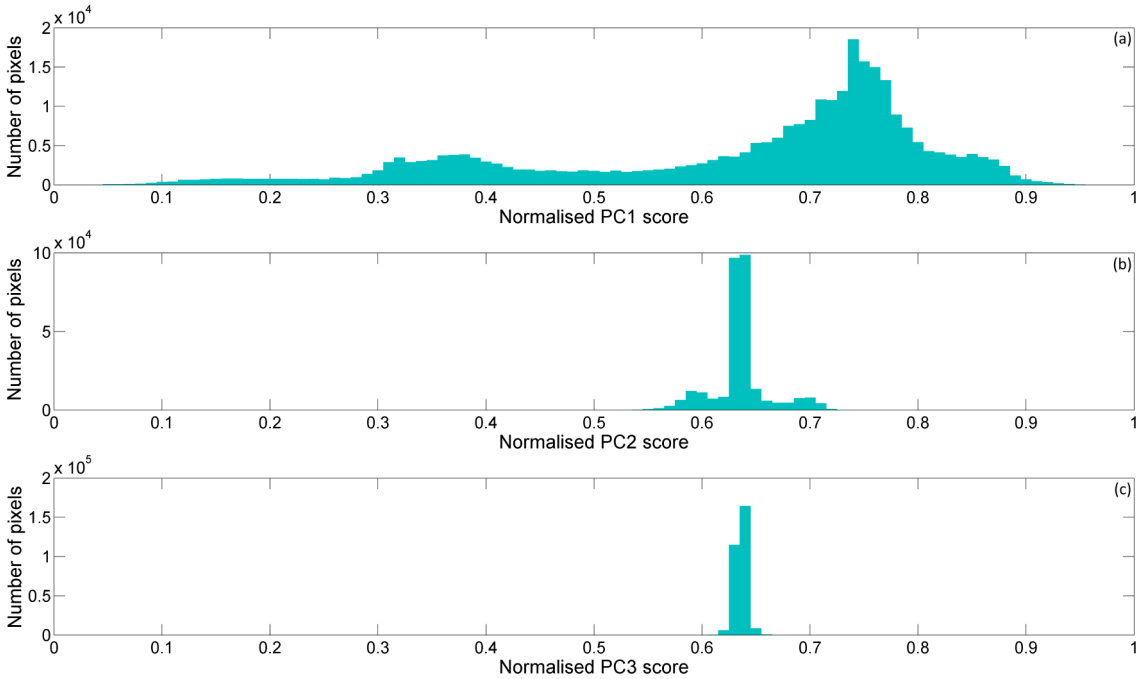

Figure 2.3-5: Frequency histograms of the normalized PC score matrix with decreasing explained variance from column 1 to 3 ($\mathbf{PC_{sc,n,1}}$ to $\mathbf{PC_{sc,n,3}}$): while the information stored in $\mathbf{PC_{sc,n,1}}$ (a) is largely redundant with the information given and analysed by the blue band of the RGB space, the PCA facilitates the separation of shaded snow cover from other surfaces by comparing $\mathbf{PC_{sc,n,2}}$ (b) to $\mathbf{PC_{sc,n,3}}$ (c) values using eq. (2.3-3).

For the used example, this means that shaded snow cover is grouped in the local maximum around 0.7 in the frequency histogram of $\mathbf{PC_{sc,n,2}}$ (fig. 2.3-5b). As a consequence, pixels are classified as snow where

$$\mathbf{PC3}_{\mathrm{sc,n}} < \mathbf{PC2}_{\mathrm{sc,n}} \text{ and } \mathrm{DN_{b,th}} \geq \mathrm{DN_b} \geq 63. \qquad (2.3\text{-}3)$$

A blue band DN (DN_b) condition is additionally included as first, all pixels with DN_b greater or equal to the derived snow threshold ($DN_{b,th}$) are already classified as snow in the first step of the routine. Second,

very dark pixels in the blue band with DN_b lower than one-fourth of the DN range (63) have been identified as prone to snow misclassifications. The snow cover derived from the PC analysis step is coloured in yellow-green in fig. 2.3-4.

The third step of the algorithm detects sunny rocks utilizing the DN in the blue and the red band (DN_r). Reflectance values of most rock surfaces increase from shorter to longer visible wavelengths and hence from blue to red. This characteristic can also be observed in the RGB values of the sunny rock surface in fig. 2.3-3a. Pixels not classified in the first two steps are identified as sunny rocks for

$$\mathrm{DN_r} \geq \mathrm{DN_b}. \tag{2.3-4}$$

The detected rock surfaces are depicted in blue in fig. 2.3-4.

Finally, pixels not classified in the three steps before ($DN_{b,n}$) are assigned snow probability values (P_s) from 0 for no snow to 1 for snow linearly increasing from low to high DN_b. P_s is not a statistically derived variable but is a helpful indicator as the probability of a snow-covered pixel increases with higher reflectance values in the blue spectrum. P_s is calculated using

$$P_\mathrm{s} = \frac{\mathrm{DN_{b,n}} - (\max(63, \min(\mathrm{DN_{b,n}})) - 1)}{\mathrm{DN_{b,th}} - (\max(63, \min(\mathrm{DN_{b,n}})) - 1)}. \tag{2.3-5}$$

Negative P_s values are set to 0, no snow, as we assume that pixels with DN_b below or equal to one-fourth (63) of the DN range (255) are areas free of snow. It should be noted that the blue band threshold of 63 in eqs. (2.3-3) and (2.3-5) can be adjusted by the user even though this was not necessary for any analysed photograph throughout the development of the routine.

Results of the newly implemented snow classification routine are illustrated in fig. 2.3-6 and can be compared to the results of v.1.0 in fig. 2.3-3b. At last, we want to mention that the new routine and in particular the PC analysis step was successfully applied in at least 95 % of our shadow-affected test photographs. For shadow-free situations, it is though still recommended to use the existing classification routines presented in Härer et al. (2013).

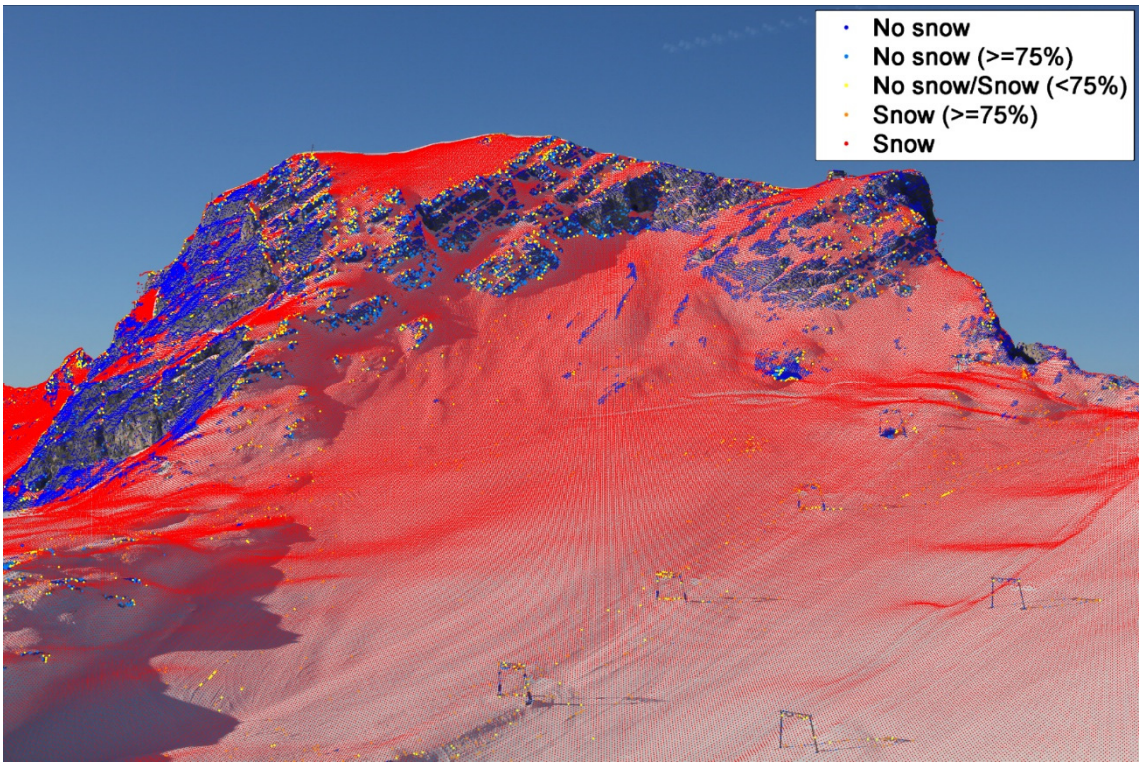

Figure 2.3-6: Results of the PCA-based classification of the SLR photograph on 17 November 2011: snow is classified in red, snow-free areas are depicted in blue. The pixels classified as *probably snow* (orange), *probably no snow* (light blue) and *highly unsure* (yellow) are enlarged for the sake of clarity. Only about 3.6 % of all classified pixels fall within one of the three probability categories and hence are assumed as *unsure*.

3.2 Threshold calibration for optimal NDSI based snow cover maps

The new approach to automatically derive an optimal NDSI based snow cover map is implemented in the second new module of PRACTISE v.2.1. The method utilizes areas that show an overlap between a photograph snow cover map and the NDSI product of a simultaneously captured satellite scene. Then, the NDSI threshold value for snow is calibrated using the dynamically dimensioned search (DDS) optimization algorithm (Tolson and Shoemaker, 2007) to obtain an optimal agreement of photograph and satellite snow cover map.

The photograph snow cover map is the ground truth data in the calibration and results from the georectification and classification of a terrestrial photograph in PRACTISE v.2.1. The NDSI map is calculated within the program evaluation for radiometrically and geometrically corrected Landsat data. The Landsat level 1 data are freely available from the archives of the US Geological Survey. The top of atmosphere planetary reflectance values of the green, near-infrared, and mid-infrared bands of Landsat

5, 7, or 8 images are automatically derived from the DN in accordance to the Landsat 5, 7, or 8 user handbook including a correction for the sun angle. For example, for Landsat 7 imagery the metadata file and the data bands 2 (GREEN, 0.52–0.60 µm), 4 (NIR, 0.77–0.90 µm), and 5 (MIR, 1.55–1.75 µm) are used in here. The NDSI is calculated on the basis of the reflectance values according to eq. (2.3-1) (Dozier, 1989; Hall et al., 1995). We want to highlight that externally produced NDSI maps from satellites like Spot, MODIS Aqua, and MODIS Terra can also be directly used.

If the Landsat scene is partially cloud covered, an externally generated cloud mask should be used to prevent misclassifications. A direct input link for the cloud mask product of the freely available Fmask software of Zhu et al. (2015) is integrated in PRACTISE to mask clouds, cloud shadows and water. The near-infrared condition of eq. (2.3-2) (Dozier, 1989; Hall et al., 1995), which is used to prevent water surfaces from being classified as snow is also applied here for masking strongly shaded pixels prone to misclassifications.

Overlapping areas of terrestrial photography and the satellite image are subsequently detected. The results of the photograph snow cover maps are used as a baseline. It is a user's decision if pixels classified as unsure in the photograph are excluded or used in weighted form according to their probability value. The user's selection, however, only affects the NDSI threshold calibration of the satellite image while the photograph snow cover map remains unchanged.

Now, the DDS optimization routine, which is also implemented in the framework of the GCP optimization (cf. Härer et al., 2013), is used to optimize the NDSI threshold value. The seed is set to the threshold of 0.4, recommended by Dozier (1989), and Hall et al. (1995) and the NDSI threshold value is limited to the range of NDSI values, which can be found in the overlapping area. The number of maximum iterations is user-dependent, but it was found that 150 optimization runs are sufficient. A quality measure of Aronica et al. (2002), which was successfully used in the context of snow extent evaluation in Bernhardt and Schulz (2010) serves as the objective function value *F* in the optimization:

$$F = \frac{a+d}{n}, \tag{2.3-6}$$

n is the overall number of photo-satellite image pixel pairs whereas *a* represents the number of correctly

identified snow pixels and *d* the same for snow-free pixels. *F* takes on values between 0 and 1 with 1 indicating a perfect agreement between the two images.

The routine is exemplarily presented for the SLR photograph of 17 November 2011 and the simultaneously captured Landsat 7 ETM+ satellite image of the Zugspitze massif. All photograph classification results from subsect. 3.1 are used in the NDSI threshold calibration. A Fmask satellite cloud mask is additionally utilized to the near-infrared condition of eq. (2.3-2) for reasons of cloud cover in the investigated area even though not visible in the Landsat Look image (fig. 2.3-2a). Tests for several scenes of Landsat 7 and 8 have shown that masking clouds with a cloud probability of 95 % and a surrounding buffer of three pixels in Fmask is reasonable in this application. The buffer secures that the satellite pixels used are not influenced by the thin edges of clouds and cloud shadows, which could potentially lead to misclassifications.

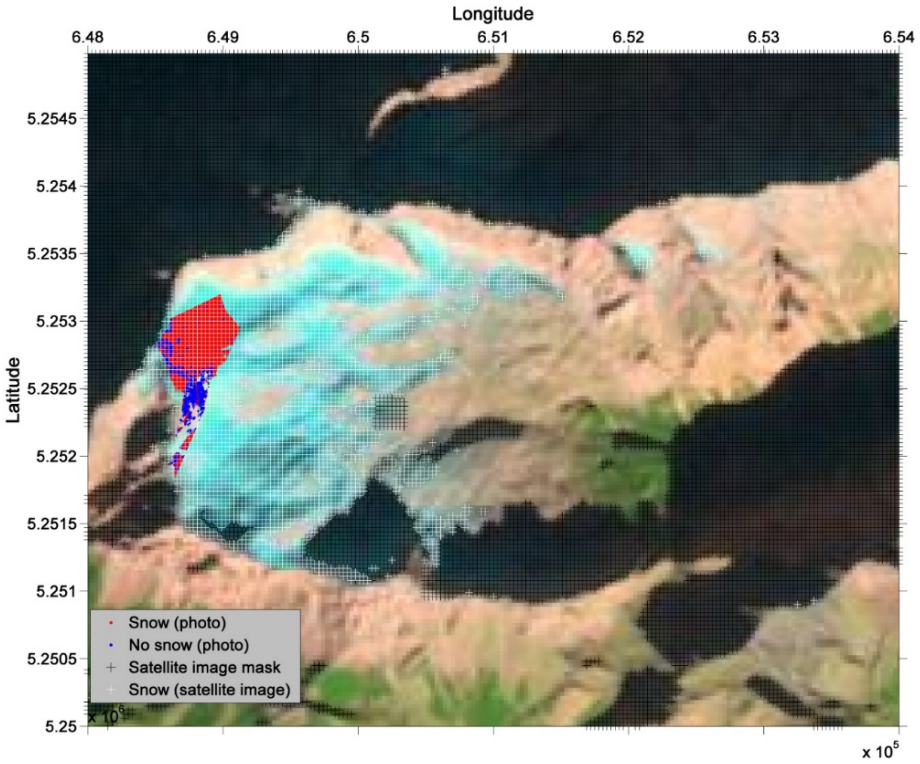

Figure 2.3-7: Resulting snow cover maps of the SLR photograph and the Landsat 7 ETM+ image on 17 November 2011 for the Zugspitze massif superimposed on the Landsat Look image: snow cover is illustrated in red and areas *free of snow* in blue for the photographed area. Unsure photo classification results are not shown for reasons of clarity even though used in the NDSI threshold calibration. White crosses depict snow cover in the satellite data using the calibrated NDSI threshold of 0.18. Masked areas including clouds and shadows are displayed with black crosses. Areas in the Landsat Look image not superimposed with crosses are snow-free satellite pixels.

The photograph and satellite snow cover maps of the SLR photograph and the Landsat 7 ETM+ image with an optimized NDSI threshold of 0.18 are illustrated in fig. 2.3-7. The classification agreement in the overlapping area of photograph and satellite is 97 %. The snow cover extent amounts to 2.8 km^2 and the masked area due to shadows and clouds covers an area of 3.6 km2 for this date. The areal coverages are calculated for the alpine Zugspitzplatt catchment (~13.1 km^2, fig. 2.3-1) defined by the catchment outlet at the Partnach spring.

3.3 Interactive modules, code improvements and the flow chart

In addition to the two new routines (subsect. 3.1 and 3.2), the code and the user-friendliness of the existing modules in PRACTISE v.2.1 have been improved.

Interactive modes are now available in the modules, optimization of the camera location and orientation and snow classification, which allows the user to directly interact with the software during runtime. Hence, the user can now interactively restart and refine the optimization of the exterior and interior camera parameters without the need to restart the complete program evaluation. The interactive mode in the snow classification module allows for switching between the three snow classification routines described in subsect. 3.1. The classification parameters for the different algorithms can also be adapted. The user can thus directly decide on the best classification method and parameters for each photograph.

PRACTISE v.2.1 is now also able to process photographs that were taken from camera locations sheltered by for example a roof and thus are assumed below ground in a DEM. In this case, surrounding DEM pixels will obstruct the view in the viewshed calculation. For omitting this problem, the user can now create a radial zone around the camera location where DEM pixels are assumed transparent. In addition to the improvements mentioned here, we refer the reader to the manual accompanying this paper for the description of other adaptations in the new version of PRACTISE, in particular regarding the data handling and naming conventions of input and output data.

The new routines are presented in detail for the SLR photograph and Landsat 7 ETM+ satellite image of Zugspitzplatt on 17 November 2011 (subsect. 3.1 and 3.2). Figure 2.3-8 now illustrates the general flow chart of PRACTISE v.2.1. All modules, including the new routines, are active. The program

evaluation starts with the reduction of the positional inaccuracy of the GCPs by optimizing the estimated camera parameters.

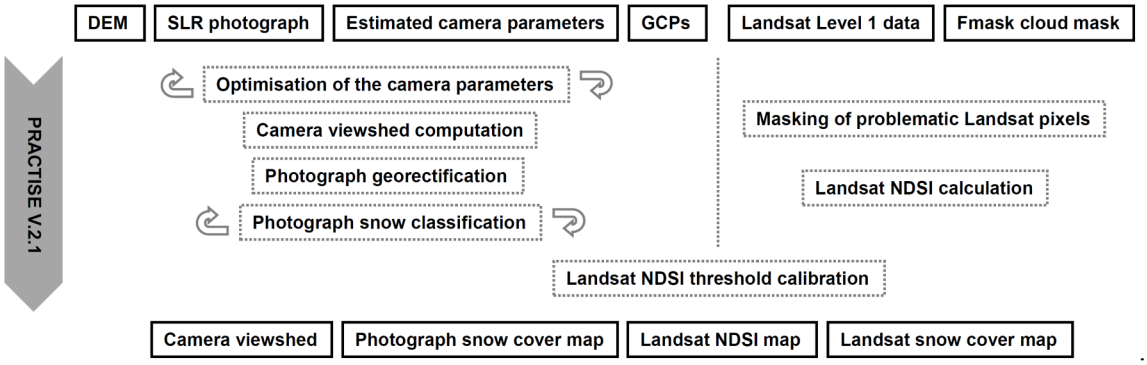

Figure 2.3-8: General flow chart of PRACTISE v.2.1 for the SLR photograph and Landsat 7 ETM+ image on 17 November 2011: inputs needed and output data generated in the PRACTISE run are depicted in solid black boxes at the top, respectively, at the bottom. All modules (dashed boxes) are active in the program evaluation and are executed downwards. Arrows illustrate activated interactive modes in the modules as the user can restart and adapt these routines during the program evaluation.

The user can interactively restart or refine the optimization of camera location and orientation (subsect. 3.3). Then, the viewshed is calculated for the respective camera system and the georectification procedure is executed. All visible DEM pixels are subsequently classified as snow-covered or snow-free by using the automatic blue band snow classification routine described in detail in Härer et al. (2013). Interactively switching to other classification routines and adapting the classification parameters is possible here (subsect. 3.1). In a next step, the NDSI is calculated for Landsat pixels, which are not masked by the NIR condition in eq. (2.3-2) and an externally generated Fmask satellite image cloud mask (Zhu et al., 2015). Areas that are covered by terrestrial photography and satellite are eventually used to calibrate the NDSI threshold value (subsect. 3.2). Final outputs of the described PRACTISE run are snow cover maps based on the SLR photography and Landsat Level 1 data, a Landsat NDSI map and the computed viewshed.

The runtime of PRACTISE v.2.1 for this set-up with a photographed area of about 0.3 km^2 and a Landsat processing extent of 30 km^2 was about 58.6 s on an Intel Core i72600 CPU with 3.4 GHz utilizing 1.2 GB of memory (RAM). However, interactive modes were deactivated in the runtime measurement and hence the optimization of camera parameters with 3000 iterations (~0.58 s) was executed only once.

4 Results and Discussion

We have presented the functionality of PRACTISE v.2.1 in course of this paper. It incorporates all options available in PRACTISE v.1.0 with revised code and improved user-friendliness. Most important are, however, the new modules facilitating on the one hand the derivation of more reliable photography-based snow cover maps even in partially shaded areas. Furthermore, a completely new approach to create calibrated NDSI thresholds needed for the generation of snow cover maps based on satellite images was introduced.

While the new modules have been presented for a SLR photograph and a Landsat 7 ETM+ image on 17 November 2011 in subsect. 3.1 and 3.2, we evaluate the software for two dates, 1 July 2013 and 7 April 2014. SLR and webcam photographs, as well as Landsat 7 or Landsat 8 scenes of the Zugspitzplatt are available for these dates. The scene of 1 July 2013 is partially cloud covered and therefore a Fmask satellite cloud mask was additionally utilized to the near-infrared condition of eq. (2.3-2).

In a first step, the quality of the photography-based snow cover maps was assured. The positional accuracy of the GCPs after the optimization of camera parameters is exemplarily illustrated for the SLR and webcam photographs on 7 April 2014 in fig. 2.3-9a and b. The root mean square error (RMSE) between GCPs and control points is 0.5 and 2.2 m, respectively. Both RMSE values are thus smaller than the spatial resolution of the DEMs used (1 m for the SLR photograph and 5 m for the webcam photograph). This was also confirmed for the two other dates used in this study. Further, the positional inaccuracy of the GCPs in the photographs is always smaller than in the Landsat scenes. The mean RMSE value in the presented Landsat scenes is 5.8 m.

Misinterpretations in the georectification and as a result in the classification were only found for snow groomers and some infrastructure not represented in the DEM and viewshed. An example of these obstacles leading to misinterpretations is an antenna in the center of the webcam photographs (cf. fig. 2.3-9b). As the number of pixels affected by this and similar problems is less than 0.5 % of the mapped area, the georectification quality of all camera images can be summarized as very high.

Figure 2.3-9: Real and calculated GCP positions for the investigated photographs on 7 April 2014: the root mean square error (RMSE) between real (green crosses) and calculated (red dots) GCP positions are 0.5 m for the SLR photograph (a) and 2.2 m for the webcam photograph (b) after the optimization of the camera parameters.

Figure 2.3-10a to d show the superimposed snow classifications (snow in red, no snow in blue) on the SLR and webcam photographs of 1 July 2013 and 7 April 2014. The July photographs in figs. 2.3-10a and b do not show strong shadowing effects due to the high sun angle at this date. Hence, the automatic blue band classification algorithm was used. The resulting classification visually indicates a high quality

and will not be further discussed here as the method was evaluated before in Salvatori et al. (2011) and Härer et al. (2013).

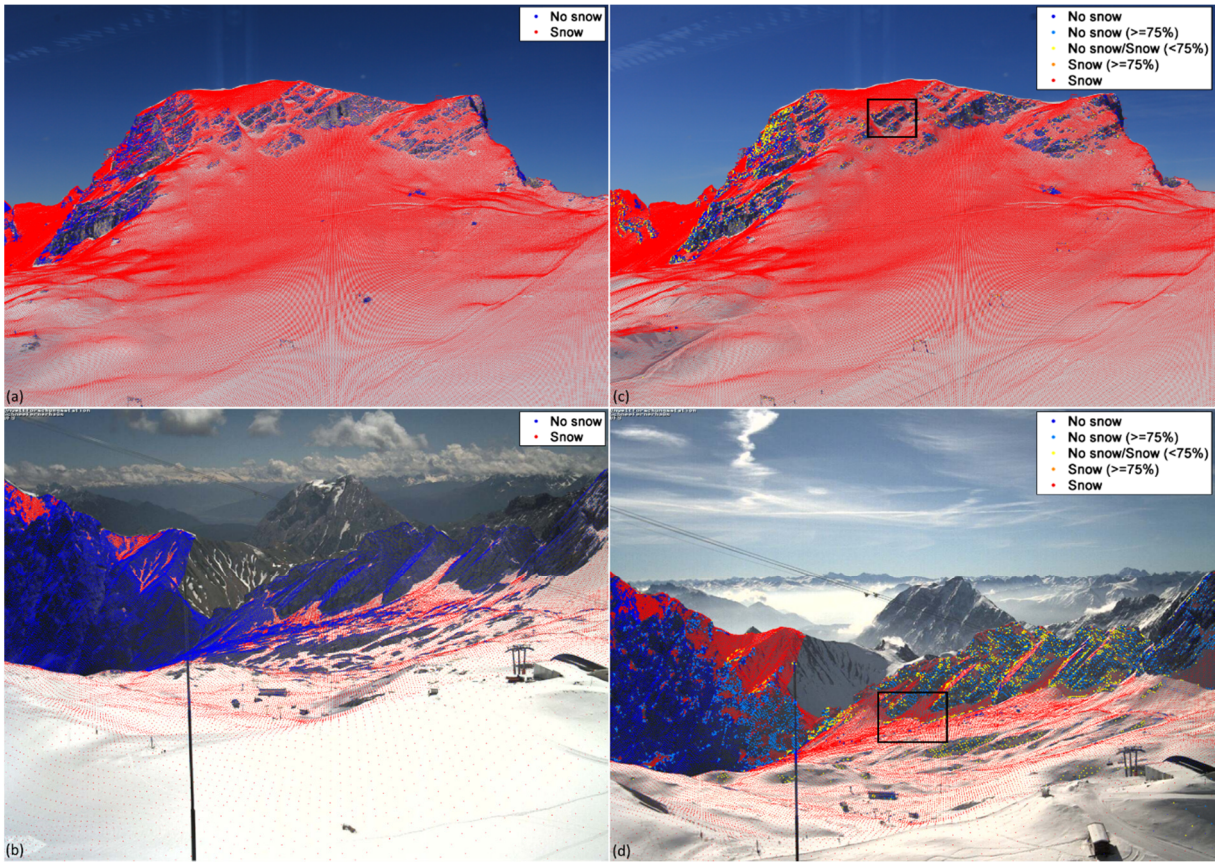

Figure 2.3-10: Superimposed snow classifications on the SLR and webcam photographs of 1 July 2013 and 7 April 2014: the SLR (a) and webcam (b) photographs of July 2013 utilized the blue band classification routine of Salvatori et al. (2011) depicting snow in red and no snow in blue. The new PCA-based classification method is, however, applied for the SLR (c) and webcam (d) photographs of April 2014. Here, snow and snow-free pixels are again displayed in red and blue but additionally unsure classification results are illustrated in light blue, yellow and orange for the categories *probably no snow*, *highly unsure*, and *probably snow*. Black rectangle boxes in (c) and (d) are depicted for detailed analyses of the classification accuracy (figs. 2.3-11a and b).

For the photographs of 7 April 2014, the PCA-based classification algorithm was applied to reduce shadow-related misclassifications (figs. 2.3-10c and d). The detailed visual analysis of the pixels in the two April photographs showed the high quality of the new classification routine for pixels identified as snow and free of snow as well as for pixels classified as probably snow, highly unsure, and probably no snow.

Misclassifications in the main classification categories snow and free of snow are rare with less than 0.3 % of classified pixels in the SLR photograph and less than 1 % in the webcam photograph. The reasons for misclassifications are, however, different in both photographs. In the SLR photograph, the misclassifications can mainly be attributed to the light-coloured bare rock (limestone) in the Zugspitzplatt area, which is mistakenly classified as snow. This issue has already been discussed in detail in Härer et al. (2013, PRACTISE v.1.0) and is a weakness of the blue band classification method, which represents one of the classification steps in the PCA-based classification routine. The misclassifications in the webcam photograph have two main origins: a georectification problem due to infrastructure, which has already been mentioned above, and another problem, as shaded areas, in particular in the valley below the Zugspitzplatt, are difficult to classify as snow and no snow, even with the human eye.

In addition to the two main classification categories, the three unsure categories need to be discussed for the April photographs; 1.9 % of classified pixels in the SLR photograph and 7.8 % in the webcam image are assigned probability values. The low percentages emphasize that the assignment rules in the PCA-based classification routine seem to describe the RGB characteristics of the different surfaces well. In addition, most pixels classified as unsure in the SLR photograph are exactly located at the transitional area between snow patches and snow-free areas in the photographs, and can therefore be seen as mixed pixels (figs. 2.3-10c and 2.3-11a). The classification of the SLR photograph on 17 November 2011 (fig. 2.3-6) has also attested this finding.

In the webcam photograph, more pixels are classified as unsure in particular as probably no snow (figs. 2.3-10d and 2.3-11b). The detailed analysis also shows some no snow misclassifications in the webcam photograph, especially in the transitional zone between sunny and shaded snow. Taken together, both issues concern less than 0.5 % of the classified pixels and are only observed in the webcam photograph. As the SLR photographs in TIFF-format, allowing for data compression without loss, are unaffected, the lower image quality and the JPEG compression of the webcam image are the reason for more unsure classifications and the misclassification issues. Hence, such uncertainties and small errors have to be expected in the context of any analysis that uses JPEG images. Overall, the new classification

technique separates sunny as well as shaded snow cover from other surfaces with a similarly high accuracy as the blue band classification does classify equally illuminated photographs.

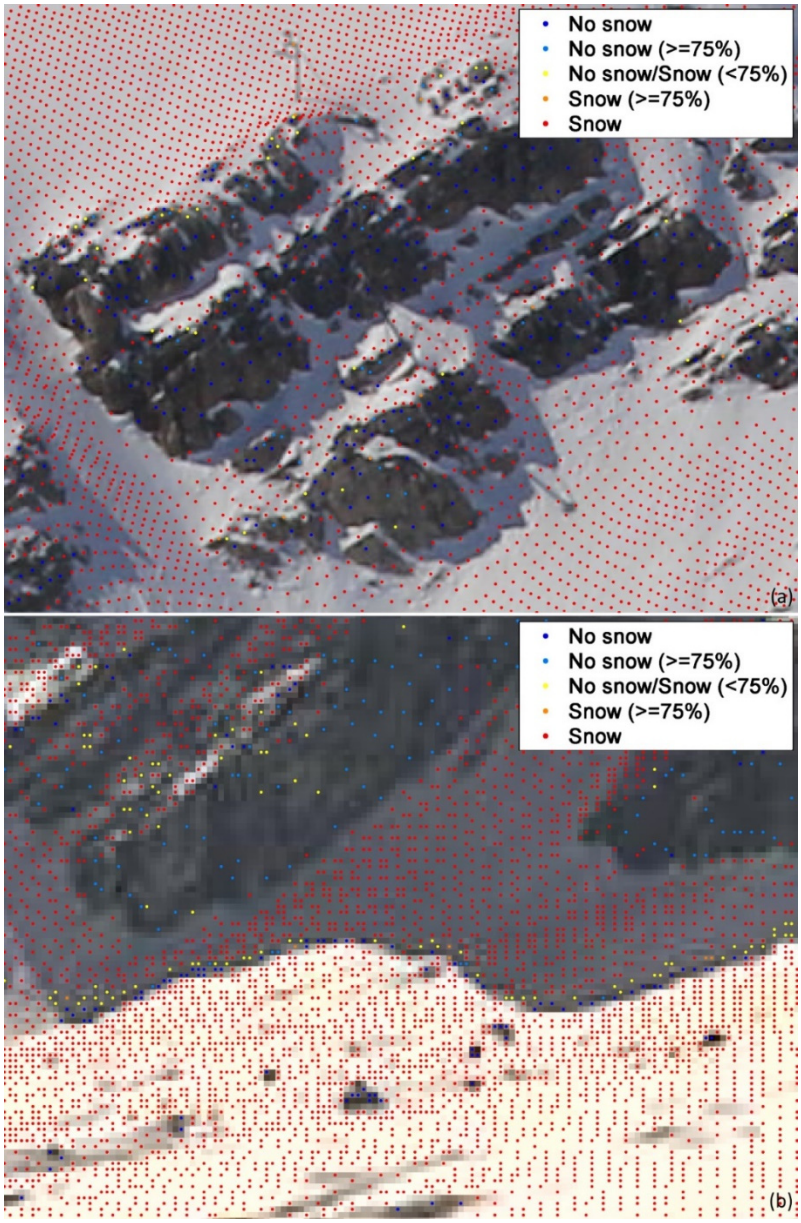

Figure 2.3-11: Enlarged view of the superimposed snow classifications on the SLR and webcam photographs of 7 April 2014 (rectangle boxes in figs. 2.3-11c and d): (a) unsure classification results in the SLR photograph are located at transitional areas between snow patches and snow-free areas. (b) In the webcam photograph, more pixels are classified in the three *unsure* categories. Moreover, some *no snow* misclassifications are found in the transitional zone between sunny and shaded snow cover.

In a second step, the calibration of the NDSI threshold of the Landsat images was evaluated. At first, the results of the Landsat 7 ETM+ satellite image of 1 July 2013 are presented. The SLR-calibrated NDSI threshold of this Landsat scene is 0.35 with 94 % of the photo snow cover map being identical

to the calibrated satellite image snow cover map. The calibration of the NDSI threshold using the webcam photograph results in a threshold of 0.37. Here, the classification agreement of the snow cover is with 84 % slightly lower but still high. In the Landsat 8 OLI satellite image of 7 April 2014, the NDSI threshold optimized with the SLR photograph is 0.23 (94 % agreement). An identical NDSI threshold of 0.23 (90 % agreement) was found for the simultaneously captured webcam photograph. The snow cover maps from the SLR and webcam photographs as well as from the SLR-calibrated satellite images are depicted in fig. 2.3-12a for 1 July 2013 and in fig. 2.3-12b for 7 April 2014. The SLR-derived snow-covered area in the Zugspitzplatt catchment amounts to 6.5 km^2 for the July date, respectively 9.9 km^2 for the April date. Masked areas are 1.3 km^2 on 1 July 2013 and 0.9 km^2 on 7 April 2014 due to shadows and clouds.

We want to emphasize here that the percentage of pixels identically classified in photograph and satellite image maps is enormously high, keeping in mind the different horizontal resolutions of photograph map (SLR: 1 m, webcam: 5 m) and satellite image map (30 m). The resolution effect becomes more pronounced for patchier snow cover, in this case in the lower Zugspitzplatt area, which also explains the slightly lower agreement between webcam photograph and satellite image.

Another important finding is that the calibration of the NDSI threshold using SLR and webcam results in almost identical NDSI thresholds. As the differences are insignificant the NDSI threshold calibration seems to be robust in the Zugspitzplatt area independent of the used camera system and field of view.

At last, the changing NDSI thresholds of 0.18 on 17 November 2011, 0.35 on 1 July 2013, and 0.23 on 7 April 2014 calibrated with the SLR camera need to be discussed. All thresholds are below the value of 0.4 from Dozier (1989) and Hall et al. (1995) and the increases of snow cover extent in the Zugspitzplatt catchment are between 3.7 % on 1 July 2013 and 26.7 % on 17 November 2011 using the calibrated NDSI threshold values instead of the literature value of 0.4. Consequently, larger differences between the optimized and the standard NDSI threshold value lead to a higher percentage change of snow cover.

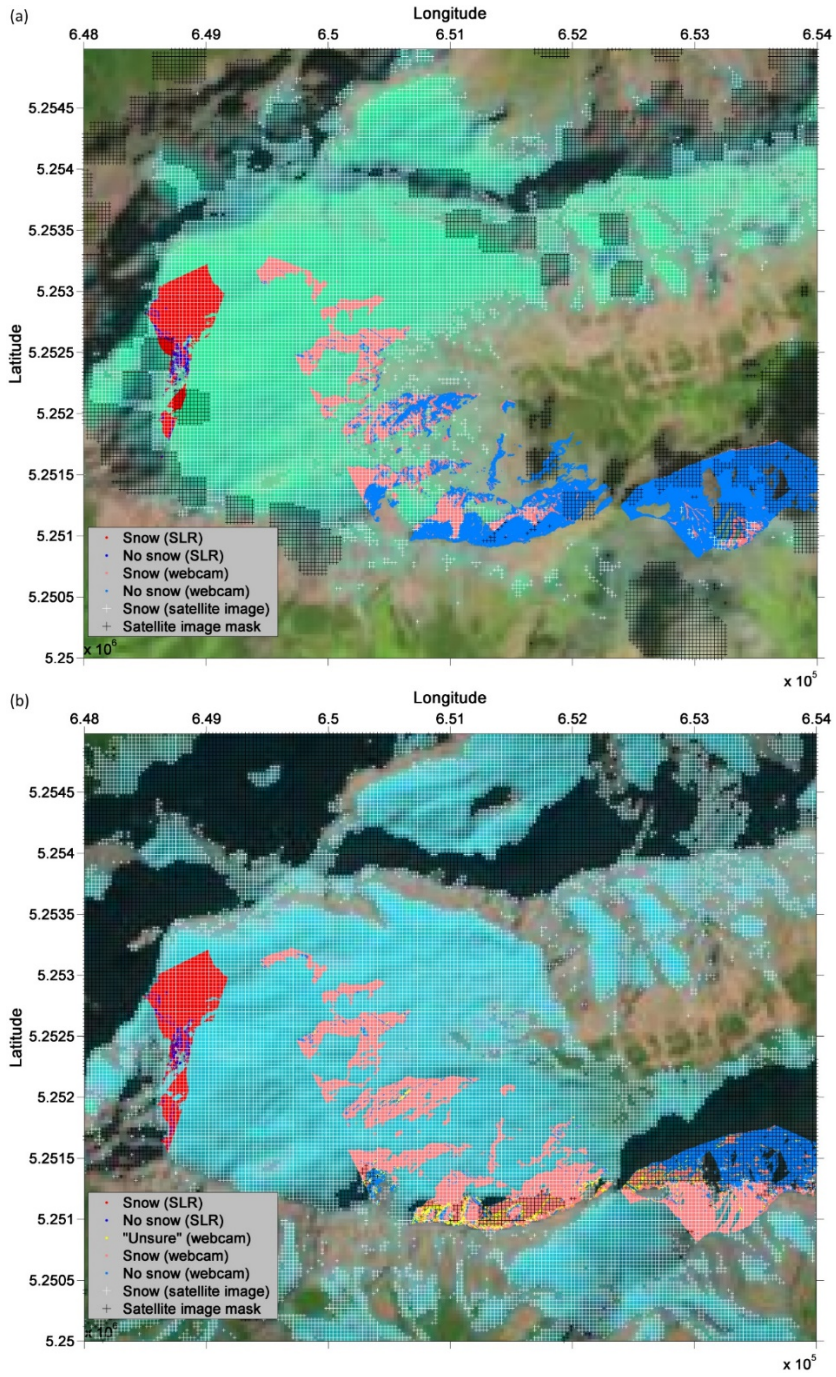

Figure 2.3-12: Resulting snow cover maps of the SLR and webcam photographs, and the Landsat images for the Zugspitze massif superimposed on the Landsat Look images: the satellite snow cover maps are calibrated using the SLR snow cover maps as a baseline. The resulting NDSI thresholds are 0.35 for 1 July 2013 (a) and 0.23 for 7 April 2014 (b). Snow cover in the satellite data is illustrated with white crosses, masked areas with black crosses mainly due to clouds in (a) and shadows in (b). Pixels not superimposed with crosses are areas classified as *free of snow* in the satellite images. The photograph snow cover maps display *snow* and *no snow* in red and blue for the SLR and in light red and light blue for the webcam. *Unsure* snow classification results only occur for the photographs on 7 April 2014 (b) as the PCA-based classification routine is applied and are only shown for the webcam (yellow) as the percentage of unsure snow classifications in the SLR photograph (figs. 2.3-10c and 2.3-11a) is negligible.

Figures 2.3-13a to c display the optimized snow cover maps (light blue) in the Zugspitzplatt for the three investigated dates in chronological order. They are superimposed with the standard snow cover maps (dark blue). The visual comparison of the snow cover maps clearly shows that especially the edges of the snow cover are reclassified to snow whereas no new large snow patches are identified. This demonstrates on the one hand that the core snow cover areas are already correctly classified using the standard threshold. On the other hand, this result also highlights that Landsat snow pixels at the snow cover edge, and hence probably mixed pixels, represent a substantial portion of snow cover in alpine areas and thus have to be correctly classified for optimum results.

In addition to the visual analysis, we analysed changes in the elevation distribution of snow-covered pixels in the Zugspitzplatt area, in particular of the lower elevation snow cover. As the lowest elevation where snow cover is detected is not necessarily representative of the current snow cover distribution in the investigation area, the 10 % quantile of the elevation values of snow-covered pixels was calculated. The resulting elevations for the 10 % quantile are 2390.6 m on 17 November 2011, 2261.4 m on 1 July 2013, and 1948.8 m on 7 April 2014 for the literature NDSI threshold, and, respectively, 2352.1, 2251.5, and 1938.6 m for the optimized NDSI thresholds. The elevation differences between the standard and the optimized method consequently range between 9.9 m for the July date and 38.5 m for the November date. The increase of snow-covered areas in lower elevations using the lower optimized NDSI threshold values might be expected. However, about 10 m and in an extreme case about 40 m elevation change in lower elevation snow cover can make a huge difference, for example, when applied in climate change studies.

The presented values and findings underline that the strong temporal variations found in NDSI thresholds transfer to large uncertainties in the derivation of snow cover extents and studies relying on these snow cover products. A spatial and temporal adjustment of NDSI thresholds is therefore important to ensure optimum results in the snow cover mapping of specific areas, for example of the studied alpine catchment.

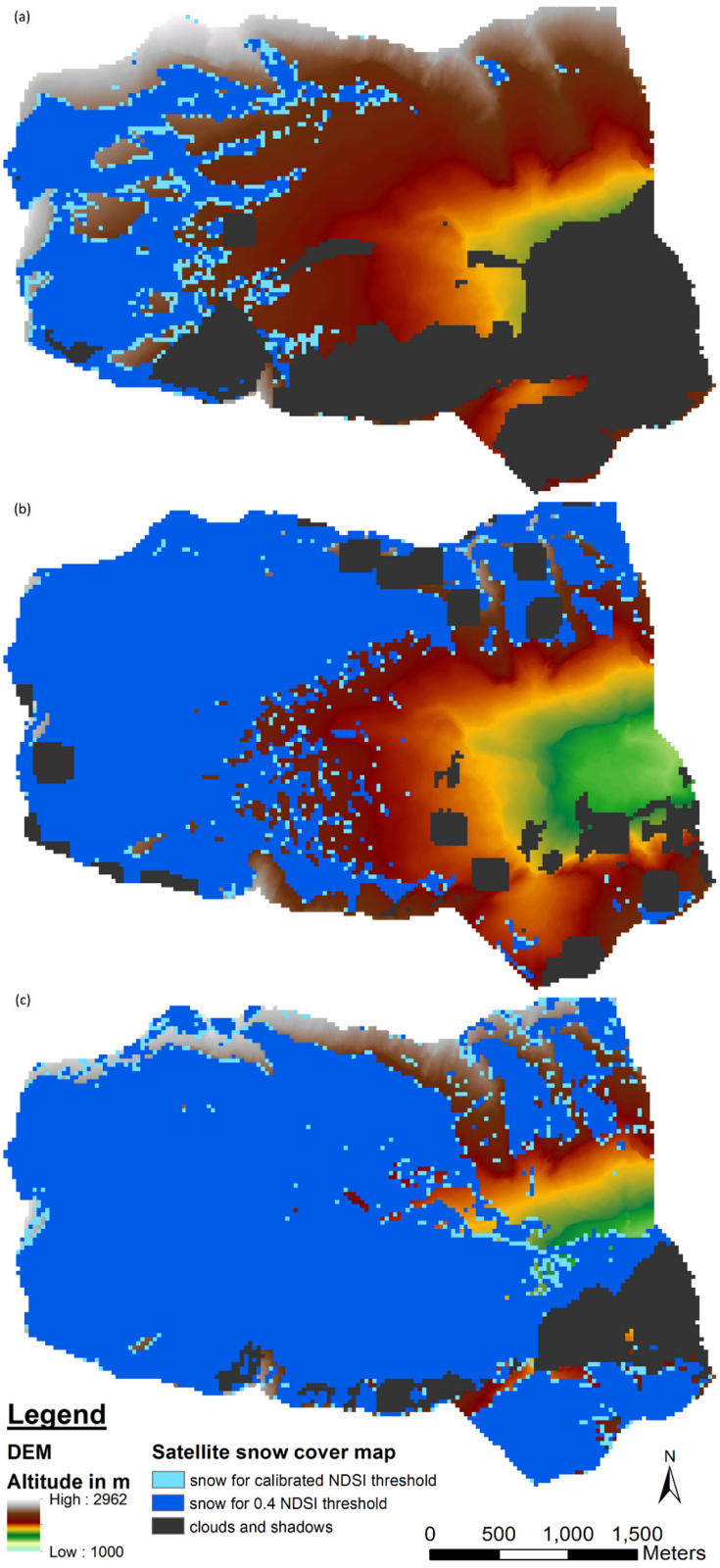

Figure 2.3-13: Standard and optimized snow cover maps of the Zugspitzplatt catchment for 17 November 2011 (a), 1 July 2013 (b), and 7 April 2014 (c): snow cover extents using the standard NDSI threshold value of 0.4 are depicted in dark blue, additionally detected snow cover using the SLR-calibrated NDSI threshold values of 0.18 (a), 0.35 (b), and 0.23 (c) in light blue, and clouds and shadows in dark grey. The snow cover maps are superimposed on the DEM of the investigation area (cf. fig. 2.3-1).

5 Conclusion and outlook

PRACTISE v.2.1 was already in the previous version a fast and user-friendly tool to georectify and classify photographs, but now further provides a new and objective method to automatically calibrate NDSI thresholds in satellite images and thus is able to create reliable, spatially, and temporally specific NDSI based satellite snow cover maps. The snow classification of photographs has moreover become more flexible with the additional opportunity to classify partially shadow-affected photographs. The code of the old version has additionally been revised and the user-friendliness has been improved while the functionality of all existing routines in PRACTISE v.1.0 remained.

PRACTISE v.2.1 is thus a simple and ready-to-use software tool that was developed and tested for SLR and webcam photographs, as well as Landsat 7 ETM+and Landsat 8 OLI satellite images in the Zugspitzplatt area. The successful use of webcam photographs in the calibration of the NDSI threshold of a Landsat 7 as well as a Landsat 8 scene further increases the transferability of this study to other areas. Obviously, when using freely available webcam infrastructure, the processing of PRACTISE needs an increased attention for any problems that may arise in the snow mapping due to image quality, lens distortion, and obstacles in the field of view.

Our next step will be to apply PRACTISE and the integrated new approach to the complete available time series of photographs and satellite images in the Zugspitzplatt area. In addition, we will process another long-term time series of photographs in the alpine Vernagtferner area, Austria, which is located in the same Landsat scene as the Zugspitzplatt. We think that this experimental set-up will be a first step towards understanding the temporal variability of the calibrated NDSI thresholds in alpine areas. Furthermore, the setup will also allow for testing spatial representativeness of the optimal NDSI threshold on the regional scale as this is another topic of ongoing discussion. This will be especially important as the spatiotemporal extrapolation possibilities and limits of the presented method are as yet unknown. Further research will also be necessary to verify if the synthesis of terrestrial photograph and satellite image is applicable in a modified form to other research fields like thermal photography and satellite imagery.

Code availability

The source code of PRACTISE v.2.1 is distributed under the Creative Commons license (CC-BY-NC-SA 4.0) and together with a manual and an example data set available online here: https://github.com/shaerer/PRACTISE/releases/tag/v2. 1 (doi:10.5281/zenodo.35646).

The software is executable on any Windows or UNIX computer with a basic Matlab installation and at least 2GB RAM. This means no additional Matlab packages are needed. Additionally, the current version of PRACTISE is also executable on Linux platforms using (64bit-enabled) Octave 4.0 and higher, an open-source alternative of Matlab. The code has been tested for compatibility with Matlab versions from 2005 and 2015 (both Windows 7) as well as Octave 4.0 (Linux Mint 17.1 and Ubuntu 14.04). We want to note here that the code is not executable using Octave 4.0 for Windows at the moment. The reason for that is simply that no precompiled 64bit-version of Octave 4.0 is available for Windows yet, which is though necessary to process large arrays in PRACTISE.

Please visit http://creativecommons.org/licenses/by-nc-sa/ 4.0 for further information on the used Creative Commons license and https://gnu.org/software/octave for information on GNU Octave.

Acknowledgements. The work described in this paper was supported by the doctoral scholarship program “Deutsche Bundesstiftung Umwelt” (DBU), the Helmholtz Research School “Mechanisms and Interactions of Climate Change in Mountain Regions” (MICMoR) and the Environmental Research Station Schneefernerhaus (UFS), as well as our previous palace of employment the Department of Geography at the LMU Munich. We also thank David Morche for providing the DEM, Michael Weber for occasional maintenance of the SLR camera, and Ben Müller, Nick Rutter and Karl-Friedrich Wetzel for thoughtful discussions.

Edited by: R. Sander

References

Aronica, G., Bates, P. D., and Horrit, M. S.: Assessing the uncertainty in distributed model predictions using observed binary pattern information within GLUE, Hydrol. Process., 16, 2001–2016, doi:10.1002/hyp.398, 2002.

Aschenwald, J., Leichter, K., Tasser, E., and Tappeiner, U.: Spatiotemporal landscape analysis in mountainous terrain by means of small format photography: a methodological approach, IEEE T. Geosci. Remote, 39, 885–893, doi:10.1109/36.917917, 2001.

Bernhardt, M. and Schulz, K.: SnowSlide: a simple routine for calculating gravitational snow transport, Geophys. Res. Lett., 37, L11502, doi:10.1029/2010GL043086, 2010.

Bernhardt, M., Schulz, K., Liston, G. E., and Zängl, G.: The influence of lateral snow redistribution processes on snow melt and sublimation in alpine regions, J. Hydrol., 424–425, 196–206, doi:10.1016/j.jhydrol.2012.01.001, 2012.

Bernhardt, M., Härer, S., Jacobeit, J., Wetzel, K. F., and Schulz, K.: The virtual alpine observatory – research focus Alpine hydrology, Hydrol. Wasserbewirts., 58, 241–243, 2014.

Blöschl, G., Kirnbauer, R., and Gutknecht, D.: Distributed snowmelt simulations in an Alpine catchment: 1. model evaluation on the basis of snow cover patterns, Water Resour. Res., 27, 3171–3179, doi:10.1029/91WR02250, 1991.

Brown, R. D. and Mote, P. W.: The response of Northern Hemisphere snow cover to a changing climate, J. Climate, 22, 2124–2145, doi:10.1175/2008JCLI2665.1, 2009.

Corripio, J. G.: Snow surface albedo estimation using terrestrial photography, Int. J. Remote Sens., 25, 5705–5729, doi:10.1080/01431160410001709002, 2004.

Corripio, J. G., Durand, Y., Guyomarc'h, G., Mérindol, L., Lecorps, D., and Pugliése, P.: Land-based remote sensing of snow for the validation of a snow transport model, Cold Reg. Sci. Technol., 39, 93–104, doi:10.1016/j.coldregions.2004.03.007, 2004.

Dietz, A. J., Kuenzer, C., Gessner, U., and Dech, S.: Remote sensing of snow – a review of available methods, Int. J. Remote Sens., 33, 4094–4134, doi:10.1080/01431161.2011.640964, 2012.

Dozier, J.: Spectral signature of alpine snow cover from the landsat thematic mapper, Remote Sens. Environ., 28, 9–22, doi:10.1016/0034-4257(89)90101-6, 1989.

Dumont, M., Arnaud, Y., Six, D., and Corripio, J. G.: Retrieval of glacier surface albedo using terrestrial photography, Houille Blanche, 2, 102–108, doi:10.1051/Lhb/2009021, 2009.

Garvelmann, J., Pohl, S., and Weiler, M.: From observation to the quantification of snow processes with a time-lapse camera network, Hydrol. Earth Syst. Sci., 17, 1415–1429, doi:10.5194/hess-17-1415-2013, 2013.

Groisman, P. Y., Karl, T. R., and Knight, R. W.: Observed impact of snow cover on the heat balance and the rise of continental spring temperatures, Science, 263, 198–200, doi:10.1126/science.263.5144.198, 1994.

Hall, D. K. and Riggs, G. A.: Accuracy assessment of the MODIS snow products, Hydrol. Process., 21, 1534–1547, doi:10.1002/hyp.6715, 2007.

Hall, D. K., Riggs, G. A., and Salomonson, V. V.: Development of methods for mapping global snow cover using moderate resolution imaging spectroradiometer data, Remote Sens. Environ., 54, 127–140, doi:10.1016/0034-4257(95)00137-P, 1995.

Hall, D. K., Riggs, G. A., Salomonson, V. V., Barton, J. S., Casey, K., Chien, J. Y. L., DiGirolamo, N. E., Klein, A. G., Powell, H. W., and Tait, A. B.: Algorithm theoretical basis document (ATBD) for the MODIS snow- and sea ice-mapping algorithms, available at: http://modis-snow-ice.gsfc.nasa.gov/?c=atbd&t=atbd (last access: 30 July 2015), 2001.

Härer, S., Bernhardt, M., Corripio, J. G., and Schulz, K.: PRACTISE – Photo Rectification And ClassificaTIon SoftwarE (v.1.0), Geosci. Model Dev., 6, 837–848, doi:10.5194/gmd-6-837-2013, 2013.

Hinkler, J., Pedersen, S. B., Rasch, M., and Hansen, B. U.: Automatic snow cover monitoring at high temporal and spatial resolution, using images taken by a standard digital camera, Int. J. Remote Sens., 23, 4669–4682, doi:10.1080/01431160110113881, 2002.

IPCC: Climate Change 2013: The Physical Science Basis, Contribution of Working Group I to the Fifth Assessment Report of the Intergovernmental Panel on Climate Change, edited by: Stocker, T. F., Qin, D., Plattner, G.-K., Tignor, M., Allen, S. K., Boschung, J., Nauels, A., Xia, Y., Bex, V., and Midgley, P. M., Cambridge University Press, Cambridge, UK and New York, NY, USA, 1535 pp., 2013.

Klemes, V.: The modelling of mountain hydrology: the ultimate challenge, IAHS-AISH P., 190, 29–43, 1990.

Lehning, M., Völksch, I., Gustafsson, D., Nguyen, T. A., Stähli, M., and Zappa, M.: ALPINE3D: a detailed model of mountain surface processes and its application to snow hydrology, Hydrol. Process., 20, 2111–2128, doi:10.1002/Hyp.6204, 2006.

Liston, G. E. and Elder, K.: A distributed snow-evolution modeling system (SnowModel), J. Hydrometeorol., 7, 1259–1276, doi:10.1175/JHM548.1, 2006.

Marty, C.: Regime shift of snow days in Switzerland, Geophys. Res. Lett., 35, L12501, doi:10.1029/2008GL033998, 2008.

Messerli, A. and Grinsted, A.: Image georectification and feature tracking toolbox: ImGRAFT, Geosci. Instrum. Method. Data Syst., 4, 23–34, doi:10.5194/gi-4-23-2015, 2015.

Nolin, A. W.: Recent advances in remote sensing of seasonal snow, J. Glaciol., 56, 1141–1150, doi:10.3189/002214311796406077, 2010.

Parajka, J., Haas, P., Kirnbauer, R., Jansa, J., and Blöschl, G.: Potential of time-lapse photography of snow for hydrological purposes at the small catchment scale, Hydrol. Process., 26, 3327–3337, doi:10.1002/Hyp.8389, 2012.

Pomeroy, J., Bernhardt, M., and Marks, D.: Water resources: research network to track alpine water, Nature, 521, 32, doi:10.1038/521032c, 2015.

Rivera, A., Corripio, J. G., Brock, B., Clavero, J., and Wendt, J.: Monitoring ice-capped active volcan Villarrica, southern Chile, using terrestrial photography combined with automatic weather stations and global positioning systems, J. Glaciol., 54, 920–930, doi:10.3189/002214308787780076, 2008.

Salvatori, R., Plini, P., Giusto, M., Valt, M., Salzano, R., Montagnoli, M., Cagnati, A., Crepaz, G., and Sigismondi, D.: Snow cover monitoring with images from digital camera systems, Ital. J. Remote Sens., 43, 137–145, doi:10.5721/ItJRS201143211, 2011.

Scherrer, S. C., Appenzeller, C., and Laternser, M.: Trends in Swiss Alpine snow days: the role of local- and large-scale climate variability, Geophys. Res. Lett., 31, L13215, doi:10.1029/2004GL020255, 2004.

Schmidt, S., Weber, B., and Winiger, M.: Analyses of seasonal snow disappearance in an alpine valley from micro- to mesoscale (Lötschental, Switzerland), Hydrol. Process., 23, 1041–1051, doi:10.1002/hyp.7205, 2009.

Tolson, B. A. and Shoemaker, C. A.: Dynamically dimensioned search algorithm for computationally efficient watershed model calibration, Water Resour. Res., 43, W01413, doi:10.1029/2005wr004723, 2007.

Viviroli, D., Dürr, H. H., Messerli, B., Meybeck, M., and Weingartner, R.: Mountains of the world, water towers for humanity: typology, mapping, and global significance, Water Resour. Res., 43, W07447, doi:10.1029/2006WR005653, 2007.

Viviroli, D., Archer, D. R., Buytaert, W., Fowler, H. J., Greenwood, G. B., Hamlet, A. F., Huang, Y., Koboltschnig, G., Litaor, M. I., López-Moreno, J. I., Lorentz, S., Schädler, B., Schreier, H., Schwaiger, K., Vuille, M., and Woods, R.: Climate change and mountain water resources: overview and recommendations for research, management and policy, Hydrol. Earth Syst. Sci., 15, 471–504, doi:10.5194/hess-15-471-2011, 2011.

Watt, A. and Watt, M.: Advanced Animation and Rendering Techniques: Theory and Practice, ACM Press, New York, NY, USA, 472 pp., 1992.

Winstral, A. and Marks, D.: Simulating wind fields and snow redistribution using terrain-based parameters to model snow accumulation and melt over a semi-arid mountain catchment, Hydrol. Process., 16, 3585–3603, doi:10.1002/hyp.1238, 2002.

Zhu, Z., Wang, S., and Woodcock, C. E.: Improvement and expansion of the Fmask algorithm: cloud, cloud shadow, and snow detection for landsats 4–7, 8, and sentinel images, Remote Sens. Environ., 159, 269–277, doi:10.1016/j.rse.2014.12.014, 2015.

2.4 Publication IV

The following text is an edited version of the 2017 The Cryosphere Discussion (TCD) article:

On the need of a time- and location-dependent estimation of the NDSI threshold value for reducing existing uncertainties in snow cover maps at different scales

Stefan Härer[1], Matthias Bernhardt[1], Matthias Siebers[2], Karsten Schulz[1]

[1] Institute for Water Management, Hydrology and Hydraulic Engineering (IWHW), University for life sciences (BOKU), 1190 Vienna, Austria

[2] Commision for Glaciology, Bavarian Academy of Sciences and Humanities, 80539 Munich, Germany

Correspondence to: Matthias Bernhardt (matthias.bernhardt@boku.ac.at)

Abstract

Knowledge about the current snow cover extent is essential for characterizing energy and moisture fluxes at the earth surface. The snow-covered area (SCA) is often estimated by using optical satellite information in combination with the normalized-difference snow index (NDSI).The NDSI thereby uses a threshold for the definition if a satellite pixel is assumed to be snow-covered or snow-free. The spatiotemporal representativeness of the standard threshold of 0.4 is however questionable at the local scale. Here, we use local snow cover maps derived from ground-based photography to continuously calibrate the NDSI threshold values ($NDSI_{thr}$) of Landsat satellite images at two European mountain sites of the period from 2010 to 2015. Both sites, the Research Catchment Zugspitzplatt (RCZ, Germany) and the Vernagtferner area (VF, Austria), are located within a single Landsat scene. Nevertheless, the long-term analysis of the $NDSI_{thr}$ demonstrated that the $NDSI_{thr}$ at these sites are not correlated and different to the standard threshold of 0.4. For further comparison, a dynamic and locally optimized NDSI threshold was used as well as another literature threshold value. It was shown that large uncertainties in the prediction of the SCA of up to 24.1 % exist in satellite snow cover maps in case the standard threshold of 0.4 is used, but a newly developed calibrated quadratic polynomial model which is accounting for seasonal threshold dynamics can reduce this error. The model minimizes the SCA

uncertainties at the calibration site VF by 50 % in the evaluation period and was also able to improve the results at RCZ in a significant way. Additionally, a scaling experiment has shown that the positive effect of a locally adapted threshold diminishes from a pixel size of 500 m and more which underlines the general applicability of the standard threshold at larger scales.

1 Introduction

Numerous studies ranging from the local to the global scale have underlined the influence of snow cover on e.g. air temperature, runoff generation, soil temperature and soil moisture (Bernhardt et al., 2012; Deb et al., 2015; Dutra et al., 2012; Dyurgerov, 2003; Liston, 2004; Mankin and Diffenbaugh, 2015; Santini and di Paola, 2015; Tennant et al., 2015). Hence, an accurate estimation of the spatial extent of the snowpack is fundamental for a suite of applications (Pomeroy et al., 2015). The accuracy of weather and climate models heavily depends on this information, as the range of surface temperatures is instantly limited to a maximum of 0° C in existence of snow and the surface albedo becomes typically significantly enhanced (Agosta et al., 2015; Liston, 2004; Rangwala et al., 2010; Takata et al., 2003; Vavrus et al., 2011). From a hydrological point of view, the formation of a snowpack has a buffering effect and thus often leads to a transfer of precipitation water from the cold to the warm season of the year (Bernhardt et al., 2014; Viviroli et al., 2011). This leads to a support of summer runoff needed e.g. in agriculture or for sanitary water supply, but can also lead to an intensification of flood events e.g. in case of rain on snow events (Viviroli et al., 2011). With this in mind, information on the current snow distribution is elementary for water resources management (Thirel et al., 2013) and weather forecasting model systems (Dee et al. 2011).

Snow cover distribution is often derived from satellite data and then either used as input for operational models (Butt and Bilal, 2011; Dee et al., 2011; Homan et al., 2011; Tekeli et al., 2005) or for the offline evaluation of modelled snow cover (Bernhardt and Schulz, 2010; Warscher et al., 2013) and snowfall patterns (Maussion et al., 2011).

The used snow-cover mapping approaches can be grouped into three categories: manual interpretation, classification-based, and index-based methods. Manual classification as well as classification-based approaches are often used in local snow cover mapping studies. Both are out of the scope of this study

as a need for expert knowledge and a high time-demand limit their applicability for large time series data. Hence, we focus on the automatic normalized-difference snow index (NDSI) approach. It was developed by Dozier (1989) and is an established method to identify snow cover in optical satellite images. NOAA/NESDIS which is assimilated into ERA/Interim (Dee et al., 2011; Drusch et al., 2004), or the widely used MODIS snow cover products (Hall and Riggs, 2007; Hall et al., 2002) make use of the NDSI.

The NDSI traces back to band rationing techniques (Kyle et al., 1978; Dozier, 1984) related to the NDVI (Rouse et al., 1974; Tucker, 1979) and is based on the physical principle that snow reflection is significantly higher in the visible range of the spectrum than in mid-infrared. The index ranges between -1 and 1 and a differentiation between snow and no snow is based on a NDSI threshold value ($NDSI_{thr}$) which is commonly assumed to be 0.4 (Dozier, 1989; Hall and Riggs, 2007; Sankey et al., 2015). According to Hall et al. (2001) the accuracy for monthly snow detection using the MODIS product with its standard threshold is about 95 % in non-forested and about 85 % in forested areas. Accuracies in this range make NDSI based snow cover products well accepted for global scale applications, but uncertainties have to be expected at the local scale (Härer et al. 2016).

In this context, numerous recent studies have questioned the general applicability of a standard $NDSI_{thr}$ in local snow and glacier monitoring. When calibrating the $NDSI_{thr}$ manually or by automated methods against field data for single scenes, large deviations from the standard value of 0.4 have been observed. The published values range from 0.18 to 0.7 (Burns and Nolin, 2014; Härer et al., 2016; Maher et al., 2012; Racoviteanu et al., 2009; Silverio and Jaquet, 2009; Yin et al., 2013). The wide range of values show the spatio-temporal variability of the $NDSI_{thr}$ and raise the question for a valid non-subjective method to define this value.

Maher et al. (2012), for example, assumed a spatially calibrated $NDSI_{thr}$ of 0.7 to be constant over time. The comprehensive work of Yin et al. (2013) compared various automatic entropy-based, clustering-based, and spatial threshold methods to adjust the $NDSI_{thr}$ for specific satellite images. The findings of Yin et al. (2013) are based on single-date comparisons at five sites around the world and were undertaken on a regional scale. The clustering-based image segmentation method developed by Otsu (1979)

compared best to the evaluation data sets, which is why the Otsu method is used as comparative data in here.

Härer et al. (2016) have presented a calibration strategy for satellite-derived snow cover maps on the basis of local camera systems. The achieved results have shown that $NDSI_{thr}$ can be distinctly different in course of the snow cover period and that there is a need for a temporal adaption of $NDSI_{thr}$ for achieving valid results in view of the local SCA.

The aim of the presented study is to evaluate the variability of $NDSI_{thr}$ in space and time and to test if this variability does lead to significant uncertainties in the existing snow cover maps. A scaling exercise which has investigated up to which scale a locally adapted threshold can improve the classification results shows the limits of the fixed threshold approach at the local scale.

We use the camera-based calibration approach (Härer et al., 2013) as a reference as it has shown its low error margins in comparison to high resolution locally derived 1m resolution snow maps at RCZ (Härer et al. 2016). The results achieved by this approach are then compared to the automatic segmentation method of Otsu (1979), which has proven to be one of the most performant snow detection methods available today (Yin et al., 2013) and to the standard threshold of 0.4, as well as to a location-specific threshold of 0.7 (Maher et al., 2012). The results will reveal the performance of the different approaches and will clarify for which scales a fixed NDSI threshold can be an adequate solution.

2 Study Site and Data

The presented study focuses on two mountain sites in the European Alps, the Research Catchment Zugspitzplatt (RCZ) located in Germany (47°40’ N/11°00’ E; Bernhardt et al., 2015; Weber et al., 2016) and the Vernagtferner (VF) catchment in Austria (46°52’ N/10°49’ E; figs. 2.4-1a to c; Abermann et al., 2011). RCZ is a partly glaciated headwater catchment with a spatial extent of about 13.1 km². It stretches from 1371 to 2962 m a.s.l. and is mainly built up by limestone. VF is also an alpine headwater basin with a size of 11.5 km² and a glaciated part of about 7.9 km² (Mayr et al., 2013). It ranges from 2642 to 3619 m a.s.l. and the pending rock is gneiss.

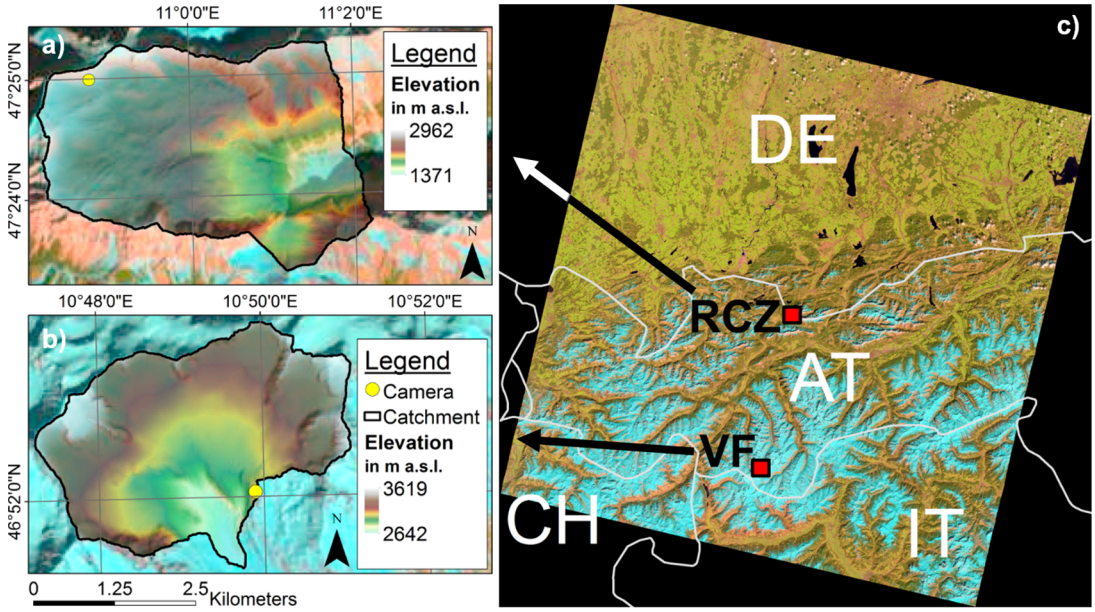

Figure 2.4-1: The figure shows the two test sites used in this study as well as their location within a Landsat scene. Both have indicated the camera location in yellow, the catchment area outlined in black and the digital elevation model (DEM) superimposed on a Landsat Look image. (a) Research Catchment Zugspitzplatt (Germany), (b) Vernagtferner catchment (Austria), (c) Landsat scene (Landsat Look image, WRS2 path 193, row 27) which contains both sites.

Both sites are equipped with similar single lens reflex camera systems for monitoring wide parts of the catchments starting from May 2011 at RCZ and from August 2010 at VF. The camera locations at the study sites are depicted in figs. 2.4-1a and b and the camera orientations are Southwest at RCZ and West-Northwest at VF. Both investigation areas are located within a single Landsat scene (fig. 2.4-1c) which guarantees for comparable illumination conditions and allows for a direct comparison of the $NDSI_{thr}$ between both sites.

Overall, 156 Landsat scenes from Landsat 5 TM, 7 ETM+ and 8 OLI were available for the observation period between 18 August 2010 and 31 December 2015. Suitable satellite image-photograph pairs were available at 15 dates for RCZ and VF, at one date for RCZ and in 32 cases for VF only. The differences stem from the local weather conditions, from the different lengths of the local photograph time series, and from the restriction that a $NDSI_{thr}$ calibration with PRACTISE or the clustering-based image segmentation from Otsu (1979) can only be applied if there is no full snow coverage in the area.

For the photo rectification part in our study, digital elevation models (DEM) with a horizontal resolution of 1 m of RCZ and VF are used, as well as orthophotos with a sub-meter spatial resolution and topographic maps as additional material to ensure an optimal geometric accuracy.

3 Methods

Our study investigates the differences of automatically derived $NDSI_{thr}$ from a) Landsat satellite imagery and b) terrestrial photography with literature values and displays their effects on the resulting snow cover maps.

Radiometrically and geometrically corrected Landsat Level 1 data was used in combination with the cloud and shadow masking software Fmask of Zhu et al. (2015). Any pixel with a cloud probability exceeding 95 % in this analysis was excluded with a surrounding buffer of three pixels (Härer et al., 2016). No atmospheric correction is applied to the Landsat data to facilitate a direct comparison to the majority of studies that apply the NDSI for snow cover mapping (Bernhardt and Schulz, 2010; Maussion et al., 2011; Maher et al., 2012; Warscher et al., 2013; Sankey et al., 2015).

The normalized-difference snow index (NDSI) is calculated in accordance to Dozier (1989) by using green (GREEN, ~0.55 µm) and mid-infrared (MIR, ~1.6 µm) reflectance values:

$$NDSI = \frac{GREEN - \mathrm{MIR}}{GREEN + \mathrm{MIR}}, \tag{2.4-1}$$

NDSI values can range between -1 and 1 and the $NDSI_{thr}$ defines the NDSI value from which on the satellite pixel is assumed as snow-covered. We used fixed $NDSI_{thr}$ values and dynamically derived $NDSI_{thr}$ values in course of this. In case of the fixed values, the standard of 0.4 and a literature value of 0.7 (Maher et al., 2012) were used. For the dynamic approaches, the clustering-based image segmentation approach from Otsu (1979) and a terrestrial camera-based calibration approach of Härer et al. (2016) were applied.

By using Otsu (1979), the $NDSI_{thr}$ is calibrated by maximizing the between-class variance of the two classes snow and no snow:

$$\max_{-1 \leq NDSI_{thr} \leq 1} \{\sigma_O^2\} = \max_{-1 \leq NDSI_{thr} \leq 1} \{P_s(NDSI_{thr})\, P_{ns}(NDSI_{thr})\, [\mu_s(NDSI_{thr}) - \mu_{ns}(NDSI_{thr})]\} \quad (2.4\text{-}2)$$

where P_s and P_{ns} are the probabilities of the classes snow and no snow with respect to the $NDSI_{thr}$, and μ_s and μ_{ns} are the mean values of these two classes. The probability of P_s is thereby calculated as the number of pixels with NDSI values above the $NDSI_{thr}$ divided through the total number of pixels in the image. P_{ns} calculates the absolute difference of P_s to 1.

It has to be mentioned that we restrict the satellite image area used for deriving $NDSI_{thr}$ in accordance to Otsu (1979) to the catchment area of RCZ and VF to allow for a spatio-temporal variable NDSI threshold value within the investigated satellite scenes and to allow for a direct comparison of the locally derived thresholds.

The second dynamic method to calibrate the $NDSI_{thr}$ of the Landsat data for RCZ and VF uses ground-based photographs as baseline.

The Matlab software PRACTISE (version 2.1; Härer et al., 2013 and 2016) is utilized first to georectify the available terrestrial photographs and secondly to calibrate the $NDSI_{thr}$. For doing so, overlapping areas in the photograph-satellite image pairs are used. For further understanding, fig. 2.4-2 gives an overview of the needed input, the internal processing steps and the generated output data of PRACTISE 2.1. The first program part georectifies the photographs and differences between areas with and without snow. This results in a high resolution photography-based snow cover map (fig. 2.4-2, left column). The second part calibrates the $NDSI_{thr}$ for the satellite scene of interest and uses the achieved value to calculate a NDSI based satellite snow cover map (fig. 2.4-2, right column).

The photo georectification is based on the assumption that the recorded two-dimensional photograph (fig. 2.4-3, blue colour) is geometrically connected to the three-dimensional real world (fig. 2.4-3, black colour). Knowing the camera type, its lens and sensor system, as well as the camera location and orientation, a georectification becomes possible if a high-resolution digital elevation model (DEM) is available as well.

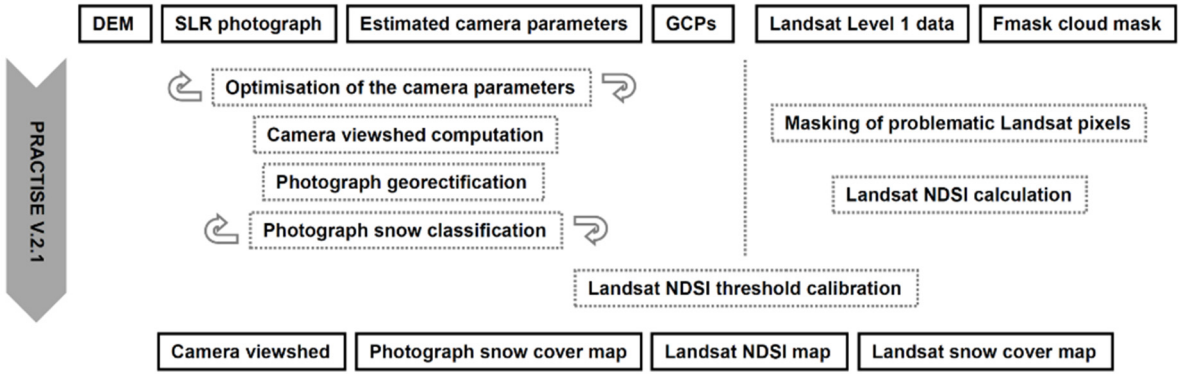

Figure 2.4-2: Input and output data as well as the workflow of PRACTISE (version 2.1) to generate the calibrated NDSI snow cover maps from Landsat data are depicted here (from Härer et al., 2016).

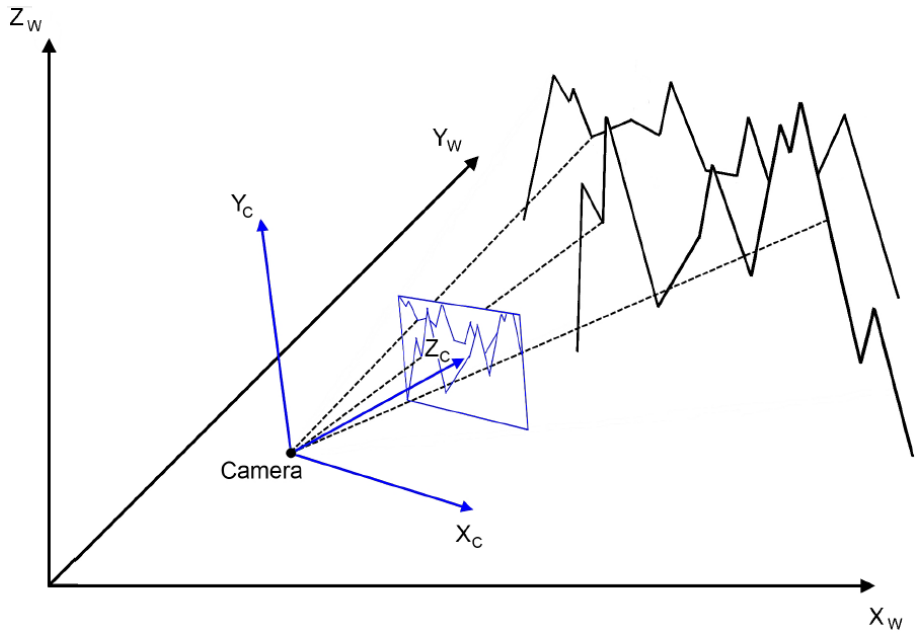

Figure 2.4-3: Schematic relationship between the camera location and orientation, and the two-dimensional photograph (blue) and the three-dimensional real world (black).

Having this theoretical background in mind, we outline the single processing steps for a photograph and a Landsat 7 scene of VF on 17 November 2011 (figs. 2.4-4a to e, 2.4-5a to c).

Before the PRACTISE program is used, any possible distortion effects of the photograph caused by the camera lens are removed by utilizing the freely available Darktable software (http://www.darktable.org/)

and LensFun parameters (http://lensfun.sourceforge.net/). Now that all data is available and ready, the PRACTISE program evaluation can start.

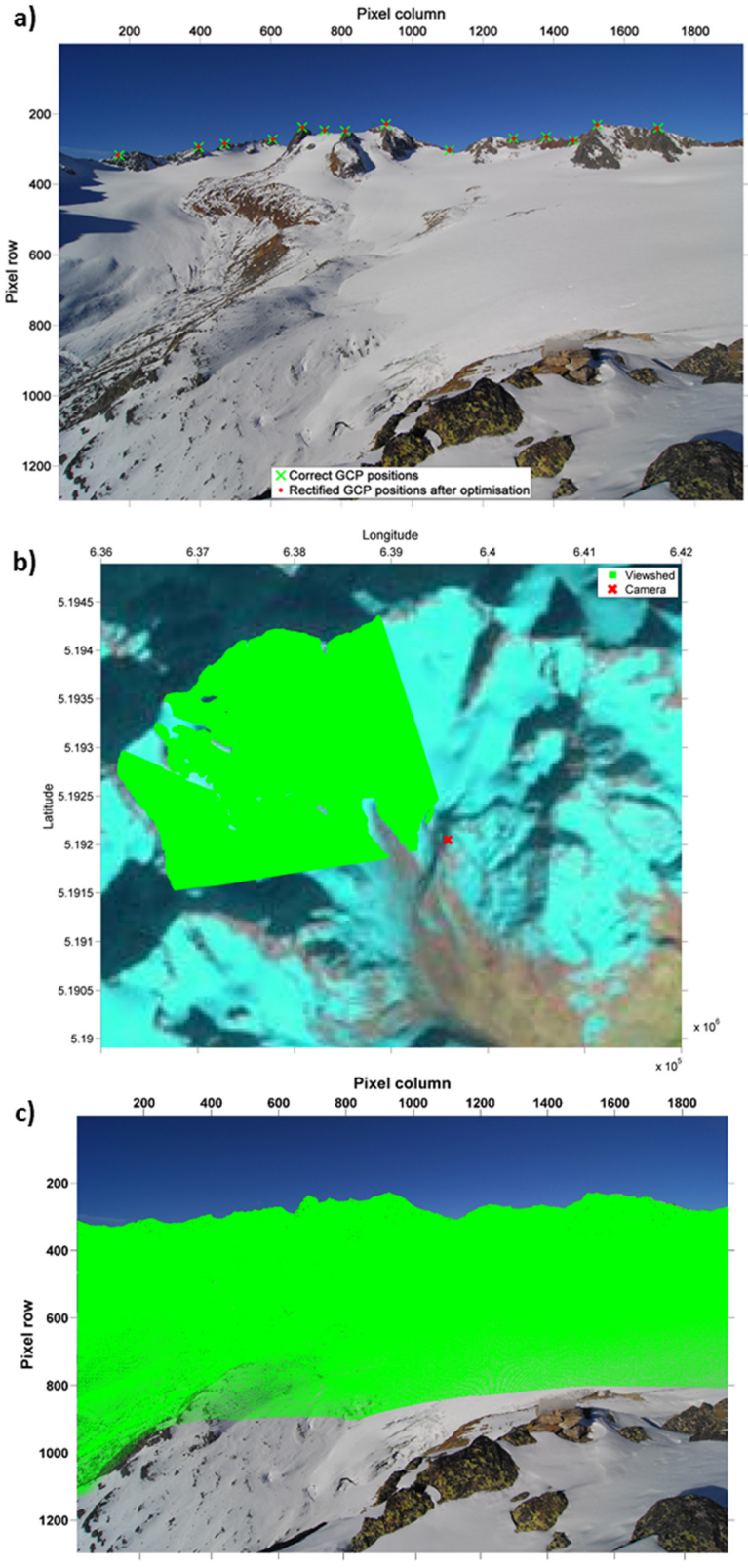

Note: Please turn over for figs. 2.4-4c and d and the figure caption.

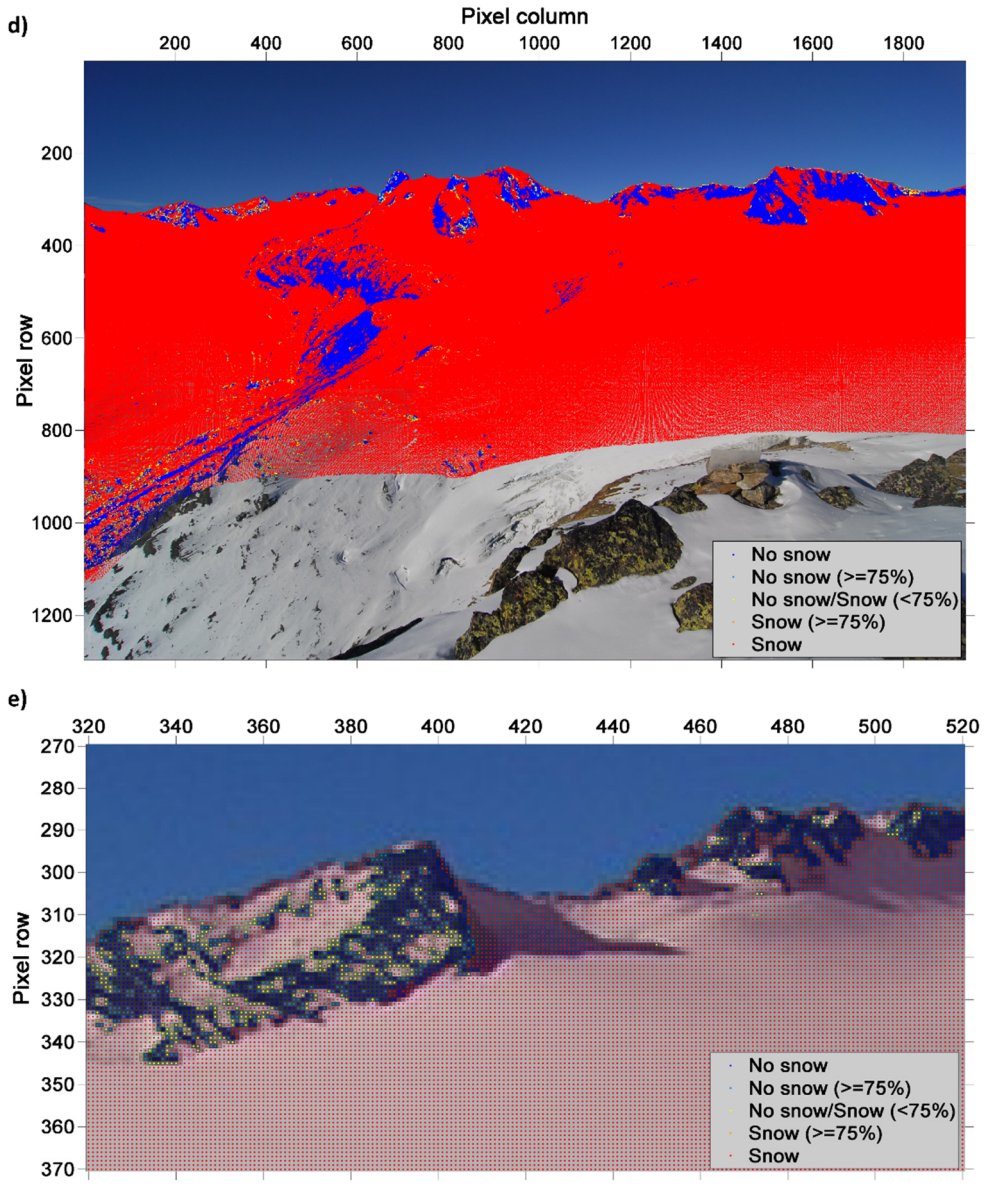

Figure 2.4-4: Internal processing steps within a single PRACTISE evaluation are shown for a photograph of VF on 17 November 2011. The figures chronologically show the routines for the photograph processing in PRACTISE which are (a) the optimization of the camera location and orientation using ground control points, (b) the performed viewshed analysis from the resulting camera location and orientation, (c) the projection and (d) the classification of visible DEM pixels. More detail of the PCA based classification result in (d) can be seen in an enlarged view in (e).

In a first step information about the camera location and orientation is needed for a georectification of the photography. This information is automatically optimized by using ground control points (GCPs, fig. 2.4-4a). The calculated viewpoint and viewing direction are by default used to perform a viewshed analysis (fig. 2.4-4b). The viewshed is needed for an identification of areas which are visible from the

viewpoint and which are not obscured by topographical features or within a user-specified buffer area around the camera. The respective DEM pixels are then projected to the photo plane (fig. 2.4-4c).

Now, the snow classification module is activated to distinguish between snow-covered and snow-free DEM pixels (fig. 2.4-4d). Two major procedures are available for classification. A statistical analysis which is using the blue RGB band (Salvatori et al. 2011) and a principal component analysis (PCA) based approach (Härer et al. 2016). The first is used for shadow-free scenes, the second for scenes with shaded areas. Härer et al. (2013) and (2016) give more insights into the used classification algorithms and their performance as well as on a third manual option if none of the two classification routines can be applied successfully. The used snow cover maps do have less than 5 % misclassified pixels, which was proven by visual inspection. For this example photograph, the snow classification algorithm utilizing a principal component analysis (PCA) was selected to account for the shadow-affected areas in the upper left part of the photograph (fig. 2.4-4d, enlarged view in fig. 2.4-4e).

After the photograph rectification and classification, the remote sensing routine of PRACTISE begins with the identification of satellite pixels that spatially overlap with the photograph snow cover map. It also generates a cloud- and shadow-free satellite image by using fmask (Zhu et al., 2015). The needed NDSI map is calculated in accordance with eq. (2.4-1) by PRACTISE (fig. 2.4-5a).

If both, the NDSI satellite map and the corresponding high-resolution photograph snow cover map were processed, an iterative calibration of the NDSI threshold value is started to acquire the best agreement between the local scale (photograph) and the large scale (Landsat) snow cover map by maximizing the ratio of identically classified pixels to the overall number of photograph-satellite image pixel pairs n (Aronica et al., 2002):

$$F = \frac{(a+d)}{n}, \tag{2.4-3}$$

a thereby represents the number of correctly identified snow pixels and *d* the same for no snow pixels. *F* is between 0 and 1 and becomes 1 for a perfect agreement between the two images.

Figure 2.4-5b shows the resulting satellite snow cover map superimposed on the photograph snow cover map and a Landsat Look image. A cutout is shown for more detail in fig. 2.4-5c.

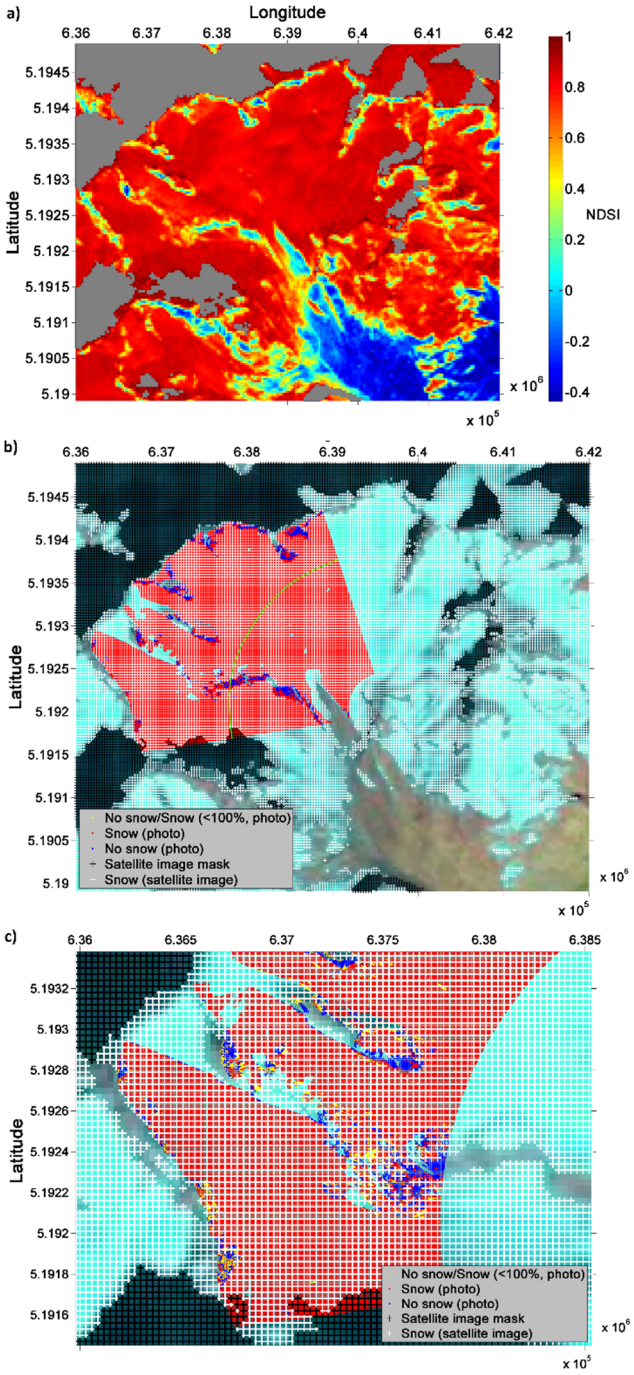

Figure 2.4-5: We outline here the internal processing steps within the remote sensing routines of PRACTISE. The Landsat NDSI map from 17 November 2011 is shown in (a). Clouds and shadows (grey areas) are excluded using fmask. The photograph and satellite snow cover map derived from the PRACTISE evaluation are superimposed on the Landsat Look image of 17 November 2011 in (b). Snow is depicted in red for the photograph snow map and white for the satellite snow map. The lower areas at VF (south-east of the green line in (b)) were excluded from the complete analysis as the combination of strong glacier retreat at VF and temporal difference between some analysis dates and the DEM recording dates resulted in a discrepancy of real elevations and DEM in the lower catchment areas that affected $NDSI_{thr}$ calibration results. The cutout in (c) clarifies which photographed areas are part of the analysis and additionally underlines the high agreement between photograph and satellite snow cover map.

It has to be mentioned that the glacier retreat between DEM production years (2007, 2010) and analysis period 2010-2015 has resulted in a discrepancy between real world elevations and the available DEMs, especially in the last years of the observation period. Figure 6 exemplarily depicts the glacier retreat between 2007 and 2010 by superimposing the ice mass loss on an orthophoto of VF from 2010.

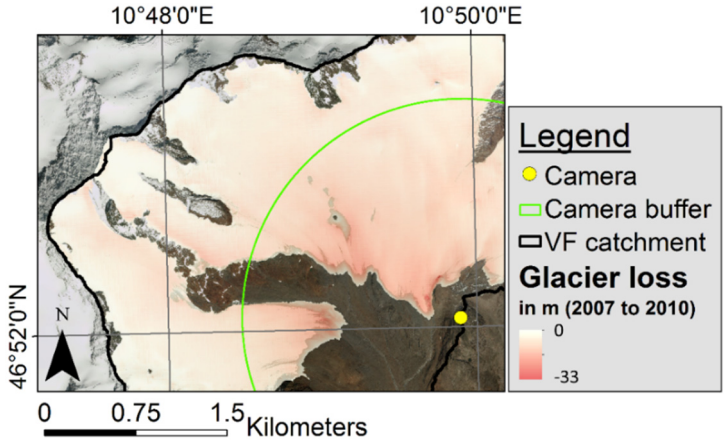

Figure 2.4-6: Glacier retreat from 2007 to 2010 causes a loss in elevation of up to -33 m at VF. The green line depicts the buffer distance around the camera which was excluded from the analysis due to significant glacier loss which in turn lead to geometric inaccuracies in the photograph rectification and incorrect NDSI threshold calibration results.

This loss in elevation leads to inaccuracies in the georectification results of the photographs. And a test for the photograph of 28 August 2010 applying the DEM of 2007 and 2010 showed that these georectification issues, in turn, affect the $NDSI_{thr}$ calibration results. For the DEM from 2007, the calibrated $NDSI_{thr}$ is 0.47 while the correct threshold for the up-to-date DEM from 2010 is 0.52. As a consequence, we limited the analysis to higher elevated and thus colder areas of the catchment where glacier retreat is marginal (areas north-west of the green line in figs. 2.4-5b and 2.4-6).

To ensure that reducing the spatial overlap between photograph snow cover map and NDSI satellite map does not have any negative effect on the calibrated $NDSI_{thr}$, we firstly calibrated the $NDSI_{thr}$ for the three investigated Landsat scenes in 2010 for the complete and the upper area only. Moreover, we calibrated the $NDSI_{thr}$ for the 44 remaining scenes between 2011 and 2015 using the upper area DEM from 2007 and 2010 to test for a $NDSI_{thr}$ sensitivity in the longer time series. For both approaches, the differences between the calibrated $NDSI_{thr}$ never become larger than 0.01. Hence, we assume that our

calibration approach of using the higher elevated areas at VF which is incorporated in PRACTISE by excluding a radius of 1800 m around the camera from the analysis (green line in figs. 2.4-5b and 2.4-6) is valid for the complete analysed time series between 2010 and 2015.

We did not find a similar effect on the $NDSI_{thr}$ calibration in our tests at RCZ. Hence, there was no need to remove the glacier areas at RCZ from the analysis.

4 Results and Discussion

The NDSI thresholds derived by the two dynamic methods are now discussed and related to static thresholds.

The $NDSI_{thr}$ predicted by the Otsu method are densely grouped around 0.4. This is underlined by a mean of 0.36 and a standard deviation of 0.04 at RCZ and a mean of 0.41 with a corresponding standard derivation of 0.04 at VF (table 2.4-1). The statistics do not include two dates at VF as no separating $NDSI_{thr}$ could be found by using the Otsu method here (squares in fig. 2.4-7a).

Table 2.4-1: Basic statistic measures of the automatically derived NDSI threshold time series at RCZ and VF using the Otsu segmentation method and the camera-based calibration method.

Site	Automatically derived NDSI threshold values									
	Mean		Standard Deviation		Max		Min		Spread	
	camera	Otsu	camera	Otsu	camera	Otsu	camera	Otsu	camera	Otsu
RCZ	0.28	0.36	0.07	0.04	0.39	0.45	0.15	0.29	0.24	0.16
VF	0.57	0.41	0.09	0.04	0.74	0.47	0.35	0.33	0.39	0.14

This stands in contradiction to the real situation as the photographs do show that there was no full snow coverage at the respective dates which would generally allow for a prediction of $NDSI_{thr}$. This shows that the application of the Otsu method is potentionally uncertain in nearly fully snow-covered situations. Furthermore, a tendency to slightly higher mean $NDSI_{thr}$ at VF and slightly lower thresholds at RCZ could be detected and the very small observed differences to the standard of 0.4 would not underline the need for a location-dependent threshold prediction. Additionaly, the weak seasonal dynamics which can be found at VF would also not require a time-dependent calculation of the threshold.

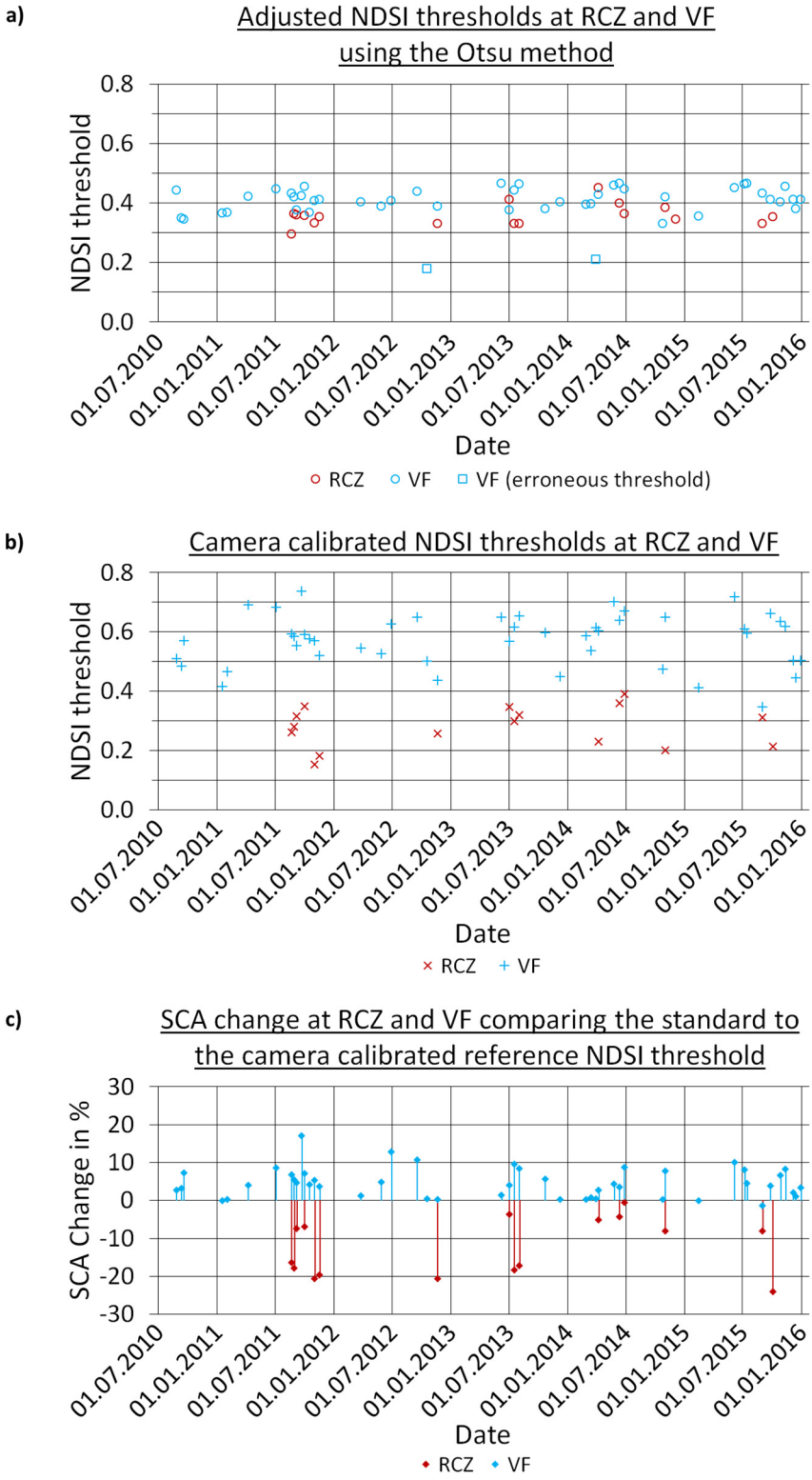

Figure 2.4-7: The figure displays in (a) the complete time series of adjusted NDSI thresholds using the Otsu segmentation method (circles, erroneous thresholds as squares) at RCZ (red) and VF (blue) and depicts in (b) the camera calibrated NDSI thresholds at these two sites utilizing ground-based photographs as in situ measurements (blue pluses for VF and red crosses for RCZ). Relative SCA changes at RCZ and VF resulting from the application of the standard instead of the camera calibrated reference NDSI threshold are shown in (c).

The camera-based method leads in general to a more dynamic $NDSI_{thr}$ in time and to a higher systematic difference of $NDSI_{thr}$ between the two sites. The archived 16 $NDSI_{thr}$ at RCZ and 47 $NDSI_{thr}$ at VF are compared in a first step. The presumption of a comparable $NDSI_{thr}$ for both sites could not be confirmed in this case. Significant differences were detected despite the fact that both sites are high alpine and are located within a single Landsat scene. Moreover, the calibrated $NDSI_{thr}$ were in large parts significantly different to the standard value of 0.4. Figure 2.4-7b and table 2.4-1 illustrate the variability and the range of $NDSI_{thr}$ at both sites. The minimum value at RCZ is 0.15 while the maximum value is 0.39. The values at VF are in general on a higher level and range between 0.35 and 0.74. Both sites thus strongly scatter around their catchment-specific mean value (0.28 at RCZ, 0.57 at VF) but show a characteristic development over the year (fig. 2.4-9) which is also detected in a significantly weaker form for the Otsu method at VF. Independent of the fact that this seasonal dynamic is comparable for both sites using the camera-based method. fig. 2.4-7b highlights that the correlation coefficient between $NDSI_{thr}$ at RCZ and VF is very low when they are compared on a date by date basis (r = 0.17). By contrast, a correlation between the Otsu method and the terrestrial camera-based method at VF of -0.56 is found which however cannot be observed at RCZ between the two methods (r = 0.10, figs. 2.4-7a and b).

The results of the camera-based methods require a deeper investigation to analyse if such different $NDSI_{thr}$ are justifiable. Despite the strong scatter and the resulting low correlation, the differences in the catchment-specific mean $NDSI_{thr}$ levels seem to be systematic (table 2.4-1). Topographic characteristics could be a possible reason. These are similar with respect to elevation, slope and aspect but different for the pending rock being limestone at RCZ and gneiss at VF. We hence investigated the NDSI reflectance values for the snow-free bare rock areas within each catchment. This is valid for the complete time series as the steepest almost vertical rock faces in the catchment are snow-free in all used scenes. Figure 2.4-8 presents frequency histograms of these NDSI reflectances for five summer dates. Other seasons were excluded due to the increased probability of fractional snow cover in the Landsat pixels. The tests show that the maximum frequencies after smoothing the histogram are stable for these dates for each catchment. The mean maximum frequency is about -0.34 at RCZ and 0.01 at VF. The mean NDSI reflectance difference of the rocks at RCZ and VF amounts to about 0.34. This difference

is comparable to the mean systematic difference of 0.26 found for the mean calibrated $NDSI_{thr}$ at both sites. It is therefore probable that the different rock types and therewith the background radiation triggers the catchment-specific mean $NDSI_{thr}$ levels which in turn supports the idea of adapting $NDSI_{thr}$ locally.

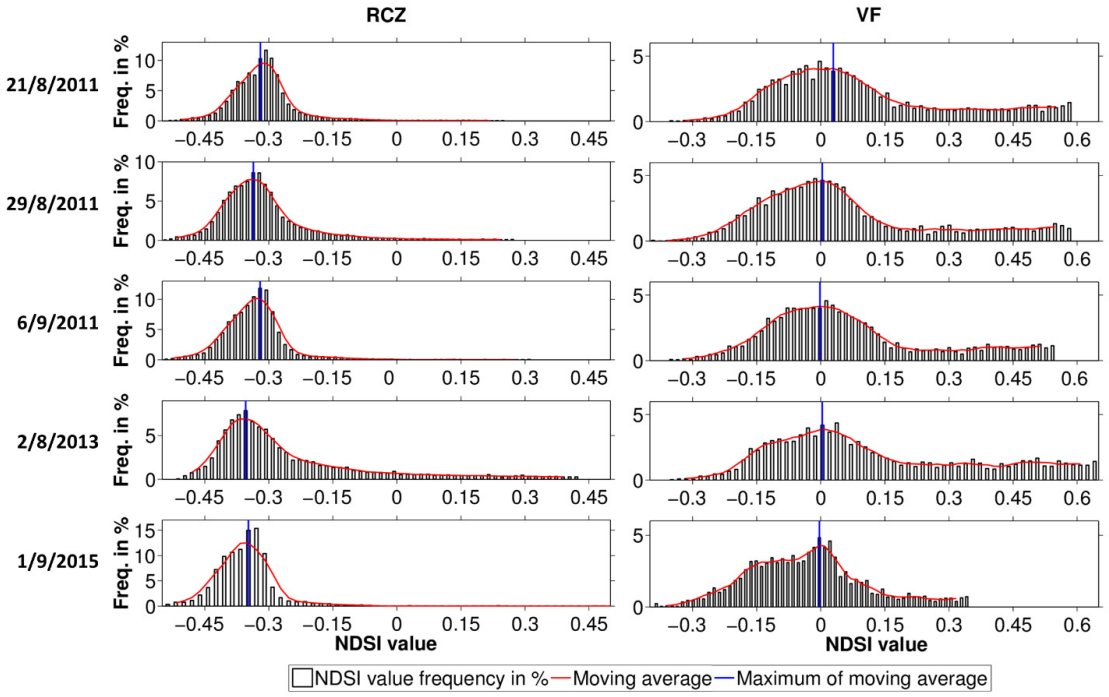

Figure 2.4-8: Representative NDSI reflectance values for the rock surfaces in RCZ and VF catchment are determined using frequency histograms of the snow-free bare rock NDSI values for five summer dates. These are then smoothed applying a moving average of 5 histogram classes. The maxima of the smoothed histograms are stable for each catchment and the investigated dates and result in mean NDSI values for rock surfaces at RCZ of -0.34 and at VF of 0.01.

Next, the effect of the calibrated $NDSI_{thr}$ on the predicted snow-covered area (SCA) at RCZ and VF is analysed. The differences between the SCA predicted with the standard threshold of 0.4 and with the Otsu method are in principle small. This can be related to the minor differences between standard $NDSI_{thr}$and the threshold predicted over Otsu. The absolute differences are 0.05 km² in average for VF and 0.15 km² for RCZ. The effects achieved with the photographic method instead are on a level which questions the applicability of the standard threshold for local investigations. The differences in SCA ($SCA_{diff\%}$) inbetween the products using the Otsu calibrated $NDSI_{thr}$ (SCA_{otsu}) and the standard threshold of 0.4 ($SCA_{0.4}$) are calculated using the camera-calibrated SCA (SCA_{cam}) as baseline which

has shown the highest accuracy of the derived snow cover products when compared to the available photo classifications of PRACTISE (Härer et al., 2016):

$$SCA_{diff\%,\mathrm{otsu}} = \frac{100\ (SCA_{\mathrm{otsu}} - SCA_{cam})}{SCA_{cam}} \tag{2.4-3}$$

For calculating $SCA_{diff\%,0.4}$, SCA_{otsu} has to be replaced by $SCA_{0.4}$.

The values are between -24.1 % at RCZ and +17.2 % at VF (fig. 2.4-7c) and reveal how much uncertainty currently exists in NDSI based snow cover maps on the small scale. The deviations are in general larger at RCZ where the calibrated NDSI threshold values are mainly below 0.4. This means that the SCA is systematically underestimated when using the standard of 0.4. The lower error in percents at VF compared to the error percentages at RCZ can be related to the generally higher snow-covered area in the VF catchment. These relative differences result in turn in significantly different absolute SCA (standard threshold versus calibrated threshold). Here, the highest differences are 1.09 km² at RCZ and 1.67 km² at VF. This is a relevant error margin especially if the small catchment sizes of only 13.1 km² (RCZ) and 11.5 km² (VF) are taken into account.

Given this finding and the large variability observed in calibrated $NDSI_{thr}$ it is obvious that widely used methods (e.g. Maher et al., 2012) which locally calibrate the $NDSI_{thr}$ for a single date and then apply this threshold at multiple dates are also no solution and can even deteriorate the accuracy compared to the standard threshold method. An example is the application of a calibrated threshold of 0.7 at VF to the complete time series in this catchment. This results in a mean absolute error in SCA of 1.26 km² compared to an average deviation of 0.41 km² for the standard threshold method.

An alternative to the temporally constant threshold methods is a statistical modelling approach fitted to the calibrated $NDSI_{thr}$. This however requires a solid set of calibration data to adjust the model to the observations at multiple dates. VF hence serves as an example for this approach because of its higher data availability. As stated before a seasonal dynamic in the calibrated $NDSI_{thr}$ could be observed at both sites. This temporal development is potentially related to the sun angle, snow age, grain size or albedo development or other effects. A detailed investigation of the reasons of this effect is beyond this study but will be subject of future studies.

A quadratic polynomial model was fitted to the calibrated $NDSI_{thr}$ for the years 2010 to 2013 at VF ($NDSI_{vf}$, fig. 2.4-9). $NDSI_{vf}$ might not exactly reproduce the calibrated thresholds at any time step (r^2=0.45; RMSE=0.06) but the evaluation of this simple model for 2014 and 2015 at VF shows a remarkable reduction in the average SCA error from 0.35 km² when applying the standard threshold of 0.4 down to 0.17 km².

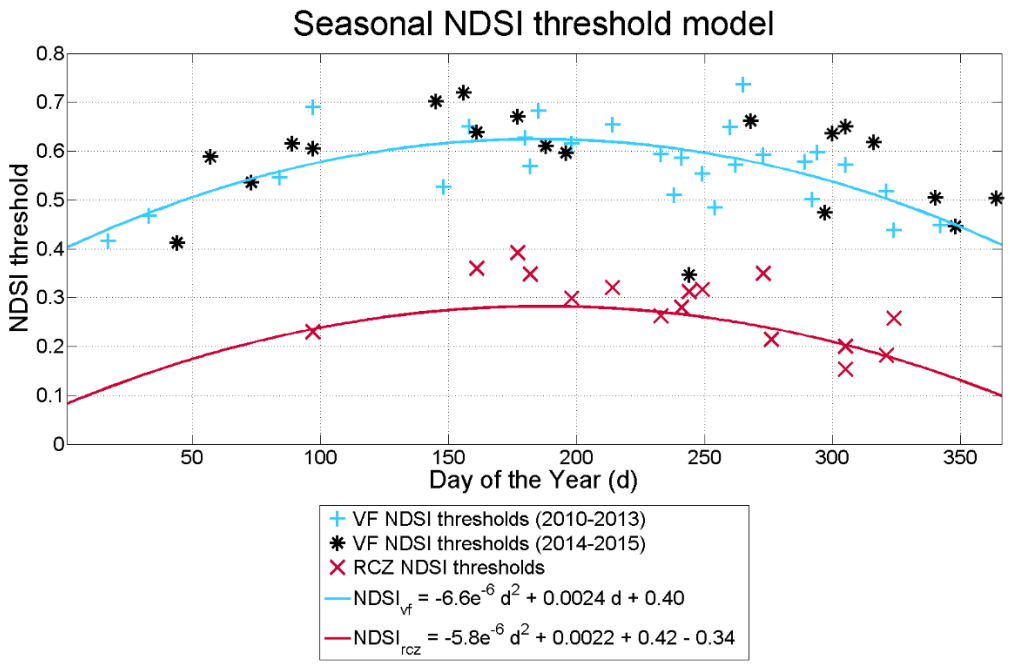

Figure 2.4-9: Estimates of NDSI threshold values at VF are predicted for each day of the year by a quadratic polynomial model ($NDSI_{vf}$, blue line) which was fitted to the calibrated NDSI thresholds between 2010 and 2013 ($NDSI_{thr}$, blue pluses). The coefficient of determination (r^2) of this model is 0.45 and the root mean square error (RMSE) is 0.06. The black stars represent the $NDSI_{thr}$ from 2014 to 2015 at VF used for evaluation of $NDSI_{vf}$. Additionally, a $NDSI_{thr}$ prediction model for RCZ ($NDSI_{rcz}$, red line) is defined by a quadratic polynomial model fitted to the complete time series of calibrated $NDSI_{thr}$ at VF (blue pluses and black stars, r^2=0.36, RMSE=0.07) and an additional term of -0.34 to account for the NDSI reflectance difference between the different rock surfaces at RCZ and VF. $NDSI_{rcz}$ is evaluated against the calibrated $NDSI_{thr}$ of RCZ (red crosses).

As not any site is equipped with camera infrastructure, it was also tested if the achieved regression model can be transferred to RCZ while including information about the geology-dependent offset between the average $NDSI_{thr}$ values. Hence, the model is fitted to the complete calibrated $NDSI_{thr}$ time series at VF (r^2=0.36; RMSE=0.07) and a term for the systematic mean NDSI reflectance difference of the rocks at RCZ and VF is added ($NDSI_{rcz}$, fig. 2.4-8). The evaluation of $NDSI_{rcz}$ seems to slightly underestimate

the calibrated $NDSI_{thr}$ at RCZ. Nevertheless, the quadratic polynomial model accounting for the reflectance differences at different sites results in a significant reduction of snow cover mapping uncertainties of 40 % as the mean SCA error amounts to 0.18 km² while the application of the standard threshold method causes an average deviation in snow cover of 0.31 km² in RCZ. Given the assumption that the seasonal dynamic and the correction factor are generally applicable, the presented seasonal model derived from the multi-year use of PRACTISE at a single site is hence not only temporally but by using information about the spectral properties of the pending rock types without the need for other camera systems also spatially transferrable. This assumption will be further evaluated in future studies with more test sites.

We have now underlined the importance of a locally adapted NDSI threshold calibration for Landsat snow cover maps at the two presented catchments. However, the detected NDSI threshold dependency automatically leads to the question if the need for threshold adaption is also necessary for coarser resolution satellite snow cover maps. This is of special interest as MODIS snow cover products are today the most frequently applied satellite snow cover maps. They are based on the NDSI technique and the 0.4 threshold and have a spatial resolution of 500 m. Hence, we aggregated the Landsat snow cover maps using calibrated and standard NDSI threshold values from 30 m to 90 m, 210 m, 510 m, and 990 m resolution. It can be seen that the SCA deviation between standard and calibrated snow cover maps diminishes for coarser resolution data. Figure 2.4-10a outlines this error reduction with spatial aggregation for a Landsat 7 scene of Vernagtferner catchment on 16 September 2011. Figure 2.4-10b shows the simultaneously captured photograph used for calibration. Figure 2.4-10c underlines this finding by depicting the spatial resolution at which standard and calibrated snow cover maps become identical for the 65 cases investigated in the two catchments.

The aggregation step to 510 m is thereby of major importance as more than 90 % of SCA maps for our investigation period and study become identical at this pixel size. Thus, using the standard threshold of 0.4 seems to be accurate in case of the MODIS snow cover product with a pixel size of 500 m. For applications at this scale, the additional effort using camera calibrated data only provides slight improvements and might rarely justify the effort. However, our new method using camera-calibrated

data allows setting in value the higher resolution satellite data of the Landsat series and of the new Sentinel 2.

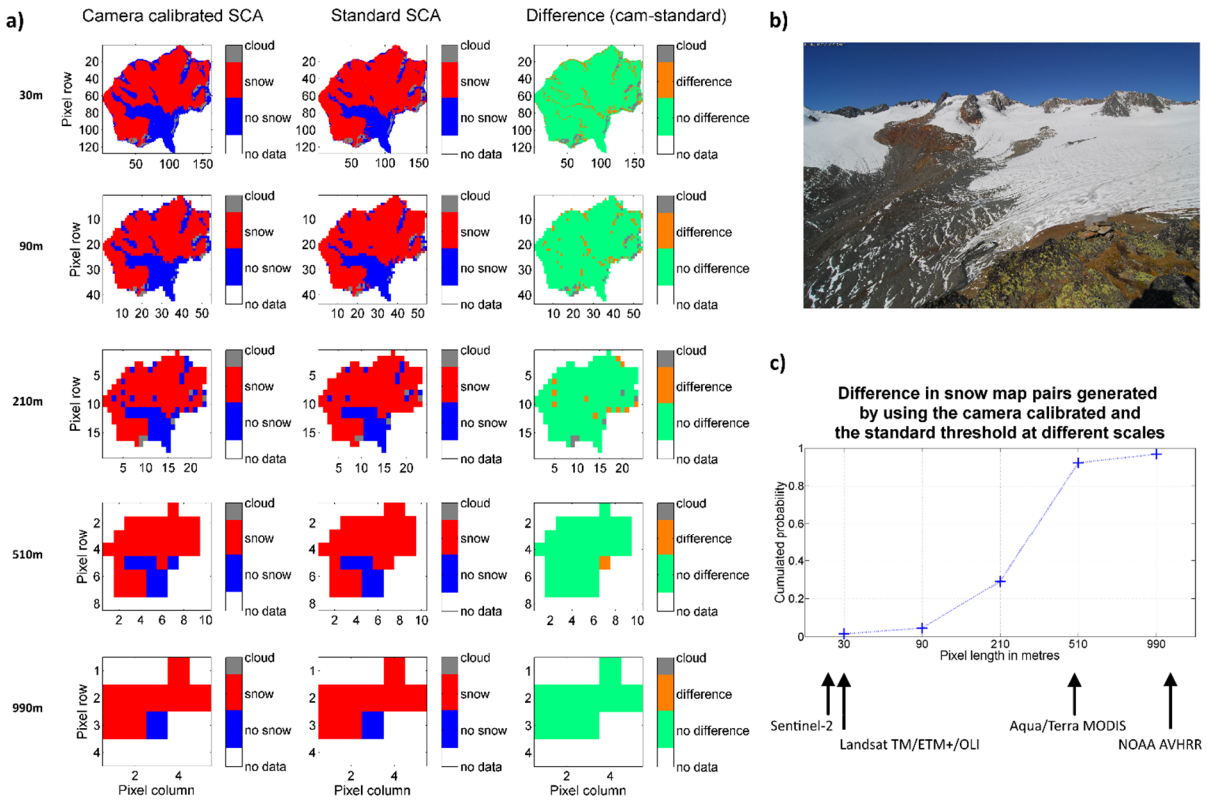

Figure 2.4-10: At VF, we exemplarily show in (a) the effect of scaling to NDSI based snow cover products for a Landsat 7 scene on 16 September 2012. The first column outlines the camera calibrated SCA, in the second column the standard threshold SCA is depicted, and in the third column their differences at VF are presented. The different rows show different scaling factors, starting from the top with the original resolution and a factor of 1 (30 m) to 3 (90 m), 7 (210 m), 17 (510 m) and at the bottom a factor of 33 (990 m). The concurrent photograph in (b) depicts the snow situation at VF in our example. The analysis of all investigation dates in (c) shows that camera calibrated and standard threshold snow cover maps become more and more identical with lower resolutions. The positive effect of the camera calibration for Landsat and presumably Sentinel 2 data thus diminishes for pixel sizes of 500 m and higher and hence for snow cover products derived from the MODIS or the AVHRR sensor.

5 Conclusions

The study has revealed that using the standard threshold of 0.4 is adequate for satellite products with a pixel size of 500 meters and more. For higher resolution snow cover mapping, significant improvements in the quality of the snow cover maps can be achieved if a threshold is used which is variable in space and time. The clustering-based segmentation technique of Otsu is producing results which are only slightly different from those of the standard threshold of 0.4 and do not indicate a need for a further

adaption. However, when compared to local images, the resulting differences are becoming obvious and could only be reduced by the presented camera-based technique. The long-term analysis of calibrated $NDSI_{thr}$ at two comparable high elevation sites has shown that large deviations from the 0.4 standard threshold exist. The calibrated optimal threshold values span a range from 0.15 to 0.74 over the complete time series and can reach a difference of 0.45 between both observation sites at a single date. It was also shown that these differences in $NDSI_{thr}$ lead to significantly different SCA when compared to the standard of 0.4.

The $NDSI_{thr}$ at both sites have similar seasonal dynamics while scattering around different site-specific average values (0.28 at RCZ, 0.57 at VF). The difference between the average threshold values at the two sites could be related to the different reflection properties of the rock types in the investigation areas (limestone at RCZ and gneiss at VF). The overall correlation coefficient between $NDSI_{thr}$ of both sites is low (r = 0.17) which prohibits a date by date transfer of calibrated values from one catchment to the other.

In view of the validity of the standard threshold of 0.4 at the local scale, it was found that relative SCA error margins of up to 24.1 % were found for the standard threshold method when using 30 m Landsat products. This is critical for any snow cover mapping application and especially for model evaluation studies. We hence conclude that the application of a fixed NDSI threshold can lead to large uncertainties in the resulting snow cover products at least at the local scale. Consequently, local studies strongly need to account for the $NDSI_{thr}$ variability in space and time in order to guarantee high accuracy snow cover products. But, in case studies are carried out with sensors having a pixel size of 500 meters and more the advantage of a location-dependent $NDSI_{thr}$ vanishes.

It was shown that site-specific single-date adaptations of the $NDSI_{thr}$ also do not lead to resilient results. The uncertainty introduced by a single measurement is not quantifiable and can lead to results worse than that achieved by using the standard value of 0.4. A quantitative calibration or visual derivation of the $NDSI_{thr}$ for a single date and its application to other dates is therefore jeopardous.

The approximation of the $NDSI_{thr}$ over a simple seasonal model fitted to the calibrated $NDSI_{thr}$ at the respective site has shown improvements instead. The achieved model was able to reduce the error in the

SCA prediction by 50 % when compared to the standard threshold method. Nevertheless, a fundamental data pool of in situ information covering the dynamic over the year as well as the range of possible $NDSI_{thr}$ within a season is needed for calculating this relation. Finally, it was shown that the fitted model parameters are also spatially transferable if an additional term accounts for the background radiation of the different rock types. This is possible without in situ measurements by utilizing the constant NDSI reflectance differences of the rock surface in the respective catchments. However, this needs to be further tested at more sites. Future studies will hence use the existent webcam infrastructure in the European Alps as well as camera systems installed worldwide at the INARCH network sites (Pomeroy et al., 2015) for the generation of numerous calibrated $NDSI_{thr}$. The observed threshold values will serve as operational source for applicable $NDSI_{thr}$ and will allow to evaluate the presented temporally and spatially variable prediction approach of $NDSI_{thr}$. In case of a successful evaluation, the presented scheme allows for an objective and reproducible derivation of the $NDSI_{thr}$ value for any given satellite scene. This is a large advantage as the threshold is up to now often set intuitively or assumed as constant which does neither conform to the complexity of the models evaluated on basis of NDSI based snow cover maps nor to the needs of the models which are assimilating these maps.

Acknowledgements. This work was funded by the Austrian Science Fund (I 2142-N29), the doctoral scholarship program of the German Federal Environmental Foundation (DBU), the Helmholtz Research School Mechanisms and Interactions of Climate Change in Mountain Regions (MICMoR) and has additionally received a fundamental support of the Environmental Research Station Schneefernerhaus (UFS) in course of the Virtual Alpine Observatory (VAO). The Commission for Glaciology of the Bavarian Academy of Sciences and Humanities has kindly provided data of Vernagtferner. We want to thank the crew of the UFS (Markus Neumann, Dr. Till Rehm and Hannes Hiergeist) for supporting this peace of research by hosting the authors and maintaining the camera system. Thomas Werz and Michael Weber have also supported the research by temporally maintaining the camera system. Relevant data can be made available by the authors.

References

Abermann, J., Kuhn, M., and Fischer, A.: A reconstruction of annual mass balances of Austria's glaciers from 1969 to 1998, Ann. Glaciol., 52(59), 127–134, doi:10.3189/172756411799096259, 2011.

Agosta, C., Fettweis, X., and Datta, R.: Evaluation of the CMIP5 models in the aim of regional modelling of the Antarctic surface mass balance, The Cryosphere, 9(6), 2311–2321, doi:10.5194/tc-9-2311-2015, 2015.

Aronica, G., Bates, P. D., and Horritt, M. S.: Assessing the uncertainty in distributed model predictions using observed binary pattern information within GLUE, Hydrol. Process., 16(10), 2001–2016, doi: 10.1002/hyp.398, 2002.

Bernhardt, M., and Schulz, K.: SnowSlide: A simple routine for calculating gravitational snow transport, Geophys. Res. Lett., 37, L11502, doi:10.1029/2010GL043086, 2010.

Bernhardt, M., Schulz, K., and Pomeroy, J.: The International Network for Alpine Research Catchment Hydrology. A new GEWEX crosscutting Project, Hydrol. Wasserbewirts., 59(4), 190–191, 2015.

Bernhardt, M., Schulz, K., Liston, G. E., and Zängl, G.: The influence of lateral snow redistribution processes on snow melt and sublimation in alpine regions, J. Hydrol., 424–425, 196-206, doi:10.1016/j.jhydrol.2012.01.001, 2012.

Bernhardt, M., Härer, S., Jacobeit, J., Wetzel, K. F., and Schulz, K.: The Virtual Alpine Observatory - research focus Alpine hydrology, Hydrol. Wasserbewirts., 58(4), 241–243, 2014.

Burns, P., and Nolin, A.: Using atmospherically-corrected Landsat imagery to measure glacier area change in the Cordillera Blanca, Peru from 1987 to 2010, Remote Sens. Environ., 140, 165–178, doi:10.1016/j.rse.2013.08.026, 2014.

Butt, M. J., and Bilal, M.: Application of snowmelt runoff model for water resource management, Hydrol. Process., 25(24), 3735-3747, doi:10.1002/hyp.8099, 2011.

Deb, D., Butcher, J., and Srinivasan, R.: Projected Hydrologic Changes Under Mid-21st Century Climatic Conditions in a Sub-arctic Watershed, Water Resour. Manag., 29(5), 1467–1487, doi:10.1007/s11269-014-0887-5, 2015.

Dee, D. P., Uppala, S. M., Simmons, A. J., Berrisford, P., Poli, P., Kobayashi, S., Andrae, U., Balmaseda, M. A., Balsamo, G., Bauer, P., Bechtold, P., Beljaars, A. C. M., van de Berg, L., Bidlot, J., Bormann, N., Delsol, C., Dragani, R., Fuentes, M., Geer, A. J., Haimberger, L., Healy, S. B., Hersbach, H., Holm, E. V., Isaksen, L., Kallberg, P., Koehler, M., Matricardi, M., McNally, A. P., Monge-Sanz, B. M., Morcrette, J.-J., Park, B.-K., Peubey, C., de Rosnay, P., Tavolato, C., Thepaut, J.-N., and Vitart, F.: The ERA-Interim reanalysis: configuration and performance of the data assimilation system, Q. J. Roy. Meteor. Soc., 137(656), 553–597, doi:10.1002/qj.828, 2011.

Dozier, J.: Snow reflectance from LANDSAT-4 Thematic Mapper, IEEE Trans. Geosci. Remote Sens., GE-22(3), 323–328, doi:10.1109/TGRS.1984.350628, 1984.

Dozier, J.: Spectral Signature of Alpine Snow Cover from the Landsat Thematic Mapper, Remote Sens. Environ., 28, 9–22, doi:10.1016/0034-4257(89)90101-6, 1989.

Drusch, M., Vasiljevic, D., and Viterbo, P.: ECMWF's global snow analysis: Assessment and revision based on satellite observations, J. Appl. Meteorol., 43(9), 1282–1294, doi:10.1175/1520-0450(2004)043<1282:EGSAAA>2.0.CO;2, 2004.

Dutra, E., Viterbo, P., Miranda, P. M. A., and Balsamo, G.: Complexity of Snow Schemes in a Climate Model and Its Impact on Surface Energy and Hydrology, J. Hydrometeorol., 13(2), 521–538, doi:10.1175/JHM-D-11-072.1, 2012.

Dyurgerov, M.: Mountain and subpolar glaciers show an increase in sensitivity to climate warming and intensification of the water cycle, J. Hydrol., 282(1-4), 164–176, doi:10.1016/S0022-1694(03)00254-3, 2003.

Hall, D. K., and Riggs, G. A.: Accuracy assessment of the MODIS snow products, Hydrol. Process., 21(12), 1534–1547, doi:10.1002/hyp.6715, 2007.

Hall, D. K., Foster, J. L., Salomonson, V. V., Klein, A. G., and Chien, J. Y. L.: Development of a technique to assess snow-cover mapping errors from space, IEEE Transactions on Geoscience and Remote Sensing, 39(2), 432–438, doi: 10.1109/36.905251, 2001.

Hall, D. K., Riggs, G. A., Salomonson, V. V., DiGirolamo, N. E., and Bayr, K. J.: MODIS snow-cover products, Remote Sens. Environ., 83(1-2), 181–194, doi:10.1016/S0034-4257(02)00095-0, 2002.

Härer, S., Bernhardt, M., and Schulz, K.: PRACTISE – Photo Rectification And ClassificaTIon SoftwarE (v.2.1), Geosci. Model Dev., 9(1), 307–321, doi:10.5194/gmd-9-307-2016, 2016.

Härer, S., Bernhardt, M., Corripio, J. G., and Schulz, K.: PRACTISE – Photo Rectification And ClassificaTIon SoftwarE (v.1.0), Geosci. Model Dev., 6(3), 837–848, doi:10.5194/gmd-6-837-2013, 2013.

Homan, J. W., Luce, C. H., McNamara, J. P., and Glenn, N. F.: Improvement of distributed snowmelt energy balance modeling with MODIS-based NDSI-derived fractional snow-covered area data, Hydrol. Process., 25(4), 650–660, doi:10.1002/hyp.7857, 2011.

Kyle, H. L., Curran, R. J., Barnes, W. L., and Escoe, D.: A cloud physics radiometer, 3rd Conference on Atmospheric Radiation, American Meteorological Society, 28-30 June 1978, Davis, Calif., p. 107, 1978.

Liston, G. E.: Representing subgrid snow cover heterogeneities in regional and global models, J. Climate, 17(6), 1381–1397, doi:10.1175/1520-0442(2004)017<1381:RSSCHI>2.0.CO;2, 2004.

Maher, A. I., Treitz, P. M., and Ferguson, M. A. D.: Can Landsat data detect variations in snow cover within habitats of arctic ungulates?, Wildlife Biol., 18(1), 75–87, doi:10.2981/11-055, 2012.

Mankin, J. S., and Diffenbaugh, N. S.: Influence of temperature and precipitation variability on near-term snow trends, Clim. Dynam., 45(3-4), 1099–1116, doi:10.1007/s00382-014-2357-4, 2015.

Maussion, F., Scherer, D., Finkelnburg, R., Richters, J., Yang, W., and Yao, T.: WRF simulation of a precipitation event over the Tibetan Plateau, China - an assessment using remote sensing and ground observations, Hydrol. Earth Syst. Sc., 15(6), 1795–1817, doi:10.5194/hess-15-1795-2011, 2011.

Mayr, E., Hagg, W., Mayer, C., and Braun, L.: Calibrating a spatially distributed conceptual hydrological model using runoff, annual mass balance and winter mass balance, J. Hydrol., 478, 40–49, doi:10.1016/j.jhydrol.2012.11.035, 2013.

Pomeroy, J., Bernhardt, M., and Marks, D.: Research network to track alpine water, Nature, 521(7550), 32-32, doi:10.1038/521032c, 2015.

Racoviteanu, A. E., Paul, F., Raup, B., Khalsa, S. J. S., and Armstrong, R.: Challenges and recommendations in mapping of glacier parameters from space: results of the 2008 Global Land Ice Measurements from Space (GLIMS) workshop, Boulder, Colorado, USA, Ann. Glaciol., 50(53), 53–69, doi:10.3189/172756410790595804, 2009.

Rangwala, I., Miller, J. R., Russell, G. L., and Xu, M.: Using a global climate model to evaluate the influences of water vapor, snow cover and atmospheric aerosol on warming in the Tibetan Plateau during the twenty-first century, Clim. Dynam., 34(6), 859–872, doi:10.1007/s00382-009-0564-1, 2010.

Rouse, J. Jr, Haas, R. H., Schell, J. A., and Deering, D. W.: Monitoring vegetation systems in the Great Plains with ERTS. 3rd Earth Resources Technology Satellite-1 Symposium - Volume I: Technical Presentations. NASA SP-351, 309–317, 1974.

Sankey, T., Donald, J., Mcvay, J., Ashley, M., O'Donnell, F., Lopez, S. M., and Springer, A.: Multi-scale analysis of snow dynamics at the southern margin of the North American continental snow distribution, Remote Sens. Environ., 169, 307–319, doi:10.1016/j.rse.2015.08.028, 2015.

Santini, M., and di Paola, A.: Changes in the world rivers' discharge projected from an updated high resolution dataset of current and future climate zones, J. Hydrol., 531, 768-780, doi:10.1016/j.jhydrol.2015.10.050, 2015.

Silverio, W., and Jaquet, J. M.: Prototype land-cover mapping of the Huascaran Biosphere Reserve (Peru) using a digital elevation model, and the NDSI and NDVI indices, J. Appl. Remote Sens., 3, 033516, doi:10.1117/1.3106599, 2009.

Takata, K., Emori, S., and Watanabe, T.: Development of the minimal advanced treatments of surface interaction and runoff, Global Planet. Change, 38(1-2), 209–222, doi:10.1016/S0921-8181(03)00030-4, 2003.

Tekeli, A. E., Akyurek, Z., Sorman, A. A., Sensoy, A., and Sorman, A. U.: Using MODIS snow cover maps in modeling snowmelt runoff process in the eastern part of Turkey, Remote Sens. Environ., 97(2), 216–230, doi:10.1016/j.rse.2005.03.013, 2005.

Tennant, C. J., Crosby, B. T., and Godsey, S. E.: Elevation-dependent responses of streamflow to climate warming, Hydrol. Process., 29(6), 991–1001, doi:10.1002/hyp.10203, 2015.

Thirel, G., Salamon, P., Burek, P., and Kalas, M.: Assimilation of MODIS Snow Cover Area Data in a Distributed Hydrological Model Using the Particle Filter, Remote Sens., 5(11), 5825–5850, doi:10.3390/rs5115825, 2013.

Tucker, C. J. :Red and photographic infrared linear combinations for monitoring vegetation. Remote Sens. Environ., 8(2), 127–150, doi:10.1016/0034-4257(79)90013-0 , 1979.

Vavrus, S., Philippon-Berthier, G., Kutzbach, J. E., and Ruddiman, W. F.: The role of GCM resolution in simulating glacial inception, Holocene, 21(5), 819–830, doi:10.1177/0959683610394882,2011.

Viviroli, D., Archer, D. R., Buytaert, W., Fowler, H. J., Greenwood, G. B., Hamlet, A. F., Huang, Y., Koboltschnig, G., Litaor, M. I., Lopez-Moreno, J. I., Lorentz, S., Schaedler, B., Schreier, H., Schwaiger, K., Vuille, M., and Woods, R.: Climate change and mountain water resources: overview and recommendations for research, management and policy, Hydrol. Earth Syst. Sc., 15(2), 471–504, doi:10.5194/hess-15-471-2011, 2011.

Warscher, M., Strasser, U., Kraller, G., Marke, T., Franz, H., and Kunstmann, H.: Performance of complex snow cover descriptions in a distributed hydrological model system: A case study for the high

Alpine terrain of the Berchtesgaden Alps, Water Resour. Res., 49(5), 2619–2637, doi:10.1002/wrcr.20219, 2013.

Weber, M., Bernhardt, M., Pomeroy, J. W., Fang, X., Härer, S., and Schulz, K.: Description of current and future snow processes in a small basin in the Bavarian Alps, Environ. Earth Sci., 75(17), 1223, doi:10.1007/s12665-016-6027-1, 2016.

Yin, D., Gao, X., Chen, X., Shao, Y., and Chen, J.: Comparison of automatic thresholding methods for snow-cover mapping using Landsat TM imagery, International Journal of Remote Sensing, 34(19), 6529–6538, doi:10.1080/01431161.2013.803631, 2013.

Zhu, Z., Wang, S., and Woodcock, C. E.: Improvement and expansion of the Fmask algorithm: cloud, cloud shadow, and snow detection for Landsats 4–7, 8, and Sentinel 2 images, Remote Sens. Environ., 159, 269–277, doi:10.1016/j.rse.2014.12.014, 2015.

III. Discussion and Outlook

The aim of this dissertation was to generate local scale information about the spatial snow distribution at the sub-catchment. Webcam data was selected as information source and the software package PRACTISE was developed for calculating semantic snow cover maps out of the numeric information given by the webcam RGB images. The final version of PRACTISE is able to generate

- orthorectified RGB images,
- orthorectified snow cover maps, and
- the most appropriate NDSI threshold value for an optical satellite system and a certain area of interest.

With these capabilities, a resource is provided which is able to dramatically improve nowadays monitoring capabilities in mountainous catchments. The temporal and spatial resolution of the achieved results are configurable. The spatial resolution of the PRACTISE snow cover maps is thereby mainly dependent on the spatial resolution of the available DEM while the resolution of the photographs is normally not a limiting factor. This statement is also true with respect to the temporal resolution of the photographs. Even when using webcams from public networks, an hourly resolution is often the standard. This is by far enough for the evaluation of models or for the monitoring of the spatial extent of a snowpack in a given area. Furthermore, the typically high temporal resolution allows for the detection of a matching satellite-webcam pair if it comes to the calibration of a location-dependent NDSI threshold value. Hence, it can be stated that PRACTISE derived snow cover maps are highly adaptable to the personal needs of the user by adequately selecting the camera location and setup as well as the DEM resolution.

Moreover, it can be assumed that the monitoring potential of webcams will further increase in the near future. Webcam networks like www.foto-webcam.eu already show an increasing number of high qualitative and freely accessible webcams in the Alpine region. Such data is an incredible source for scientific data if it is combined with the PRACTISE software package.

The model code of PRACTISE is available on the GitHub platform where it can be easily distributed and updated, if needed. The software is executable in Octave or Matlab making it accessible to and applicable by a wide range of users.

PRACTISE itself is currently used by different research groups e.g. in Austria (University of Graz and University of Innsbruck) and Switzerland (University of Bern), but also in the UK, USA and Canada. This underlines the interest in the new approaches and software package developed in course of this thesis.

However, the potential applications of PRACTISE are yet not fully exploited. A future aim can be the automatic analysis of all images published by e.g. www.foto-webcam.eu for the generation of a spatially well-distributed NDSI calibration database. This would allow for the generation of an area-dependent NDSI threshold map for the European Alps. The local accuracy of e.g. Landsat-based snow cover maps would be significantly increased by having such a source of information. Another aim would be the derivation of the surface albedo and of different radiation terms on basis of the available information about the target area. For doing so, the exposure time of the webcams and the ISO value of the webcam images, which are partwise published as additional information, could be used in combination with albedo values of the objects in the field of view.

A certain limitation of the current approach is that the terrestrial as well as the satellite-based analysis is limited to the spatial extent of the snow cover but it delivers no information on the snow water equivalent (SWE) nor on the snow cover height and respectively the snow volume. While an approximation of the volume might become possible in the future by using two cameras or two high-resolution optical satellite sensors with a slightly different orientation and by making use of the image displacement, an accurate estimation of the SWE will stay unreachable. In this context, it has to be stated that a successful approach for a stable estimation of the SWE is still lacking in satellite remote sensing (Dozier et al., 2016; Shi et al. 2016). Shi et al. (2016) are also outlining that current microwave-based SWE products might be promising from a theoretical point of view but they still have large uncertainties and therefore are, as yet, not applicable for e.g. the evaluation of hydrological models. Hence, the best method to estimate SWE until now is to optimize model results in a way that they are able to cover the

snow depth measurements at the stations as well as the snow cover extents derived from optical data. If a model fulfils these two requirements, it also tends to reproduce the SWE development well.

Finally, it can be stated that PRACTISE today is a fully functional, widely used observation package, which has proven its capabilities in the course of different studies. PRACTISE is a very flexible and stable software tool which is freely available and which can be seen as an excellent starting point for additional routines developed by interested scientists. The source code as well as the detailed manuals that were published together with the papers can be found in my GitHub repositories. The subsections *Supplement* or *Code Availability* at the end of publication I, II and III outline the details.

References

Dozier, J., Bair, E. H., and Davis, R. E.: Estimating the spatial distribution of snow water equivalent in the world's mountains, WIREs Water, 3, 461–474, doi: 10.1002/wat2.1140, 2016.

Shi, J., Xiong, C., and Jiang, L.: Review of snow water equivalent microwave remote sensing, Sci. China Earth Sci., 59(4), 731–745, doi: 10.1007/s11430-015-5225-0, 2016.